מכון ויצמן למדע
WEIZMANN INSTITUTE OF SCIENCE

Thesis for the degree
Doctor of Philosophy

עבודת גמר (תזה) לתואר
דוקטור לפילוסופיה

Submitted to the Scientific Council of the
Weizmann Institute of Science
Rehovot, Israel

מוגשת למועצה המדעית של
מכון ויצמן למדע
רחובות, ישראל

By
**Luca Moleri**

# Development of large-area gas-avalanche Resistive-Plate WELL detectors: potential sampling elements for digital hadron calorimetry

Advisors
**Amos Breskin, Shikma Bressler**

המנחים:
**עמוס ברסקין, שקמה ברסלר**

December 2017

טבת תשע״ח

# Acknowledgements

Out of the all thesis work, this is really the most difficult part to write. It is impossible to put in few words all the thanks that I want to express to so many people, for so many things, big and small that I received from them. So, the few words that follow are only a drop of what is in my thought and I would like to express but I am not able to. In any case, all the people that I met during these six years, that I will not name explicitly, can be sure of my deepest gratitude and affection.

אני מודה לעמוס ושקמה שסמכו בי ונתנו לי את ההסדמנות לעבוד איתם לכמה שנים טובים. אני מאוד גא להיות סטודנט של עמוס והסטודנט הראשון של שקמה. תודה שאישרתם לי לנסות, לטעות, לשבור, לבנות וסך הכל ללמוד. במיוחד תודה שנשאתם את האופי שלי הקשה. גם בצד הזה בזכותכם גדלתי הרבה.

Thanks to all my colleagues that in these six years supported me and collaborated with me. It is needless to say that alone I could not do any of the work that is presented in this thesis. More than that, your company has been fundamental to make the time spent in the lab interesting and gave me relief in the dry and upsetting moments.

המון תודה לכל צוות המזכירות והשירותים הפיזיקלים. בלי עזרתכם העבודה שלנו היא פשות בלתי אפשרי.

Grazie alla mia famiglia, quella carnale. Grazie mamma e papà che avete sempre sostenuto la mia avventura, anche quando vi costa fatica e non capite. Spero che anche se siamo spesso lontani possiate godere anche voi dei bei frutti che il Signore non smette di regalarmi.

Thanks to my brothers in the faith that have been my close family here in Rehovot. You have been the unexpected and surprising answer to my prayer.

Grazie alla mia famiglia di chiamata, agli amici di Comunione e liberazione che in questi anni sono stati in Israele, o che mi hanno accolto ovunque andassi, e ai vecchi amici ora sparsi per il mondo. Senza di voi semplicemente non sarei quello che sono. Ancora più specialmente grazie ai miei fratelli Memores Domini, per il vostro "si" e il segno di conforto e di speranza che siete per me. Soprattutto Giovanni che è stato la mia "casa" e guida fin dall'inizio.

# Declaration

I here declare that the presented work summarizes my independent research.

The entire work was conducted in collaboration with colleagues from Weizmann Institute of Science (WIS) and other institutes. In particular:

- I was involved in all the detector prototypes development and assembly, except for the $30 \times 30$ mm$^2$ detector that was designed and assembled by Dr. Artur Coimbra and Dr. Purba Bhattacharya. The $100 \times 100$ mm$^2$ tiled prototypes and the $500 \times 500$ mm$^2$ prototype were designed and assembled by myself and Dr. Artur Coimbra. Dr. Purba Bhattacharya participated in the assembly of the $500 \times 500$ mm$^2$ detector.

- The test-beam campaigns conducted in winter 2014 [1] and summer 2015 [2, 3] involved researchers from different institutes, as indicated by the author lists of the relevant published papers. Other two test-beam campaigns were carried out by myself together with Dr. Artur Coimbra in summer 2016 [4], and with Dan Shaked-Renous and Dr. Purba Bhattacharya in summer 2017. In all cases, I tested the prototypes in the lab, set-up the system in the beam area and performed the measurements. I also analyzed the data, produced the published plots and wrote the published papers.

- The edge-effect study described in appendix C was conducted mainly by Dr. Artur Coimbra and Dr. Purba Bhattacharya. I contributed with ideas, the installation of the x-y scanner and with software analysis.

- The large area x-y scanner described in section 2.2.1 was operated with the help of Dr. Ilia Ravinovich.

- Monte Carlo simulations for position resolution studies described in section 2.4.1 were done by myself and Dr. Purba Bhattacharya. Dr. Purba Bhattacharya contributed with the data from Garfield simulations (including neBem, Heed, and MagBolts software packages).

# Contents

# Abstract

The construction of new accelerators goes along with the development of advanced detectors and instrumentations. Since many scenarios of new physics Beyond the Standard Model (BSM) of particles involve hadronic-decay channels, efforts are made to develop modern calorimetry systems. All experiments designed for future linear colliders foresee the implementation of a (semi-)Digital Hadron Calorimeter ((s)DHCAL) as a key-element for their expected performance.

The present work targeted the development of a large-area, robust, thick detector concept, suitable as sampling element in a sDHCAL and for other applications requiring particle imaging at moderate, sub-mm spatial resolution over a large area. As a solution, the few-mm thin Resistive-Plate Well (RPWELL) sampling element concept, developed at WIS, was suggested: a single-sided Thick Gas Electron Multiplier (THGEM) electrode coupled to the readout anode through a highly Resistive Plate (RP).

Several detector prototypes, reaching a size of $500 \times 500$ mm$^2$, were built. They incorporated either Semitron ESD225 acetal, or silicate doped-glass Resistive Plate (RP). Methods were developed for effectively coupling the RP to the readout anode.

The detector prototypes underwent various systematic investigations - both in the laboratory, and with muon and high-rate pion beams at the European Organization for Nuclear Research (CERN)-Super Proton-Synchrotron (SPS).

The presented results allow for a deeper understanding of the RPWELL detector concept and properties. Moreover, they are essential for optimizing the design of future large-area prototypes and their performances for different applications.

Their main properties are: stable operation with Ne/(5%)$CH_4$, Ar/(5%)$CH_4$ and Ar/(7%)$CO_2$ gas mixtures. High efficiency (>98%) at low average pad multiplicity ($\sim$1.2). Position resolution of 0.28 mm. These properties make the RPWELL a competitive technology, compared to other candidate sampling elements for sDHCAL or Digital Hadron Calorimeter (DHCAL).

Based on this study, the preferable RPWELL detector configuration for future (s)DHCAL would include a 3 mm drift gap, single-sided THGEM electrodes with segmented holes pattern (segmentation similar to that of the readout anode), Semitron ESD225 or doped silicate-glass resistive-plate coupled to the anode through graphite/epoxy. The preferred operation gas mixture is the non-flammable Ar/(7%)$CO_2$.

Future RPWELL-based (s)DHCAL prototypes will be read out by the (s)DHCAL-dedicated MICROROC readout electronics [5] - the next step towards the integration of RPWELL sampling elements into a full (s)DHCAL prototype.

# Chapter 1

# Introduction

Elementary particles and their interactions are described by the Standard Model (SM) of particle physics. In the last 50 years, thousands of experiments have been performed in the field of particle physics, and none have shown and confirmed deviations from the predictions of the SM. However, the SM fails to explain fundamental phenomena such as gravity, neutrino masses, dark matter and more. These shortcomings indicate that the SM must be extended.

A precise measurement of the properties of the Higgs boson, its mass, decay products, branching ratios, and coupling to other SM particles, is a key ingredient in the foreseen high energy physics program. Any deviation from the SM-predicted values could indicate upon the nature of new physics BSM. The current experimental data from the Large Hadron Collider (LHC) permits a branching ratio for Higgs decay to BSM particles as high as 20% [6]. Indeed, some BSM theories predict a branching ratio of Higgs decay to new singlet scalars or new fermions as high as 10% (depending on their masses). An improved precision yielding sensitivity to new scenarios is foreseen with the High-Luminosity LHC (HL-LHC) data [7]. Nonetheless, it is already clear that even with the foreseen upgraded detectors, the precision that can be obtained for some important scenarios using the HL-LHC data is insufficient. For example, in some scenarios, a branching ratio of the of Higgs decays to new light scalars below the 5-10% level can not be excluded [6, 8]. In addition, the QCD background in hadron colliders inherently reduces the sensitivity for measuring coupling of the Higgs to certain quarks, e.g. the charmed quark, and to gluons [9].

These considerations motivate the development of future electron-positron colliders such as the International Linear Collider (ILC) [10], the Compact Linear Collider (CLiC) [11], the Circular Electron Positron Collider (CEPC) [12], and the Electron-Positron Future Circular Collider (FCC) [13]. Those could cover larger areas in the parameter space of BSM physics as well as allow reaching, in some of the key channels, precisions higher than that foreseen at the HL-LHC.

The construction of new accelerators goes along with the development of advanced detectors and instrumentation, without which the potential of these facilities cannot be fully exploited. Since many BSM scenarios involve hadronic-decay channels, efforts are made to develop modern calorimetry systems. The current target performance is driven by the desire to enable good mass separation between the weak bosons (W and Z) in their hadronic decay mode; this will allow, for instance, measuring the branching ratios of the Higgs boson's decay to Z and W to precisions better than 1.9% and 0.44% (RMS) respectively [9]. Such precision requires jet-energy resolution of at least $30\%/\sqrt{E}$ which corresponds to σ/E=3% for 100 GeV jets (see for example [10]), close to the resolution of the ZEUS calorimetry system [14] and three times better than the one measured with the A Toroidal LHC Apparatus (ATLAS) and Compact Muon Solenoid (CMS) calorimeters [15, 16].

The present work aims at the development of the Resistive-Plate Well (RPWELL) detector [17], as a potential sampling element for hadronic calorimetry in future particle-physics experiments. After a brief historical perspective on radiation detectors (section 1.1), Micro-Pattern Gaseous Detectors (MPGDs) will be presented in section 1.2. A deeper look into the role of resistive materials in gaseous detector is the topic of section 1.3. In Section 1.4, after an introduction to THGEM detectors, the main subject of the present work: the RPWELL concept [17] will be presented.

While it could become a detector of choice for moderate-resolution radiation tracking, we will put an accent on its potential application in (s)DHCAL in future linear colliders: ILC [10], CLiC [11], CEPC [13, 18], and in the FCC [12]. Potential target experiments would be the Silicon Detector (SiD) [19], or the International Linear Detector (ILD) [20] designed for ILC. The semi-Digital Hadron Calorimeter (sDHCAL) concept and the requirement imposed on its sampling elements are discussed in section 1.5.

## 1.1 Brief history of radiation detectors

> "Just as modern biology was launched with the invention of the microscope, in physics, too, areas for investigation have been opened with the development of new observational tools."[1]

Towards the end of the XIX century, almost at the same time two major discoveries happened: different kinds of natural radiation originating from several materials, and an unavoidable background of penetrating ionizing radiation coming from the upper atmosphere. A new unexpected window to nature opened up: that of nuclear and cosmic ray physics. The question about the source and the nature of these unknown kinds of radiation motivated many physicists to investigate them both experimentally and theoretically. Experimentally, the challenge was clearly making these elusive objects visible and measurable. Thus, the development of adequate imaging instruments became of capital importance. Since 1911, the fortunate invention of an

[1] V. L. Fitch, Elementary Particle Physics: The Origins [21]

imaging instrument, the **cloud chamber** [22], allowed photographing the tracks of cosmic particles.

The cloud chamber was developed to study the effects of light in the clouds, but it soon became the principal instrument to look at nuclear interactions and cosmic rays. In one of the first observations, the track left from an electron-like particle having opposite charge was captured. It was recognized by Anderson as the positron [23], predicted theoretically a couple of years earlier by Dirac, as a result of its relativization of the Shrödinger equation. Occhialini and Blackett confirmed the nature of the new particle [24] by observing the production of electron-positron pairs in showers originating from cosmic rays (a new phenomenon called electro-magnetic showers). Using a $\gamma$ source, they also demonstrated experimentally for the first time the transformation of radiation into matter. In their experiments, the cloud chamber expansion was triggered by the passage of a cosmic ray, using **Geiger-Müller tubes** [25] and a coincidence circuit. It was remarkably the first time that a triggering system has been used; a concept which implementation became a crucial aspect of modern high-energy physics experiments. Other than for triggering, **counting devices** [26] like Geiger-Müller tubes and **scintillators** with **photo-multipliers** were also used for timing measurements. This was necessary, for example, for the measurements of particles lifetime, especially important to understand the nature of the interactions underlying the decay.

From the theoretical point of view, an idea was diffused that the particles constituting the cosmic rays could be related to the components of atomic nuclei and their interactions, which are the source of radioactivity. Yukawa theorized that nuclear interactions might be mediated by a particle yet to be discovered [27]. Some events confirming this theory had been already observed a few years earlier, in 1947 by Perkins, Occhialini and Powell using **photographic emulsions** (for a deep overview see Powell's Nobel prize speech in 1950 [28]). In this technique photographic plates are impressed by the passage of charged particles and the tracks left are then analyzed under microscope. The thickness of the track indicates the amount of deposited energy Together with its range, it gives an estimation of the mass.

The possibility to bring these very compact detectors to high altitudes (by balloon, airplane or at the top of mountains) allowed measuring the primary constituents of the cosmic radiation - mainly H and He with small fraction of light atomic nuclei - and their nuclear decays when interacting with the atmosphere. A two-body decay of a primary particle, which was called $\pi$-meson[2] or pion, to a secondary one $\mu$-meson or muon, and one neutral particle (recognized as the neutrino emerging from a $\beta$ decay) was recorded. A photographic emulsion is very suitable to measure such reactions, because its density is large enough to stop mesons and look at their decay at rest. Subsequent mass measurements from twenty events resulted in the pion and muon masses; the pions were the particles postulated by Yukawa. This led to the conclusion that most of the mesons observed at sea level are penetrating muons arising from the in-flight decay of pions created in nuclear disintegrations, higher up in the atmosphere.

Many more particles were discovered in the same way, including the $\tau$ lepton and strange mesons (decaying with lifetimes incompatible with their strong interaction): neutral V particles (today $\Lambda$ and K) and others. The study of cosmic rays with cloud chambers and emulsions remained the only source of information about the new particles through most of the 1950s.

The last significant experiments using a cloud chamber were the observation of associated production of strange particles in Brookhaven (in this case with a **diffusion chamber** [29]), and the search for the predicted long-lived K meson. Then accelerator experiments took over, yielding high-rate production of particles with increasing masses. A new device, the **bubble chamber**, inspired by a glass of beer in

[2]currently called $\mu$ lepton

a pub, was ideally suited for use with accelerators and soon took over as the visual detector of choice. As Glaser, the bubble chamber inventor, described in his Nobel lecture [30], the requirements posed by accelerator experiments were demanding and called for new technologies: there was a need for a particle detector of high density and large volume - tens to hundreds of liters - in which tracks could be photographed and scanned, and in which precision measurements of track geometry could be made. When large proton synchrotons in the few GeV energy range came into operation in the early 1950s, expansion cloud chambers were not suitable anymore; the synchrotrons had pulse repetition frequency of a few seconds, while the expansion cloud chambers (which operated with internal gas pressures up to 300 atmospheres) required waiting times of 15 to 30 minutes between expansion cycles.

The bubble chamber concept is based on the thermodynamic instability of a superheated liquid, that can be used to detect minimum ionizing radiation if the density of ionization energy deposited in the liquid along the path of the particle is sufficient to form a vapor bubble nucleus large enough to grow to photographable size.

Bubble chambers became widespread over many facilities having new acceleration complexes. Being complex, bubble chambers required the collaboration of many specialized technicians and large teams of people to scan and analyze the figures. Already at that time, scientists dreamed of computers capable of recognizing specific particle-track patterns and analyzing the experimental results. An important result obtained at the European Organization for Nuclear Research (CERN), with the Gargamelle bubble chamber in a neutrino beam was the proof of the existence of sub-nuclear constituents (quarks) and the observation of neutral current interactions, in support of the theory for the unification of the electromagnetic and weak forces.

Due to the need for higher acquisition rates than what a bubble chamber could provide, and the need to trigger detectors on specific pre-selected events, new technologies were developed. The first were different categories of photographic but triggerable

**spark chambers** and **streamer chambers** [31]; they were vastly used in numerous particle-physics and cosmic-ray experiments (see for example [32] and [33]). Next came electronically-recorded spark chambers, with increased operation rates. For an historical perspective on the transition to electronic radiation imaging detectors, the Nobel lecture of Georges Charpak is a noticeable synthesis [34].

A Spark chamber consists of a stack of conductive plates or wire planes in a gas medium; when an ionizing particle passes through it, a high voltage pulse is applied between the plates (upon the appearance of a trigger signal) - resulting in a track of local discharges. The track image can be recorded by photography, or recording the current pulses induced on the wires. Standard spark chambers were simple to operate, yielding over 100-fold higher operation rates - but did not provide the localization resolutions of a bubble chamber, compromising, for example, on the details of some interaction vertexes. For this reason, spark chambers were introduced in most cases as a supplement to bubble chambers. An important result obtained with a spark chamber system was, for example, the measurement of muon neutrinos [35]. The more complex streamer chambers, requiring very fast and very high voltage pulses yielded, by photographic means, resolutions close to that of bubble-chambers.

Other than acquisition rates, one of the major advantages of electronic devices was the new possibility to record signals automatically through a computer (developed in the same period); this also opened the possibility to automatically analyze large sets of data.

A detector that literally revolutionized the field of particle physics is the **Multi-Wire Proportional Chamber (MWPC)** developed by Georges Charpak (Nobel prize in 1992) in the late sixties. These detectors, often called "wire chambers" [36], consist of a central plane of thin anode wires kept at high positive voltage, interposed in-between two segmented cathode planes (with wires or strips at different angles). Their operation, in a gas-avalanche mode, is similar to that of Geiger-Müller tubes.

Charged particles (but also x-rays or neutrons) ionize the gas, releasing electron-ion pairs; electrons drift (driven by the electric field) towards the anode wires, where charge-multiplication occurs in an avalanche mode under the very intense electric field. The resulting electronic signal is proportional to the primary charge deposited. Avalanche electrons are promptly (within ~ns) collected by the anode wires, while avalanche ions slowly drift away - inducing charge signals on the anode wires and on the segmented cathode planes. The resulting anode and cathode signals are amplified by electronic circuits; data are collected and digitized by advanced computer-driven acquisition systems.

Wire chambers permit reaching data-acquisition rates approaching a MHz/cm$^2$. A good example of large MWPC detectors are that of CERN-UA1 experiment - the first multi-purpose experiments at CERN - which permitted the direct observation of the W and Z bosons (Carlo Rubbia, Nobel prize in Physics), mediators of the weak interactions [37]. In this detector, the internal region around the beam was a large drift chamber for precise track reconstruction, and the external part after the calorimeter was tiled with small-gap wire chambers for muons localization.

A more advanced wire-chamber configuration is the **drift chamber** [38], in which anode and cathode wires are alternated, and the localization is done by measuring also the drift time (to the anode wires) of the primary charge. These detectors permit recording the track in 2D, with superior position resolutions with respect to a normal MWPC.

A similar combination of time and position measurements is implemented in large volume **Time Projection Chambers (TPCs)** [39]. Measuring the primary electrons drift time over a long distance until reaching a MWPC plane where they are collected and multiplied, the 3D track can be reconstructed with a performance comparable to that of cloud or bubble chambers. Installed in numerous particle-physics experiments, TPCs record precisely and simultaneously multiple events originating from particle interactions The acquisition rate is limited by the drift time of electrons and ions in the large gas volume.

The most modern TPCs in use are the CERN-LHC ALICE TPC [40] and that of BNL-RHIC STAR experiments [41], recording with great precision, with large wire-arrays, hundreds of particles per relativistic-ion collision. The development of low-noise, very large scale integrated readout electronics, made it possible to design enormous detection systems acquiring information from tens of thousands of channels simultaneously and yielding resolutions below 100 μm.

Some wire-chamber systems yield resolution times of a few tens of ns at rates close to a MHz, making it possible to study rare phenomena which were beyond the reach of optical detectors. MWPCs are still widely used in current high-energy experiments; an example of one of the world-largest wire-chamber system is the ATLAS muon system, using thousands of Thin-Gap Chambers (TGCs) [42], developed and built at WIS [43].

Modern high-granularity "electronic detectors" equipped with fast readout channels, certainly marked the end of the bubble chamber era.

While the present work deals with novel gas-avalanche chambers, it is worth mentioning that in parallel to the progress in gaseous detector techniques there has been enormous progress in modern semi-conductor detectors. Even though they are much more costly than gaseous detectors, they are widely used as high precision (few μm), fast (<ns) tracking devices in most particle-physics experiments, constituting the core of the vertex reconstruction systems (as a latest development see for example [44]). In addition, solid-state detectors, e.g. silicon photo-multipliers [45] are replacing in many cases traditional photo-multiplier tubes and can be used also in calorimetric systems.[3]

[3] Bubble chambers and emulsions are still used in current low rate experiments and give unbeatable performance in terms of track reconstruction and energy deposition precision.

In the last decades, the industrial development of Printed Circuit-Board (PCB) technology opened up many possibilities for obtaining high electric-field configurations in a gas. A new entire family of detectors has been developed: that of **Micro-Pattern Gaseous Detectors (MPGDs)** [46].

## 1.2 Micro-pattern gaseous detectors

MPGDs, produced by the modern photo-lithographic technology on glass and on flexible and standard PCB supports are replacing the old generation MWPCs [36]. They play a pivotal role in large particle physics and nuclear physics experiments and in applications such as x-ray [47, 48], UV [49] and visible-photon [50] and neutron [51] imaging reading the signal with electronics systems, or with optical recording from the light emitted by fluorescence of the gases in the multiplication process. For a complete review on MPGDs see the book [52].

Like in MWPCs, in MPGDs the detection is based on charge-avalanche multiplication in high electric-fields in a gas. Thus, a fundamental understanding of electron and ions interactions with different gas molecules under various condition (pressure, field, etc.) becomes crucial. For this reason, together with the experimental efforts, different sets of simulation tools were developed, for example Garfield [53] and MagBoltz [54]. The development of MPGDs progressed in parallel with that of readout electronics, with two main outcomes: 1) the integration of an increasing number of readout channels in a single chip board allowed for very fine readout segmentation and therefore higher rate capabilities 2) improving the sensitivity and lowering the electronic noise allows for efficient operation at gas gains as low as $\sim$100-10000, depending on the specific application.

Examples of MPGD technologies are Micro Strip Gas Chambers (MSGCs) [55] with thin strips patterned on an insulator (glass); Gas Electron Multipliers (GEMs) [56], with arrays of tiny holes etched in a thin double-sided copper-clad Kapton sheet; Micro-mesh gaseous structure (MICROMEGAS) [57], where the multiplication occurs between a micro-mesh and the readout anode; and the more recent Thick Gas Electron Multiplier (THGEM) [49] and THGEM-based COBRA [58] and WELL concepts [59], with the avalanche occurring in sub-mm diameter hole-arrays drilled in a PCB. Other examples are the MHSP [60], multi-layer THGEM [61], Micro-Pixel Chambers [62], capillary gas detectors [63], InGrid detectors [64] and many others. Detectors based on these technologies and concepts have been used for numerous experiments and are being designed for future ones [65, 66, 67, 68, 69, 70]. An active R&D activity is ongoing with the emergence of new detector structures to improve their performances in terms of spatial resolution (tens of microns to sub-millimeter scales - according to experimental needs), fast response (ns scale, recently reaching ps in specific configurations [71]), pulse-height resolution, photo-detection, and high counting rate capability (reaching MHz/mm$^2$).

With their versatility and properties, MPGDs are applicable in numerous fields, including in noble-liquid based detectors [72, 73, 74, 75, 76, 77]. MPGDs permit operation also at very low gas pressures [78, 79]. For recent reviews on the history of MPGDs and their latest developments and applications see for example [46, 80] and references therein. In recent years some effort has been put into the development of new materials both as substrates (see for example [81]) and as readout electrodes (see for example [82]). The second case, the use of resistive electrodes, is one of the most recent trends in MPGD research; it aims at limiting intense occasional electrical discharges, often due to highly ionizing events. The latter can damage both detector and electronics and induce dead-time. We will discuss in more detail in section 1.3 the role of resistive materials in gaseous detectors.

## 1.3 Electrical stability of gas-avalanche detectors and the use of resistive materials

### 1.3.1 Electrical breakdown in gaseous detectors

Electrical breakdown is an issue common to all gaseous detectors and in particular to MPGDs, that typically do not have discharge self-quenching mechanisms (as MWPCs do [83]). A spark or discharge between electrodes in a gaseous environment is the development of a conductive and self-sustained plasma that connects them, causing a large amount of charge to flow.

Experimentally, discharges in gaseous detectors are associated with highly ionizing events (with higher probability to occur under high irradiation rate) or other processes such as photon feedback, spontaneous electron emission or avalanche gain fluctuations. These mechanisms point to the same generally accepted picture: when the total charge density in an avalanche becomes higher than $10^7$ -$10^8$ electron-ion pairs - known as the Raether limit [84] - the avalanche may evolve into a discharge.

Considering the detection of Minimum-Ionizing Particles (MIPs) (e.g. relativistic muons). The most probable number of Primary Electrons (PEs) left by a MIP in a few mm gas is around 10-15. For this signal to be detected, gas amplification of the order of $10^4$ is needed. Therefore, ionization processes inducing more than $10^3$ primary electrons over distances comparable to the typical lateral extent of an avalanche (a few 100 $\mu$m) carry the risk of leading to discharges by avalanches surpassing the Raether limit. Such ionization levels are possible but less common for MIPs (due to their typical energy deposition). They easily reached by interactions in the detector gas or detector materials resulting in heavily ionizing particles from natural radioactivity and experimental radiation background (e.g. neutrons).

It is commonly accepted that sparks are initiated by the formation of a streamer [85]:

a filament of plasma developing in the presence of high electric fields when the space-charge distribution in the head and tail of the avalanche is large enough. The streamer is developing in space until it connects the anode and cathode electrodes and a spark occurs [86, 87]. Normally the discharge is terminated when the spark current leads to a sufficient reduction in the voltage, and therefore in the electric field and so to a local gain reduction. This self-terminating discharge mechanism is observed in THGEM detectors, while for example GEMs need an external intervention to end the discharge and avoid a current trip.

Even though the general picture is clear, it is not trivial to get a detailed description of the dynamic process leading to a discharge; it depends on the specific gas mixture, density, and detector geometry and operation. It is a complex physical process involving electron transport in variable fields, electron multiplication in high fields, space-charge distorted electric field, emission of photons able to photo-ionize the gas at a certain distance. Several attempts have been made to study this phenomenon, trying to compare experimental data with both analytical and computational results.

UV photons are emitted by atomic de-excitations in an avalanche process. In a gas mixture, those photons could be energetic enough to extract photo-electrons outside the avalanche from the gas molecules. Those electrons could contribute to maintain the streamer expansion at its tail. This is not the case in pure noble gases where the excitation photons do not have enough energy to ionize gas molecules. In parallel-plate geometries there is also the possibility that UV photons extract electrons from the electrodes, those electrons can start secondary avalanches that can sustain the streamer formation. In MPGDs with avalanches occurring in holes, namely in "closed geometries", this effect is reduced. On top of these processes, it has been shown in [88] that diffusion alone could provide a sufficient mechanism for positive streamer front propagation in some simplified (but quite reasonable) conditions.

In recent studies, conducted with COMSOL Multiphysics simulation software[4], the charge multiplication process was simulated using hydrodynamic equations for a gas of electrons and ions, and parametrized curves as inputs for the physical processes governing the transport and production of charges. The studies show (even pictorially) that indeed the streamer propagation to the cathode can be sustained by ion diffusion in high field only, without the aid of photons [89][5]. A recent attempt to relate the simulated charge density to discharge probability measurements in a quantitative way is presented in [90]. The simulation was done using GEANT4 software [91]. The critical charge density leading to the formation of a spark in a GEM hole is found to be within the range of (5-9)$\cdot 10^6$ electrons after amplification (close to the Raether limit), and it depends on the gas mixture.

### 1.3.2 The use of resistive materials in gaseous detectors

As explained in [92], most MPGD detectors lack an avalanche saturation mechanism like the one available for example in MWPCs [48], and they are therefore limited in their dynamic range by the occurrence of discharges.

Resistive materials have been used as electrodes (especially anodes) in gaseous detectors for a few decades. They were introduced in an attempt to prevent discharges and/or quench their energy, thus, stabilizing the detector performance, minimizing the discharge-associated dead time and protecting the readout electronics.

The concept relies on the fact that anodes or cathodes with high resistivity block the instant drain of charge deposited by the electric breakdown through the following mechanism: the charge accumulating locally in the resistive material for a relatively long of time produces a local drop in the electric field. This causes self-quenching

[4]https://www.comsol.com

[5]The details of this simulation were presented in December 2017 during RD51 open lectures at CERN, based on a previous work by Paulo Fonte.

of the discharge, or even stops the streamer development at an early stage. In the first case, the amount of charge involved in the discharge (which for fully conductive anodes is limited only by the total charge stored in the assembly of the participating electrodes) is then reduced; in the second case, the discharge doesn't occur, and the end result is just a large avalanche.

A successful application of resistive materials to gaseous detectors is the **Resistive-Plate Chamber (RPC)** detector [93]. Based on original works from Pestov [94], the Resistive-Plate Chamber (RPC) consists in a parallel-plate chamber whose plates are made of a thick (∼mm) resistive material of typical bulk resistivity of $10^7$ -$10^{12}$ Ωcm. In the RPC operated in spark mode, when the gas is ionized by a charged particle, a discharge is originated by the electric field (similarly to a spark chamber). However, due to the high resistivity of the electrodes, the electric field is strongly reduced in a limited area around the point where the discharge occurred, so that the latter is prevented from discharging the entire charge stored in the plates; out of this area the sensitivity of the counter remains unaffected [95]. For a review on RPC detectors see [96].

An undesired effect of using electrodes with large resistivity is the gain drop and hence efficiency loss observed under high irradiation rates. In fact there is a trade-off between the high resistance needed for effective discharge quenching and the low resistance required for operating efficiently at high particle fluxes. For this reason, the resistive plate should be optimized for the usage in specific applications. In order to choose the best resistive material and its geometry, it would be important to know its recovery time constant, and its quenching power - i.e. the entity of the local reduction of the electric field due to the charge deposited during a discharge.

A model describing these effects was proposed for example in [97] and reviewed in [98] (a similar one was recently used in GEM coupled to a resistive layer [99]). Depending on the resistivity of the material and the geometry of the detector, the charge produced in the avalanche process is evacuated through the resistive material within a finite time, $\tau$, corresponding to an equivalent RC circuit. If this time is long enough, the charge accumulating causes a local potential drop which prevents the discharge from evolving. An attempt to model this phenomenon in RPCs was introduced in [100]; a column with cross-section O and a height equal to the layer thickness D has a resistance of R= $\rho$D/O, where $\rho$ is the bulk resistivity of the material. The virtual capacitance of this column equals to C= $\epsilon_0\epsilon_t$O/D, where $\epsilon_t$ is the permittivity of the material. The product of the column resistance and capacitance is a time constant $\tau= \epsilon_0\epsilon_r\rho$ , which does not depend on the layer thickness and can be associated with the recovery time of a potential charge on the layer surface.

This simple model is not supported by the results shown in [101] where the gain drop in RPC detectors at increasing particle fluxes depends on the plate thickness. The authors argue that the resistive plate does not behave as a simple RC circuit. Therefore, in addition to the bulk resistivity and the dielectric constant, also the surface and the thickness of the plate are important and change the RC response of the plate. Since in RPCs there is current flowing both on the surface of the plate and through the bulk of the plate, there must be a lower limit in resistivity and thickness, below which sufficient current can flow through the plate to sustain the discharge.

Another attempt to identify the parameters involved in discharge quenching can be found in [102]. The authors point out that resistive materials lie in between two limit cases depending on the typical effective response time RC of the resistive electrode, being R the resistance and the C the capacitance effectively involved in the streamer formation process. The case RC= $\infty$ is when the electrode is a perfect insulator. In this case, charge accumulates until there is no electric field; the case RC= 0 is when the electrode is a perfect conductor, so the field is maintained until discharge fully develops. In order to quench the discharge, the resistive material RC time should be longer compared to the development time of the streamer. Even if this simple model is correct, any estimation of the values of the effective R and C is highly non-trivial; on top of that, the streamer development itself is not fully understood (see section 1.3.1). In the same presentation, the author shows a test done with six MICROMEGAS prototypes with the same resistive layer thickness but different total resistance, placed in a high-intensity hadron beam behind an absorber (1 MHz 150 GeV pion beam showering inside a 2 interaction-lengths steel block). It was shown that below a certain value of the resistance, the mesh current during an accelerator spill fluctuates, just like a non-resistive prototype subject to sparking. Above a critical value of the resistance, the current is somewhat constant as if due only to the normal ionization and multiplication process. This critical resistance value suggests that there is a threshold RC above which spark suppression becomes effective. The author gives also an estimation of the capacitance involved in the process and compares the resulting RC with the avalanche development time, (e.g. $\sim$10 ns in the specific case of resistive MICROMEGAS).

Other than introducing a spark quenching mechanism and rate limitations, another effect of resistive materials on the detector operation is its influence on signal development, both in time, amplitude and space. As an example in [103] the effect of resistive anode strips on the signal shape is described. A theoretical and systematic approach to this issue is given in [104]. Resistive layers play an important role also in the detector's spatial resolution. In the TGC [42], for example, graphite-coated insulating foils were used as cathodes to decouple the readout from the gas volume. In that specific case the very thin resistive layer was grounded at its sides to cause the avalanche charge spreading in the layer before evacuating. This configuration was coupled to a segmented readout electrode to induce signal on several channels allowing for improved spatial resolution [43]. The same idea was later applied to MPGDs, for example to GEM [105] and THGEM [106].

The use of resistive materials in MPGDs to quench discharges has been implemented mainly in the form of thin resistive films, where the resistance is developed on the surface of an insulating sheet (for example in MICROMEGAS [107], GEM [99], and THGEM (section 1.4)). Methods of "embedded resistors" were investigated as well [108]. A special case is the one of the RETGEM [109], in which the multiplier electrode itself is resistive, rather than the anode.

In [110] it was suggested that using the resistance through the bulk of a thick material, like the resistive plates in RPCs, may be applied to MPGDs, with the advantage of obtaining higher-rate detectors. Indeed, this idea has been successfully employed in the **Resistive-Plate Well (RPWELL)** detector [17], which is described in detail in section 1.4. One of the advantages of this concept of coupling a RP to the anode rather than a resistive layer is the smaller avalanche-charge spread across the surface; this should, for example, result in a lower pad multiplicity in "digital" detectors. Another advantage demonstrated in this work is that a resistive plate can quench discharges more effectively than a thin resistive film, as discussed in section 1.4 when comparing Resistive Well (RWELL) and RPWELL detector results.

## 1.4 The THGEM and Resistive Plate WELL detectors

### 1.4.1 The THGEM detector

The THGEM [49, 111] was developed and intensively investigated by the WIS radiation detection physics team and collaborators. R&D research was conducted at room temperature [112, 106, 113, 114, 115, 116, 117, 118, 58, 119, 120, 121, 122, 123, 124, 125, 126, 17, 127, 59, 128, 92, 129, 130, 1, 3, 2] and in cryogenic environment [131, 132, 75, 133, 76, 134]. Advances in the development of this multiplier have been also achieved by the Trieste team [65, 135, 136] and recently by others [137, 138, 139, 140]. Being simple, robust, economically produced, and rather fast (ns scale), the THGEM has been attracting significant attention, due to its potential applications to large-area particle tracking at moderate localization resolutions. With its sub-millimeter spatial resolution [106, 4], ns-scale time resolution [115] and high counting-rate capability [112], this MPGD is suitable to cope with the needs of large particle-physics and astro-particle physics experiments as well as inspection applications over very large detection areas. CsI-coated THGEM-based UV-photon imaging detectors were developed at WIS, as potential photo-sensors for Ring-Imaging CHerenkov detector (RICH) [141, 142]; THGEM-based UV detectors have been chosen for the upgrade of the RICH detector of Common Muon and Proton Apparatus for Structure and Spectroscopy (COMPASS) experiment at CERN, requiring $\sim$6 m$^2$ coverage of UV-photon detectors. It is the first particle physics experiment to use THGEM-based photon detectors [136].

A standard THGEM electrode (figure 1) consists of 0.4-0.8 mm thick FR4 plate, copper-clad on both sides. Holes of typically 0.5 mm diameter are mechanically drilled through the plate, with an hexagonal or square pattern of typically 1 mm pitch; etching is used to remove sharp conducting edges from the holes, resulting in an insulating rim of typically 10-100 μm width. The operation principle of a standard single-THGEM detector configuration is shown in figure 1-b.

Upon application of a voltage difference across the THGEM electrodes, a strong dipole field is created (typically 10-20 kV/cm) inside the holes; each of them acting as an independent electron multiplier. The detection process is as follows:

- PEs extracted from the gas by ionizing radiation in a conversion region above the electrode, or produced on a solid radiation converter (e.g. a photocathode), are drifted towards the THGEM holes along the drift field applied between its top face and the cathode.

(a) (b) (c)

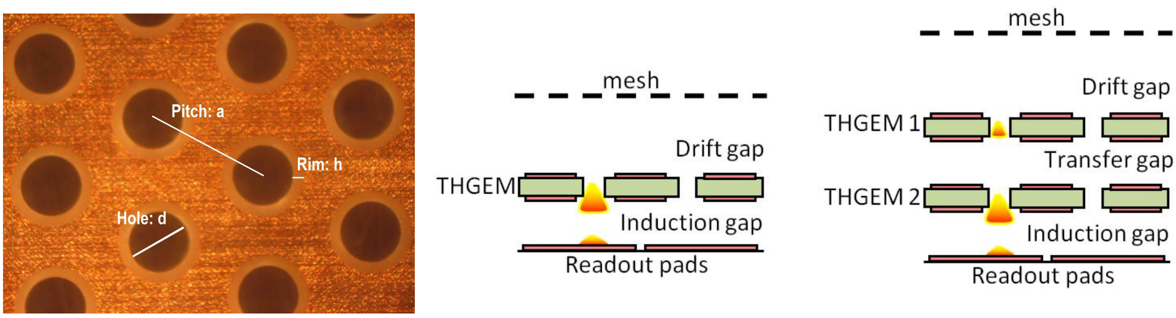


Figure 1: a) Typical THGEM electrode with hexagonal hole pattern. The relevant parameters are shown. b) Scheme of the single-THGEM detector concept with induction gap. c) Scheme of a double cascaded THGEM configuration.

- The PEs are focused into the holes by the strong local dipole field; a drift field of order 0.5 kV/cm typically results in high focusing efficiency [112].
- An avalanche ionization process develops in the holes, resulting in electron multiplication. The detector gain is a function of the voltage applied across the THGEM electrodes, and the gas type and pressure.
- The electrons (ions) are drifted towards the anode (THGEM-top or cathode) and collected. The movement of the electrons and ions induces a current pulse which is typically recorded from the anode; its amplitude is proportional to the deposited energy (number of PEs).

Different THGEM-based detector structures are shown in figure 2. Their operation principles, as well as the main associated R&D results (figure 2) are summarized in [59]. The original THGEM concept is that of a double-sided electrode with induction gap (figure 2-a). The Thick Well (THWELL) structure corresponds to a single-sided electrode directly coupled to the anode, (figure 2-b). In the RWELL, a resistive layer deposited on an insulating sheet is inserted in a THWELL-like configuration in-between the THGEM electrode and the anode (figure 2-c). In the Segmented Resistive WELL (SRWELL) the resistive layer is segmented into electrically separated regions prevents lateral charge spread (figure 2-d). Finally, the Resistive-Plate Well (RPWELL) described in section 1.4.2 is depicted in figure 2-e.

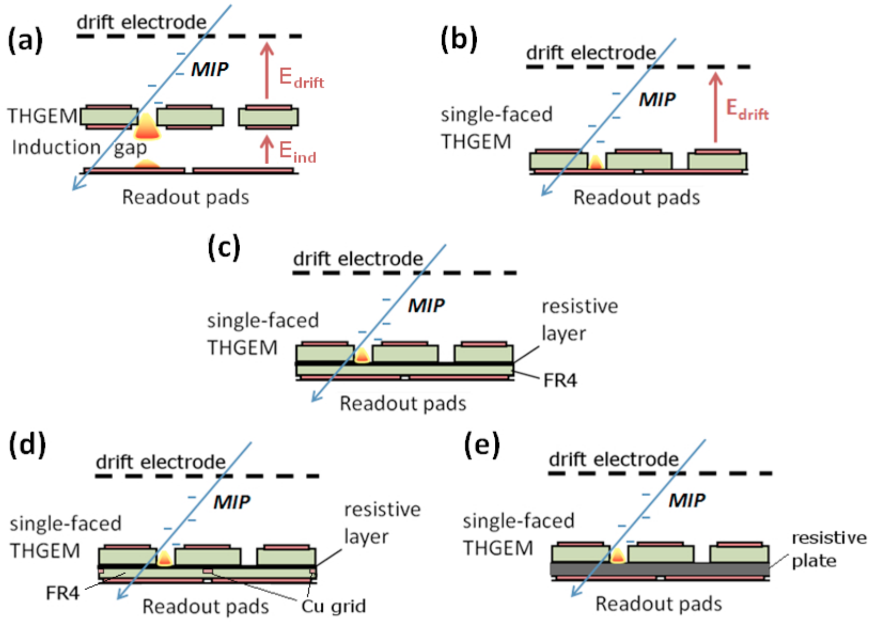


Figure 2: Different THGEM configurations. a) Double-sided THGEM with induction gap. b) Single-sided THGEM in WELL configuration. c) Resistive WELL. d) Segmented Resistive WELL. e) Resistive-Plate WELL.

A main feature of all THGEM detector configurations is the avalanche confinement within the holes, which considerably reduces secondary effects; it allowed reaching stable high-gain operation (in excess of $10^4$ -$10^5$ depending on the ionizing source) in a large variety of gas mixtures, including noble gases [111]. In the original THGEM detector, the electrode is separated from the readout anode by a few-mm wide induction gap (e.g. figure 1-b), it is possible to configure the voltages in order to extend the charge-multiplication region outside of the THGEM holes towards the induction gap [126].

Cascading two or more THGEM elements (figure 1-c) permits reaching higher gains, required for example for single photo-electron detection in RICH [141, 142] or in cryogenic Gaseous Photo-Multipliers (GPM) [133] developed at WIS for radiation imaging with liquid-xenon detectors for future Dark-matter experiments and for radiography with fast neutrons and $\gamma$ rays [76, 77]. The role of various geometrical and operational parameters in multi-stage configurations has been established, for optimal electron collection into the holes and the efficient transfer of avalanche electrons into successive multiplier elements [111].

Compared to single-element configurations, cascaded structures allow for higher maximal achievable gains and lower discharge probabilities (due to reduced charge density in the multiplier holes). On the other hand, multi-stage THGEM configurations are more expensive and, due to their larger thickness, they are less suitable for applications requiring few-mm thick detectors - like sampling elements in a (s)DHCAL (see section 1.5). Therefore, in the present study, the efforts have been focused on the development of single-element multipliers.

The THWELL, RWELL and SRWELL detectors are thin (~5-6 mm excluding readout electronics) single-element structures (without induction gap); they were studied extensively in the laboratory and in accelerator test-beam, giving satisfactory results in terms of gain and rate dependence [125, 127, 128, 92, 129]. On the other hand, the local resistance provided by a thin resistive film was not large enough to avoid discharges; in fact they were found to occur in RWELL detectors at the same rate as in THWELL [92], but with reduced intensity [59]. This lead to the idea of substituting the resistive layer with resistive-plates similar to the ones used in RPCs. This is the RPWELL concept [17] described in details in the next section ( 1.4.2).

### 1.4.2 The RPWELL detector

The **Resistive-Plate Well (RPWELL)** [17] consists of a THWELL configuration in which the single-sided THGEM electrode is coupled to a segmented readout anode (e.g. pads or strips) through a high bulk resistivity plate (figure 2-e). The RPWELL combines the properties of THWELL and RPC detectors. The latter employs anodes of highly resistive bulk materials ($10^7$-$10^{12}$ $\Omega$cm), that fully damp sparks but cause rate limitations, as explained in section 1.3.

Extensive laboratory studies of $30 \times 30$ mm$^2$ RPWELL prototypes, with various resistive materials, operated in Ne/(5%)$CH_4$ [17] demonstrated discharge-free operation at high gas-avalanche gains and over a broad ionization range, making it a suitable concept for the detection of minimum- as well as highly-ionizing particles. The gain-dependence on the incoming particle flux, demonstrated with the RPWELL with 0.6 mm thick Semitron ESD225 resistive plate was slightly better than the RWELL with 1 M$\Omega/\Box$ resistive film, with a 30% pulse-height drop over a 3 orders-of-magnitude increase in rate: from 10 to $10^4$ Hz/mm$^2$. This result can be compared to the performance of multi-gap RPCs made of ceramics, plastics and doped glass of lower resistivity values ($10^7$ -$10^{10}$ $\Omega$cm), that permit reaching rate capabilities of up to several $10^3$ Hz/cm$^2$ [143] only.

The results obtained with a charge-injector (a primary charge multiplier added to mimic highly ionizing events [92]), showed that the RPWELL configurations are robust relative to the THWELL and the RWELL [17, 92]. From these studies it appears that the onset of discharges occurs at the same number of primary electrons for the THWELL (no resistive layer) and for the RWELL with 1 M$\Omega/\Box$ and 10 M$\Omega/\Box$ thin resistive films. On the other hand, the RPWELL configurations did not spark even at hundred-fold higher injected charges. This hints to the fact that the role of the resistive layer at the tested resistivity values is not reducing the discharge rate, but quenching the intensity of the discharges, as discussed in section 1.3 and shown for example in [129] for different RWELL detector configurations.

The stability of the RPWELL indicates upon its potential stable operation in the presence of highly ionizing events. The drop in gain due to the high injected charge, was more pronounced for electrodes with the highest resistivity: glass and Bakelite. The discharge damping, rate dependence of the gain and the drop in gain with highly ionizing events can be explained by the long time-constant of the highly-resistive plates (see section 1.3); it can be estimated by approximating the detector as a parallel-plate structure, using $\tau = \rho \cdot \epsilon$, where $\tau$ is the time constant, $\rho$ is the bulk resistivity, and $\epsilon$ is the dielectric constant of the plate[6].

While some of the operation principles of the RPWELL are similar to that of the RPC, the RPWELL offers some advantages. First, the region of multiplication is confined to the holes. As a result, the RPWELL can be preceded by large conversion/drift volumes and the total charge produced in the avalanche does not depend on the position of the interaction. The closed geometry also limits the avalanche divergence by photon feedback and the RPWELL can operate with standard counting gases like Ne/(5%)$CH_4$ or Ar/(7%)$CO_2$, compared to RPCs where very specific gas mixtures are needed. These, together with the field structure, also reduce the operation voltage of the RPWELL to lower values compared to that of RPC chambers. Note that, contrarily to the RPWELL case (in which the anode is grounded), in the RPC the high resistivity material is kept at few kV potential, requiring a perfect surface for stable operation and limiting the choice of available materials to the ones capable to sustain such High Voltage (HV) values without changing their properties.

In the present work, which aims at a DHCAL application (section 1.5), we will demonstrate that this thin (∼4-6 mm excluding readout) single-element detector can

[6] Under the caveat discussed in section 1.3.2

satisfy all the requirements of a sampling element, and it can operate efficiently in a discharge-free mode over a broad dynamic range also when assembled in large prototypes.

## 1.5 Particle flow and Digital Hadronic Calorimetry (DHCAL)

Since the discovery of the Higgs Boson, the challenge for the high-energy physics community is measuring precisely its properties and determining its nature. A precise knowledge of its mass, its decay products, branching fractions and couplings to the standard model particles will provide an important insight into fundamental questions such as the mechanism by which elementary particles acquire mass, and how massive matter was formed in the early universe. However, some of these questions cannot be answered at the LHC; others cannot be answered with sufficient precision. This, together with the hope to discover BSM physics, motivates the design and development of future colliders and experiments. Among the candidate projects are various electron-positron colliders; the ILC [10], the CLiC [11], the CEPC [13] and the ee-FCC [12].

Many new physics scenarios, and the measurement of different characteristics of the Higgs boson, involve hadronic-decay channels which require excellent jet-energy resolution. Therefore, future high-energy physics experiments place severe demands on hadronic calorimetry. For example, in the specifications of the calorimeters for experiments at the ILC, the required jet-energy resolution is $30\%/\sqrt{E}$ or better [10] (corresponding to $\sigma$/E= 3% for 100 GeV jets). This resolution is roughly three times better than that achieved with the ATLAS and CMS calorimeters, even with the implementation of **Particle-Flow (PF) techniques** [15, 16].

In the PF approach the jet energy is reconstructed combining the information from all the detector subsystems, trying to measure separately the energy of all visible particles in an event. The reconstructed jet energy is the sum of the energies of the individual particles. Charged particles constitute over 60% of the particles in a jet, and their momentum can be measured with the highest precision in the tracking system, whereas photons and neutral hadrons deposit their energy in the calorimeters only.

The main idea of PF is to improve the jet-energy resolution by minimizing the use of the Hadron Calorimeter (HCAL), where large fluctuations due to fundamental hadronic processes are unavoidable. The PF method relies on the imaging capability of segmented calorimeters, and on the correct assignment of calorimetric energy deposition to individual particles. In this application, the pattern recognition performance of the reconstruction software - the Particle-Flow Algorithm (PFA) - becomes crucial; the jet energy resolution is a combination of the intrinsic detector performance and the performance of the PFA software.

At low energies, the intrinsic calorimeter resolution is the main factor limiting the jet energy resolution, whereas at high energies (more than 100 GeV) the jets become more collimated, and the confusion in the energy depositions assignment to the individual particles becomes the dominant limit. The most advanced PFA is Pandora PFA [144] specifically developed in the context of the ILC detectors. SiD [19] and the ILD [20], both incorporating PFA as a basic element of their philosophy and design, including a highly segmented Electromagnetic Calorimeter (ECAL) and HCAL. The study presented in [144], considering an analogue scintillator tiled calorimeter demonstrates that PF calorimetry with Pandora PFA can meet the challenging ILC jet energy resolution goals.

An example of a simulated 100 GeV jet event in the ILD seen from the PFA approach is showed in figure 3-a. A schematic description of the ILD quadrant is shown in figure 3-b; it comprises a powerful silicon-pixel vertex detector, silicon-strips tracker, silicon-tungsten ECAL, highly segmented HCAL, and a muon identification system. Notice that both the ECAL and the HCAL are located inside the 5 T magnetic field created by a superconducting solenoid, necessary for applying the PF analysis. PF calorimetry places stringent requirements on the granularity of the ECAL and HCAL. For the entire SiD HCAL, with $10^2$ $m^3$ total volume, the total number of readout channels will be $4{\cdot}10^7$ which is one of the biggest challenges for the HCAL system. To overcome this problem, the possibility of using a digital readout rather than analogue one was proposed, namely a DHCAL. The DHCAL concept relies on the linear relation between the number of pads fired and the incoming hadron energy.

In this context, gas detectors (such as RPC, cascaded GEMs, THGEM and MICROMEGAS) become potential sampling element candidates.

The baseline design of the SiD hadronic calorimeter is a DHCAL comprising 40 layers of stainless steel absorber plates separated by 8 mm gaps, which should incorporate the active sampling elements with their $1{\times}1$ $cm^2$ square pixels and readout electronics. The DHCAL sampling elements (glass RPC in the baseline design) need to fit within the 8 mm gaps between the absorber plates (together with the readout electronics), and should perform at the highest *efficiency* (close to 100%) and lowest average *pad multiplicity* (ideally 1 pad firing per track segment), to provide the conditions for the PFA to work at its best. Confusion between hits belonging to closely-spaced showers, and non-linearity between shower energy and number of digital hits in the calorimeter are two main challenges to a proper event reconstruction.

A worldwide collaboration - Calorimeter for the Linear Collider Experiment (CALICE)[7] (including the WIS team) - is active in the particle-flow calorimetry concept

[7]The CALICE collaboration

(a)

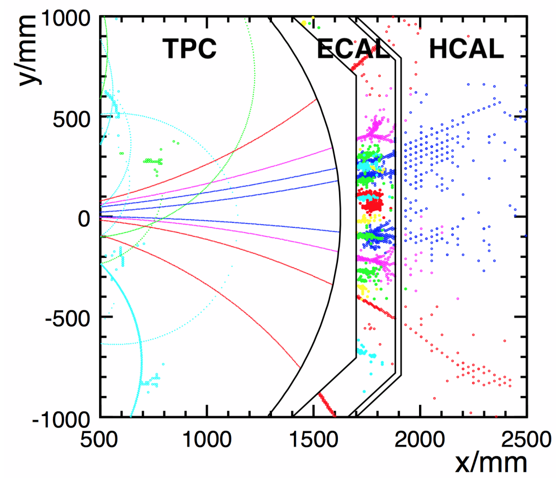


(b)

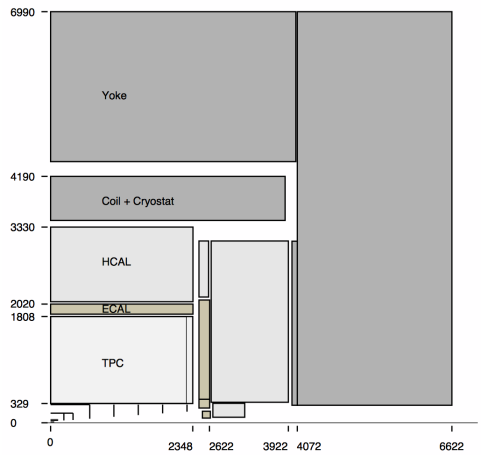


Figure 3: a) Pandora PFA reconstruction of a 100 GeV jet in the MOKKA simulation of the ILD detector. In the particle-flow approach, calorimeter hits are grouped into clusters that are associated with a specific particle initiating a shower. The energy of neutral particles is measured by counting the number of hits in the calorimeter cluster. Calorimeter clusters associated with a track in the tracking system are identified with charged particles and their momenta are measured with better precision. b) A schematic view of the ILD detector with its components: TPC, ECAL and HCAL.

R&D. Several calorimeter prototypes were built and tested in beam, and the results were compared with that of Monte Carlo simulations. The most recent results of this effort are summarized in [145].

Beam tests of a 1 m$^3$ RPC-DHCAL prototype [146] gave a first demonstration that digital hadronic calorimetry, based on hit counting only, works both conceptually and technologically. Single-particle energies were reconstructed with a resolution comparable to that obtained with analog methods [147, 145]. On the other hand, digital reconstruction schemes have not yet been implemented into the Pandora PFA, therefore estimations of a DHCAL jet-energy resolution are not yet available. For the same reason, no detailed study addressed the effect of the average pad multiplicity on the hadron energy reconstruction and close showers separation in DHCAL (some preliminary studies on RPC digitization can be found in [148]). However, the common paradigm is that the lower the average pad multiplicity the better the energy resolution and the shower-to-shower separation. Under this assumptions, we can compare the results obtained by the different technologies considered for future DHCAL applications.

Sampling elements based on RPCs, the baseline technology for the SiD hadronic calorimeter, have yielded so-far an average multiplicity of 1.5-2 at 90-95% efficiency [149]. Elements based on MICROMEGAS, have demonstrated superior properties: 98% efficiency with a 1.1 average multiplicity [150]. Elements based on the double-GEM, have shown a multiplicity of 1.3 at 95% efficiency [151]. THGEM -detectors were first suggested by the WIS team as potential sampling element for the SiD DHCAL in [125]. This possibility was studied further with $100 \times 100$ mm$^2$ THGEM and THWELL detectors. Using thin ($\leq$6 mm) configurations (to cope with the thin sampling gaps requirement), a detection efficiency greater than 98% was reached at pad multiplicity in the range 1.1-1.2 [127, 128].

In parallel to the DHCAL concept, a sDHCAL with two different energy-threshold values is being developed. The advantage would be to overcome the non-linear response (between the number of fired pads and the energy of the incoming hadron) of a DHCAL at high energy, when the hadron shower density becomes comparable to the readout segmentation. Results obtained with a glass-RPC sDHCAL prototype [152] show that the measured degradation of the energy resolution for high-energy hadrons (above 30 GeV) can be mitigated by a proper calibration of a three-thresholds readout.

Since THGEM-based detectors are proportional ones, namely the amplitude of the measured signal is proportional to the deposited energy, they would be suitable candidates also for sDHCAL. These results place THGEM-like detectors as very competitive sampling-element candidates for sDHCAL. Hence, further investigations were conducted, focusing on the RPWELL detector; the results obtained during the present work are presented in chapter 3.

# Chapter 2

# Methods

## 2.1 The RPWELL detectors

Different RPWELL prototypes of increasing size (up to $500 \times 500$ mm$^2$) were built with two main purposes: demonstrate the capability of the RPWELL concept to meet the requirements of a DHCAL or sDHCAL, and to scale up the detector to large areas. The latter is a mandatory step towards the realization of a (s)DHCAL prototype as well as the usage of the RPWELL detector in other applications requiring large area coverage. When relevant, the assembled prototypes were used for dedicated studies of RPWELL-related physics characteristics. Examples are the study of position resolutions and the study of the effect of frames edges on the detector performance.

The different detectors assembled are listed in table 2.1, along with their main properties and experimental usage. Detailed description of each detector including the main assembly stages is given in appendix A.

### 2.1.1 Resistive Plate choice and assembly methods

Two different commercial materials were selected for the Resistive Plates (RPs): Semitron ESD225[1] electro-static dissipative polymer and a doped silicate-glass [153], having typical bulk resistivity values of $10^9$ Ωcm and $10^{10}$ Ωcm respectively. This choice is driven by experience gained in previous studies which showed that good performance can be obtained with an RPWELL detector using materials in this range of resistivity [17, 154]. In particular, discharge-free operation was achieved at the cost of relatively moderate gain loss (30%) over 4 orders of magnitude of the incoming particles flux[2].

From the practical point of view, it is difficult to find commercial materials that present at the same time the desired mechanical and electrical properties. The Semitron ESD225 polymer is a good candidate, but it has the disadvantage of being available only in thick plates of several mm, which requires precise and costly machining to reduce its thickness to sub-mm values. Moreover, some mechanical aspects make Semitron ESD225 problematic: it cannot be glued properly by common epoxies; it absorbs humidity and suffers from large humidity- and temperature-dependent expansion coefficients. The doped silicate-glass does not have these problems, but it can be produced only in area of $300 \times 300$ mm$^2$. Furthermore, it is fragile when produced in sum-mm thicknesses, making the coupling of the glass RP to the anode challenging. It is likely that the conception of large-area RPWELL detectors will require the development of industrially-made application-tailored RP materials.

Other than the RP material itself (its electrical and mechanical properties), a proper coupling to the readout anode is essential for ensuring the required detector performance. Thus, the coupling of the RP to the anode deserves careful considera-

[1] www.quadrantplastics.com

[2] It should be emphasized that the exact mechanism of discharge quenching by a RP is not yet well understood. Thus, the RP is chosen based on experience and available materials in the market.

tion. Two different approaches were investigated:

- Keeping the RP electrically decoupled from the anode. In this case, the charge produced by electron multiplication in the gas does not reach the anode. The charge movement induces a bipolar signal on the anode, and it must be neutralized via an additional path to ground. Such a scheme is implemented for example in detectors with a resistive layer like RWELL [129], MICROMEGAS [103] or TGC [43]. Since the signal lateral spread on the readout anode is usually large, we used this approach in a small prototype dedicated to position-resolution studies (see section A.4.1).

- Granting a direct conductive path between the RP and the anode. In this configuration, the charge is collected and neutralized on the readout anode and the induced signal is contained within a smaller region. This option is more suitable for a DHCAL application, where the readout-anode is pixelated into small pads (e.g. $10 \times 10$ mm$^2$); in a digital recording of individual particles, the average pad multiplicity per hit must be kept minimal - as close as possible to 1.

We developed two different methods for direct coupling of the RP to the readout anode (the second option above): a) one-to-one contact and b) graphite/epoxy glue. One-to-one contact between the RP and the readout segments requires patterning the RP with conductive paint in accordance with the readout segmentation, coupling them one by one with a conductive glue [1]. The limitation of this procedure is that it can be applied easily only to anodes which are pixelated into large pads. Gluing the RP to the anode with the graphite/epoxy procedure described below is a simpler method. Furthermore, it can be applied to any anode geometry, including small pads and thin strips. The method consists in coating the RP with a graphite film of several M$\Omega/\square$ resistivity and then gluing it with epoxy to the anode. The epoxy mixes with the graphite, resulting in an intermediate layer having relatively large surface resistivity and moderate bulk one (as confirmed by the dedicated experiment described in appendix B). Thus, the preferred path to ground is through the resistive layer to the readout anode.

The one-to-one contact technique was used in the assembly of the detectors described in sections A.1, A.2, A.3. Graphite/epoxy gluing was used in the assembly of the prototypes described in sections A.4 and A.5, and it was tested in a dedicated experiment described in appendix B. More details about the techniques and their implementation methods are available in appendix A, along with the description of the assembly of the different RPWELL chambers.

### 2.1.2 RPWELL chambers design and assembly

In parallel to the physics studies, effort was made to evolve from an R&D-oriented design to an experiment-targeted prototyping approach. In the R&D-oriented design, the electrode structures were mechanically mounted inside gas vessels using screws and nuts, leaving the possibility to modify them at will. In the experiment-targeted prototyping approach, the detector parts were assembled and glued permanently in a determined configuration. This is a fundamental step towards the production of large prototypes for target applications, that require optimized dimensions of the elements, optimized material thicknesses and gas gaps, minimal dead areas, etc. It requires careful design of the detector parts and a well-defined assembly protocol to produce reliable detector elements and reproducible results.

The largest R&D-oriented RPWELL assembled was $300 \times 300$ mm$^2$ large, with a Semitron ESD225 RP directly coupled to the anode patterned into $10 \times 10$ mm$^2$ readout pads. Following the experiment-targeted approach, several prototypes of different sizes ranging from $100 \times 100$ mm$^2$ to $500 \times 500$ mm$^2$ were designed, assembled and investigated. A summary of the produced and tested chambers is given it table 2.1. The detectors are described in details in appendix A.

| size [$mm^2$] | RP thickness [mm], material | THGEM thickness [mm], holes pattern | gases | purpose | notes |
|---|---|---|---|---|---|
| $30\times30$ | 0.6, Semitron ESD225 | 0.8, square-segmented | Ne/(5%)$CH_4$ | edge effects | different distances from side frame to THGEM holes |
| $100\times100$ | 0.4, Semitron ESD225 | 0.86, square-segmented | Ne/(5%)$CH_4$, Ar/(5%)$CH_4$, Ar/(7%)$CO_2$ | DHCAL, test-beam studies | modular assembly, patterned RP, pads readout, 5 mm drift |
| $300\times300$ | 0.4, Semitron ESD225 | 0.86, hexagonal, 6 separate segments | Ne/(5%)$CH_4$, Ar/(5%)$CH_4$, Ar/(7%)$CO_2$ | DHCAL, test-beam studies, scaling-up | modular assembly, patterned RP, pads readout, 5 mm drift |
| $100\times100$ | 0.4, Semitron ESD225 | 0.8, square-segmented, 9 tiles | Ne/(5%)$CH_4$, Ar/(5%)$CH_4$, Ar/(7%)$CO_2$ | DHCAL, test-beam studies, assembly methods | glued, pads readout, RP coupling by graphite and epoxy |
| $100\times100$ | doped silicate-glass | 0.8, square-segmented, 9 tiles | Ne/(5%)$CH_4$ | position resolution, test-beam studies, assembly methods | glued, strips readout, RP coupling by graphite and epoxy |
| $500\times500$ | doped silicate-glass | 0.8, square, 2 tiles | Ar/(7%)$CO_2$ | scaling-up, test-beam studies, assembly methods | glued, strips readout, RP coupling by graphite and epoxy, 3 mm drift |

Table 2.1: The assembled RPWELL detectors features

### 2.1.3 Operation gases

All the RPWELL detectors were operated in flow mode in Ne/(5%)$CH_4$ gas mixture prior to their operation in argon-based gas mixtures: Ar/(5%)$CH_4$ and Ar/(7%)$CO_2$. For the first time, single-stage THGEM-based detector was capable of operating with Ar-based gas mixtures in a discharge free mode.

The operation in argon mixtures required higher applied potentials with respect to neon, to reach similar avalanche gains. However, argon mixtures present two main advantages: (1) larger average number of MIP-induced electron-ion pairs; e.g. in 1 cm of gas in standard conditions the numbers are 94 in argon, and 39 in neon [48], allowing to use a smaller conversion/drift gap while maintaining high detection efficiency. (2) Argon is considerably cheaper than neon, hence more attractive for applications requiring large-area coverage, such as the (s)DHCAL.

It is mainly for the second reason that the successful transition from neon-based to argon-based gas mixtures is a major success of this research. Among the different argon-based mixtures, the usage of the non-flammable $CO_2$ instead of $CH_4$ as a UV photon quencher could be convenient for safety reasons. The final gas mixture should be optimized for the foreseen application, taking into account other properties. Examples are electron diffusion, which affects the position resolution (see section 3.2.2), electro-negativity, which affects the down charging processes [155, 156], etc.

## 2.2 Laboratory test setups

### 2.2.1 Large area x-y scanner

A fully-automated x-ray scanning machine (installed at the TGC production facility at WIS (figure 4)), was used for performing a "preliminary", pre-test-beam stress-test of the largest $500 \times 500$ mm$^2$ RPWELL detector; it aimed at enlightening eventual weak points or "hot spots". The irradiation facility consists of an Amptec mini-X x-ray gun with silver target providing a photon beam peaked at 22 keV, mounted on a x-y stepper motor system which is able to scan a surface of a few $m^2$. This setup was used to characterize the entire active region of the $500 \times 500$ mm$^2$ RPWELL detector described in section A.5 over a wide range of irradiation fluxes. Different collimators of 5 mm and 30 mm diameter were used, scanning with step sizes of half the collimator size. During a scan, a measurement of the current drawn by each electrode (2 THGEM sectors and the cathode) was performed, using a software kit that synchronizes and stores the x-y position with the HV power supply monitoring.

The current value was sampled at 1 Hz rate. The energetic x-rays did not permit a direct measurement of the detector gain; the resulting x-ray induced photoelectrons ($\sim$22 keV) have a $\sim$cm range in Ar/(7%)$CO_2$ gas at atmospheric pressure, with a random emission direction. Hence, the total number of electrons extracted in the detector drift gap fluctuates greatly from event to event.

The $500 \times 500$ mm$^2$ detector was investigated as following:

1. Stability: the detector was irradiated with maximum x-ray flux for 9 hours, at the position of a spacer, and at another position far from any spacer. (see appendix A.5 for the detector geometry). With this test, charging-up effects should become visible, through variations in the measured current.

2. Uniformity and stability: the entire detector area was scanned by the broader x-ray beam (30 mm collimator) in steps of 15 mm, with different irradiation times of 30 s or 120 s per spot, at different detector voltages and x-ray fluxes. In addition, a finer scan of the area of a single resistive-glass tile was performed.

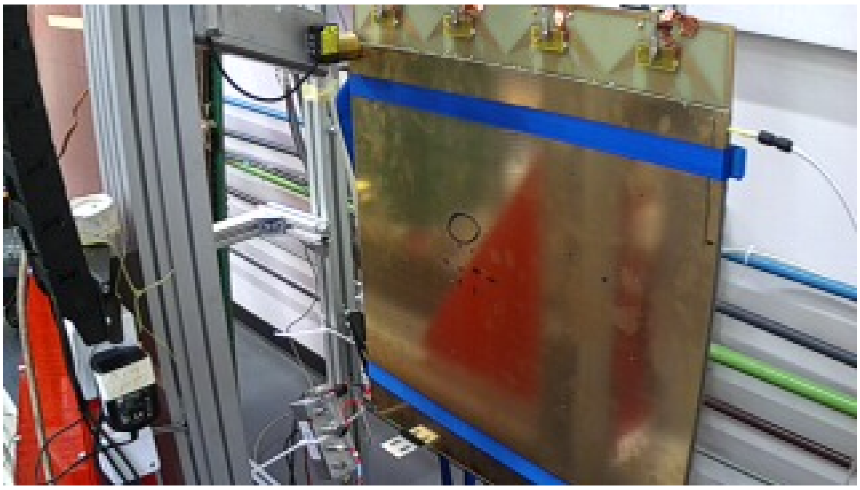

Figure 4: The $500 \times 500$ mm$^2$ RPWELL prototype mounted in the large x-y scan system with the silver x-ray gun (at the left-top corner of the chamber).

### 2.2.2 Cosmic rays test-bench

Cosmic rays were used in the laboratory to characterize the detector response prior to test-beam experiments.

The setup was very similar to the one described in section 2.3.1, based on the APV25/Scalable Readout System (SRS) readout electronics [157, 158], but without tracking system. Three scintillators were used in coincidence to select the events occurring in a $100 \times 100$ mm$^2$ detector region. The data were also analyzed in a similar way as described in section 2.3.1.

## 2.3 Test-beam experiments

Test-beam experiments were carried out at the CERN-SPS H4 beam line, with 150 GeV muons and pions at flux in the range between $10^2$ - $10^5$ Hz/cm$^2$. All the $100 \times 100$ mm$^2$, the $300 \times 300$ mm$^2$ and the $500 \times 500$ mm$^2$ RPWELL detectors described in section 2.1 have been tested in this beam. A schematic representation of the test-beam setup is shown in figure 5. It consists of scintillators operated in coincidence, providing the trigger to the readout electronics; a MICROMEGAS tracker, and the tested RPWELL chambers, which were placed along the beam line in-between two tracker elements.

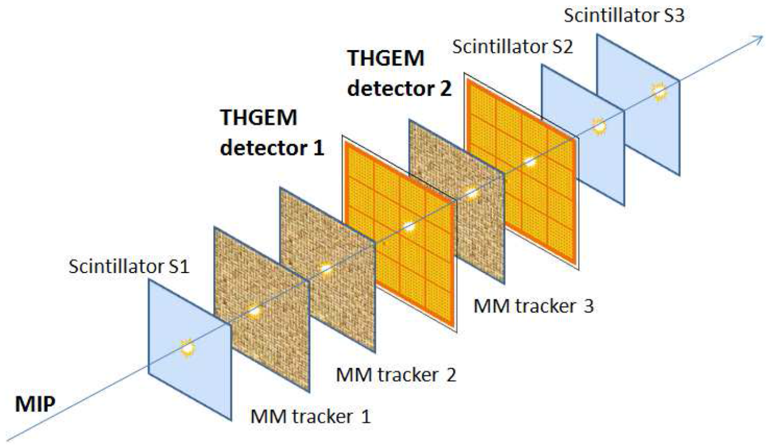


Figure 5: The test-beam setup scheme, comprising RPWELL prototypes mounted in-between the tracker elements.

### 2.3.1 The slow control, tracking and readout system

The tracking system (based on the CERN-RD51 telescope [159, 160]), the data acquisition system (based on the APV25/SRS readout electronics [157, 158]) and the analysis framework are described in detail in [1]. The tracker comprises three scintillators in coincidence to provide a clean trigger, and three MICROMEGAS chambers for precise track reconstruction. All the electrodes of the RPWELL and of the tracker were individually biased using CAEN A1833P and A1821N HV power-supply boards, remotely controlled with a CAEN SY2527 unit. The voltage and current in each channel were monitored and stored. All HV inputs were connected through low-pass filters. We could also monitor the current flowing through the RPWELL detector anode as a function of time, using a sensitive ammeter [161]. The MICROMEGAS chambers were operated in standard gas mixture (Ar/(7%)$CO_2$) and HV configuration to provide high detection efficiency and precise localization. All the detectors of the tracker and the tested RPWELL were read out by APV25 chips; their shaping time of ~75 ns is much shorter than the full RPWELL typical rise-time (1-2μs).

### 2.3.2 DAQ and analysis framework

All the APV25 chips connected to the tracker chambers and the tested RPWELL detectors were read out using the mmDAQ software [162]. Dedicated pedestal runs, in which the trigger is provided by the system clock, were taken before each physics run. mmDAQ uses the pedestal to extract the baseline and noise level for each channel. The baseline is corrected for, and a channel-by-channel on-line threshold is set using a common Zero-order Suppression Factor (ZSF) (for details see [1]).

The raw data are stored in a root tree which comprehends for each hit: chip id, channel id, signal peak (10-bit ADC value), time-stamp. In the offline analysis, each channel id was mapped to a specific position in the relevant detector. For every event, the hits in each detector element were grouped into clusters of neighbors; the position of the cluster being defined as the charge-weighted average of the channels position.

A dedicated software [160] provided the slope of the reconstructed track and its position in the telescope coordinates system. The RPWELL local coordinate system was aligned with that of the tracker using a dedicated alignment analysis, which applied a linear fit to the correlation plot of the clusters positions in the two systems.

### 2.3.3 Definition of the main measured properties

The *global detection efficiency* of the RPWELL detector was calculated as the fraction of particle tracks matched to a cluster within a certain distance W. The *average pad (or strip) multiplicity* was the average number of channels contained in a cluster.

Using the current monitor, the *discharge probability* was defined as the number of measured current spikes divided by the number of hits in the active region of the detector (i.e., in the total area covered by the crossing beam). The number of discharges was extracted directly from the power supply log files by counting the resulting spikes in the supplied current monitor. Due to the low rate of the muon beam, only pion runs were used to estimate the discharge probability. Since pions are prone to induce highly-ionizing secondary events, this study yielded an upper limit of MIP-induced discharge probability.

In the measurements of position resolution, the *residual* is defined as the distance between the track position and the position reconstructed by the RPWELL. In the simulation (section 2.4), the residual is defined as the difference between the simulated muon position and the position reconstructed by the RPWELL.

### 2.3.4 Detector working point

The THGEM electrodes were biased at a negative voltage. The difference with respect to the grounded anode ($\Delta V_{\mathrm{RPWELL}}$) was varied throughout the experiments. The drift voltage was kept constant (except in some dedicated measurements): $\Delta V_{drift}$= 250 V -corresponding to a drift field of ~0.5 kV/cm across the 5 mm drift gap. Measurements at different $\Delta V_{\mathrm{RPWELL}}$ values were analyzed to fix the optimal working point, scanning the off-line ZSF and the W parameters.

The detector working point, in terms of $\Delta V_{\mathrm{RPWELL}}$, ZSF and W values, was adjusted to optimize its performance in each gas mixture. In the detectors with pads readout aiming at a DHCAL application, the target was reaching high global detection efficiency at low average pad multiplicity. In the detector with strips readout, the target was achieving the best position resolution.

## 2.4 Monte Carlo Simulations

A microscopic simulation of the RPWELL operation was implemented. The main tools used and their role is schematically presented in figure 6:

- Garfield simulation framework [53] - includes all relevant physics processes governing the electron and ion interactions and transport in gases.
- neBEM solver [163] - produces a field map, solving the Maxwell's equations in the provided geometry and voltage configuration.
- Heed [164] - provides the energy and position of PEs extracted by charged particles depositing their energy in a gas
- Magboltz [54] - contains the parameters of charge transport in gas

C++ scripts and ROOT[3] were used to produce the relevant calculations and plots.

### 2.4.1 Position resolution

To study in detail the localization properties of the $100 \times 100$ mm$^2$ tiled glass-RPWELL detector with strips readout, a Monte Carlo simulation was implemented. The simulation was performed on an event-by-event basis. For each event, we used as an input

[3]https://root.cern.ch

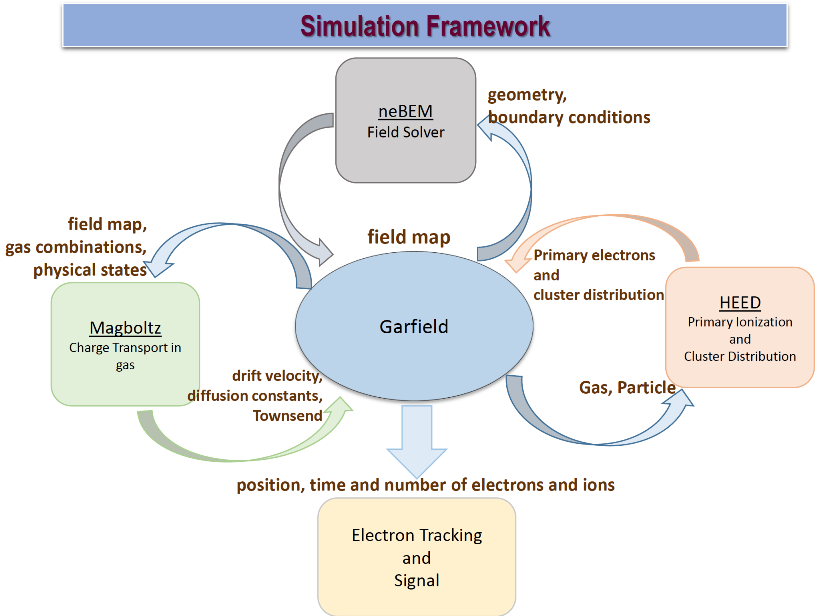


Figure 6: The simulation tools scheme.

a combination of measured quantities (such as signal shape) and simulated quantities[4] (such as electrons drift), to reproduce the following physics processes:

1. Ionization of PE clusters in the drift gap, along the trajectories of a 150 GeV muon.
2. PEs drift into the THGEM holes (including longitudinal and transverse diffusion).
3. The avalanche formation in the high-field region within the THGEM holes.
4. Current-signal induction on the anode strips by the drifting charges. Both the drift of the electrons towards the anode and the drift of the ions towards the THGEM top were considered.

[4]The simulation tools were Garfield simulation framework [53], together with the neBEM solver [163], Heed [164] and Magboltz software [54]

5. Reconstructed position and the residuals pattern.

The details of the simulation process are given in [4].

# Chapter 3

# Results

As described in chapter 1, the present research aimed at developing large-area cost-effective detector concepts with moderate, sub-mm, position resolution for efficient detection of charged particles. In particular, the detectors were investigated in the context of sampling elements in DHCAL or sDHCAL for experiments in future electron-positron colliders.

For that purpose, different RPWELL detector prototypes were developed as summarized in table 2.1 and detailed in appendix A. With these prototypes, the scalability of the RPWELL concept from $100 \times 100$ mm$^2$ to $500 \times 500$ mm$^2$ was demonstrated.

In the framework of the (S)DHCAL application, prototypes of $100 \times 100$ mm$^2$ and $300 \times 300$ mm$^2$ area, with $10 \times 10$ mm$^2$ pad readout were assembled. The different prototypes were built using two different RP materials, that were coupled to the readout anode in two ways (section 2.1.1). The prototypes were characterized in test-beam under muon and high-rate pion beams at CERN-SPS (section 3.1). Their response in terms of gain, detection efficiency, pad multiplicity, rate capability, position resolution, and stability was investigated in different gas mixtures.

A $500 \times 500$ mm$^2$ RPWELL prototype with strips readout[1] was designed and assembled, as a step towards the production of large-area sampling elements for (s)DHCAL. Systematic investigations of this detector were carried out both in the laboratory, with cosmic rays and an x-ray scanning-machine, as well and in test-beam; being the first-ever built $500 \times 500$ mm$^2$ RPWELL, attention was paid to the operation stability and uniformity under different irradiation conditions (section 3.3).

Ancillary R&D studies were conducted on small- and medium-size detector prototypes. Using a $100 \times 100$ mm$^2$ RPWELL with strips readout, its intrinsic position resolution was assessed. Complementary to the test-beam measurements, Monte Carlo simulations were performed in order to understand the underlying physics processes governing the detector performance; the results are presented in section 3.2. The effects of edges and frames on the detector performance was studied in the laboratory using a dedicated $30 \times 30$ mm$^2$ RPWELL detector; the experiment is presented in appendix C and its results are compared with test-beam measurements of the $500 \times 500$ mm$^2$ detector with strip readout (section 3.3).

Overall, the present results prove the capability to operate a $500 \times 500$ mm$^2$ RPWELL detector compatible with the requirements of a DHCAL or sDHCAL and place the RPWELL as a competitive technology for these applications. They provide valuable input for possible future optimization of the design of these sampling elements, as well as a deeper understanding of the RPWELL detector operation in its basic principles. A comprehensive discussion of the present findings is given in chapter 4.

[1] In this prototype, the usage of the strip anode rather than a pad one was motivated by cost considerations. The goal was to study the detector design and assembly. Thus, the most economical solution was preferred. The same procedures can be applied identically to any anode pattern.

## 3.1 In-beam evaluation of RPWELL prototypes with padded readout

Various RPWELL prototypes with padded-anodes of $10 \times 10$ mm$^2$ size (see table 2.1) were evaluated in four test-beam campaigns in winter 2014 [1], summer 2015 [2, 3], and summer 2016 [4]. Considering the requirements of a DHCAL, the performance of the detectors was studied in terms of effective gain, average detection efficiency, average pad multiplicity, rate capabilities and stability under high irradiation fluxes.

Two different methods to couple the RP to the anode were investigated: 1) by a channel-by-channel conductive path (section 3.1.1) and 2) through an epoxy/graphite layer (section 3.1.2). The main achieved results are presented for the two methods.

The geometry and assembly methods of the detectors are described in detail in appendix A. For the details about the RP choice and its coupling to the readout anode see section 2.1.1.

### 3.1.1 Channel-by-channel conductive path coupling

Two RPWELL detector prototypes were built using this technique, $100 \times 100$ mm$^2$ and $300 \times 300$ mm$^2$, as described in appendices A.2 and A.3 respectively. They were operated in the test-beam in three gas mixtures: Ne/(5%)$CH_4$, Ar/(5%)$CH_4$ and Ar/(7%)$CO_2$. The results obtained with these prototypes are summarized below. Details can be found in [1, 3, 2].

A remarkable achievement was the ability to operate the RPWELL detector in a discharge-free mode also in argon-based gas mixtures, at low average pad multiplicity. No other single-stage THGEM- or GEM-based detector has these capabilities, which were demonstrated with small- ($100 \times 100$ mm$^2$) and large- ($300 \times 300$ mm$^2$) area detector prototypes [2].

### Efficiency and pad multiplicity

Figure 7-a shows the Most-Probable Value (MPV) of the charge spectrum, as a function of the RPWELL operation voltage $\Delta V_{RPWELL}$. Figure 7-b shows the detection efficiency as a function of average pad multiplicity. Both measurements were carried out with the $100 \times 100$ mm$^2$ detector prototype at $\sim$100 Hz/cm$^2$ muon beam. The corresponding measurements, conducted with the $300 \times 300$ mm$^2$ detector prototype, are shown in figure 8. For both prototypes, the drift gap was 5 mm, and the detector was operated in Ne/(5%)$CH_4$, Ar/(5%)$CH_4$ and Ar/(7%)$CO_2$ at effective-gain values ranging from 130 to $1.5 \cdot 10^4$. The operation voltage $\Delta V_{RPWELL}$ was ranging from 800 V to 950 V in Ne/(5%)$CH_4$, and from 1550 V to 1750 V in argon mixtures.

(a) (b)

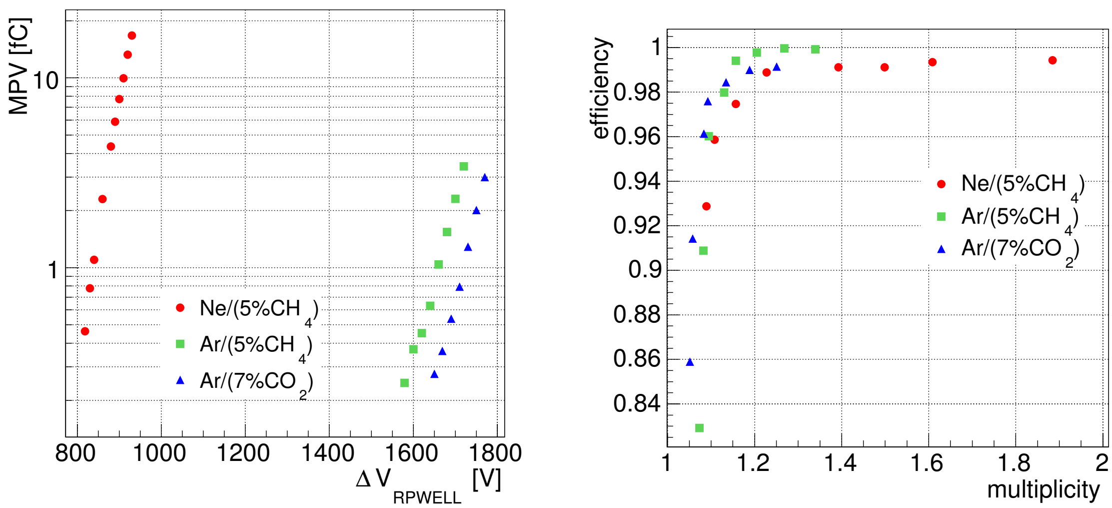


Figure 7: Using the same data-set: a) The charge MPV measured by the $100 \times 100$ mm$^2$ RPWELL detector in $\sim$100 Hz/cm$^2$ muon beam for different operation voltage ($\Delta V_{RPWELL}$) values in the three gas mixtures Ne/(5%)$CH_4$, Ar/(5%)$CH_4$, Ar/(7%)$CO_2$. b) The detector efficiency as a function of the pad multiplicity. Data recorded by APV25/SRS readout electronics.

At an effective gain of $2.7 \cdot 10^3$ (measured charge MPV of ∼2 fC), corresponding to a gas gain of $\sim 10^4$, an efficiency of more than 98% at a pad multiplicity of 1.2 was reached in all gas mixtures, with both detectors. These results were obtained using the APV25/SRS readout. Note that the optimal operation conditions depend on both the detector response and the readout electronics used. Thus, the quoted results are not independent of the readout system.

(a) (b)

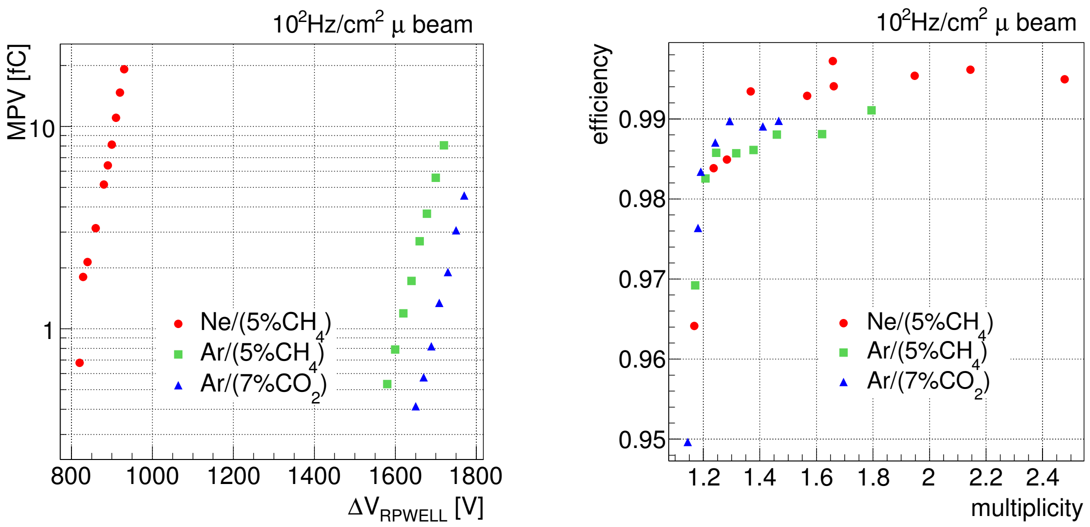


Figure 8: Using the same data-set: a) The charge MPV measured by the $300 \times 300$ mm$^2$ RPWELL detector in ∼100 Hz/cm$^2$ muon beam as a function of the operation voltage $\Delta V_{\mathrm{RPWELL}}$. b) The global detection efficiency as a function of the average pad multiplicity for different $\Delta V_{\mathrm{RPWELL}}$ values. The detector was operated in $\sim 10^2$ Hz muon beam in Ne/(5%)$CH_4$, Ar/(5%)$CH_4$ and Ar/(7%)$CO_2$ gas mixtures. Data recorded by APV25/SRS readout electronics.

The tracker precision allowed studying local effects like the efficiency and pad multiplicity as a function of the track distance from the pad border. This is shown in figure 9 and figure 10 for the $100 \times 100$ mm$^2$ and for the $300 \times 300$ mm$^2$ RPWELL detectors respectively. For both detectors, while the efficiency remains constant, the multiplicity increases when approaching the pad border. In the $300 \times 300$ mm$^2$ detector, the multiplicity increase is sharper in the x direction. This is attributed to the hexagonal geometry of the THGEM holes pattern (compared to the square pattern of the $100 \times 100$ mm$^2$ detector, see appendices A.2 and A.3), having a different pitch along the x and y directions, and the PEs focusing into the THGEM holes. Laboratory and simulation studies aiming at to decoupling the different physics processes governing the pad multiplicity (charge spread, electronics crosstalk, etc) are subject for future studies and are beyond the scope of this work.

(a) (b)

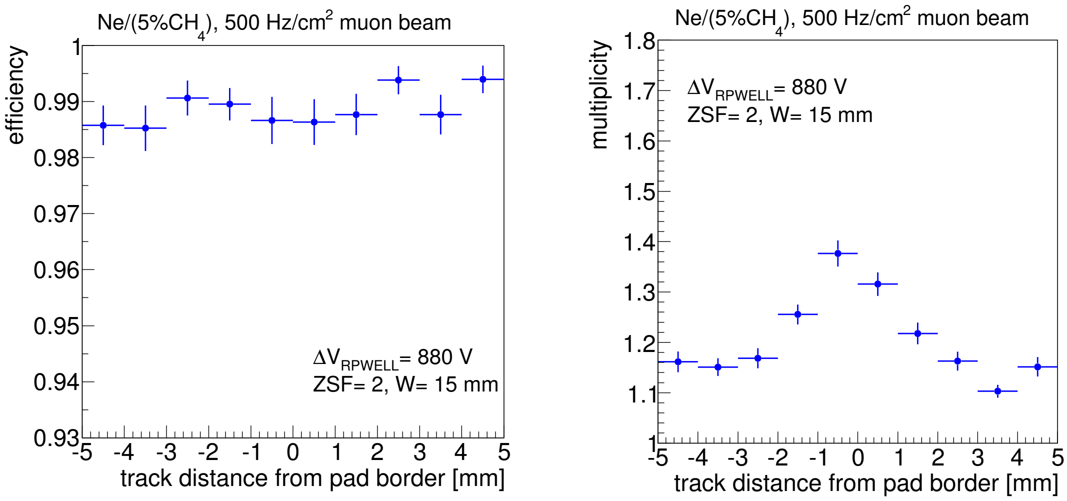


Figure 9: The detection efficiency (a) and the average pad multiplicity (b) as a function of the distance from the pad boundaries along one axis on the detector plane measured by the $100 \times 100$ mm$^2$ RPWELL detector, in Ne/(5%)$CH_4$ gas mixture. The detector was operated at the nominal conditions under a $\sim$500 Hz/cm$^2$ muon beam. Data recorded by APV25/SRS readout electronics.

(a) (b)

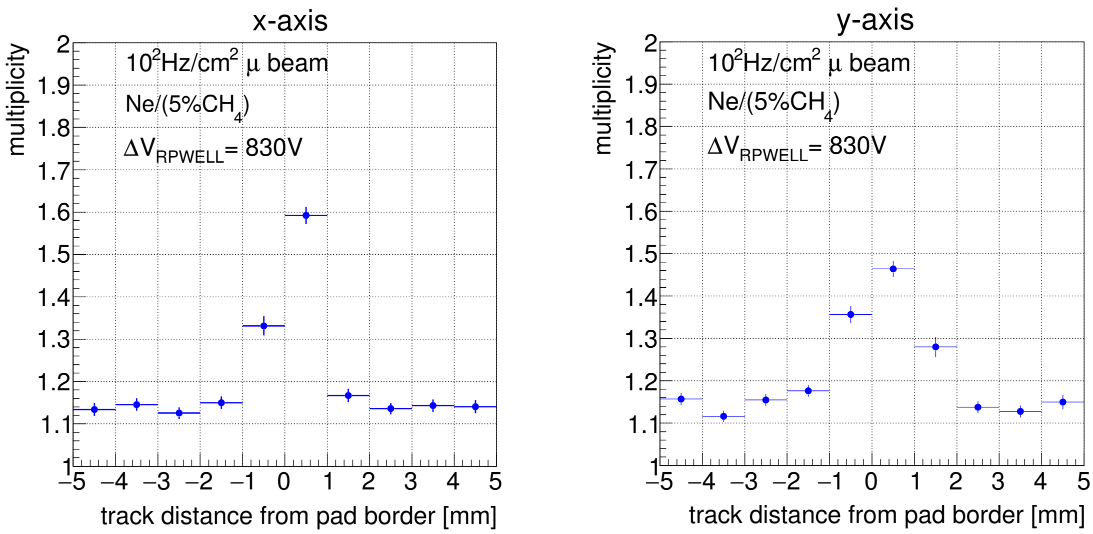


Figure 10: Using the same data set; the local average pad multiplicity as a function of the track distance from the pad boundary along the detector's x-axis (a) and y-axis (b) measured by the 300 × 300 mm$^2$ RPWELL detector, in Ne/(5%)$CH_4$ gas mixture, under a ∼10$^2$ Hz/cm$^2$ muon beam. Similar results were obtained with the argon gas mixtures. Data recorded by APV25/SRS readout electronics.

**Rate dependence and stability**

Figures 11 and 12 show the results of measurements with increasing pion fluxes for the 100 × 100 mm$^2$ and for the 300 × 300 mm$^2$ RPWELL detectors respectively. In both cases, the $\Delta V_{\mathrm{RPWELL}}$ value was fixed to the one at the beginning of the efficiency plateau, as measured in a dedicated run with low rate muons. Consistently for all three gas mixtures, the global detection efficiency remained unaffected until rates of ∼10$^4$ Hz/cm$^2$. An efficiency drop of a few % was observed while approaching rates of ∼10$^5$ Hz/cm$^2$, due to some tens % gain loss measured at these rates (figure 12-b), possibly resulting from the charging up of the holes and avalanche build-up limitations on the resistive anode [165, 166, 156].

To demonstrate the electrical stability of the RPWELL, we measured the current flowing through the anode using a sensitive ammeter [161], while irradiating the detector with pions at different rates. figures 11-b and 13 show the current and the pion rates as a function of time for the $100 \times 100$ mm$^2$ and for the $300 \times 300$ mm$^2$ RPWELL detectors respectively. Similar results were obtained in all three gas mixtures. As expected, the small current spikes, correlated with the beam spill-structure, increases smoothly in amplitude with the particle rate.

(a) (b)

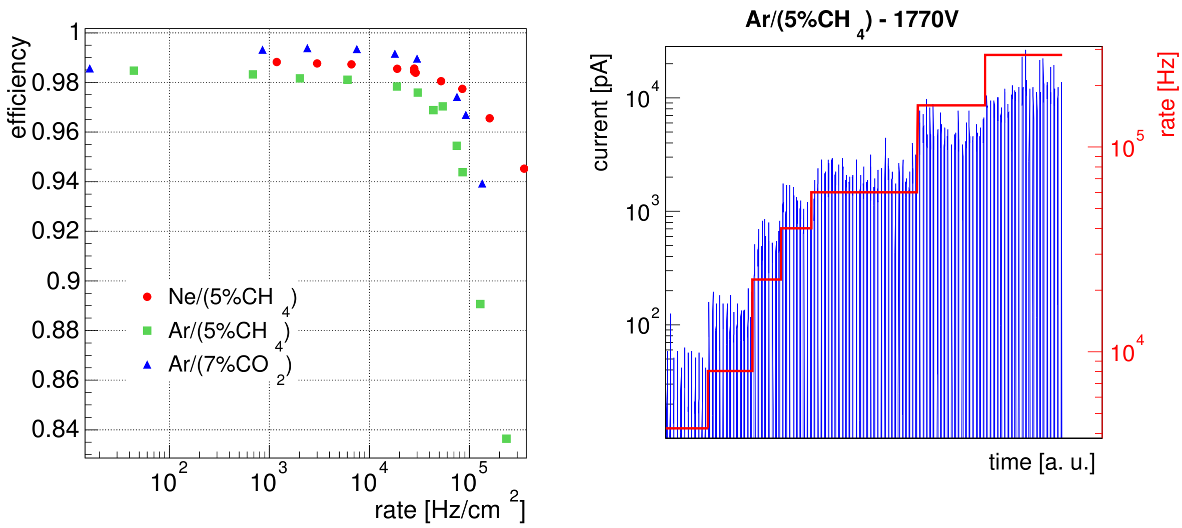


Figure 11: Global detection efficiency of the $100 \times 100$ mm$^2$ RPWELL detector as a function of the incoming particle flux in Ne/(5%)$CH_4$, Ar/(5%)$CH_4$ and Ar/(7%)$CO_2$ gas mixtures. The values of $\Delta V_{\mathrm{RPWELL}}$ were 880 V, 1700 V and 1770 V respectively. b) Current flowing through the detector during pion runs at different rates in Ar/(5%)$CH_4$. The beam spill-structure is clearly visible. Data recorded by APV25/SRS readout electronics.

A stable operation of the detector was demonstrated over time, under $10^4$-$10^5$ Hz/cm$^2$

(a) (b)

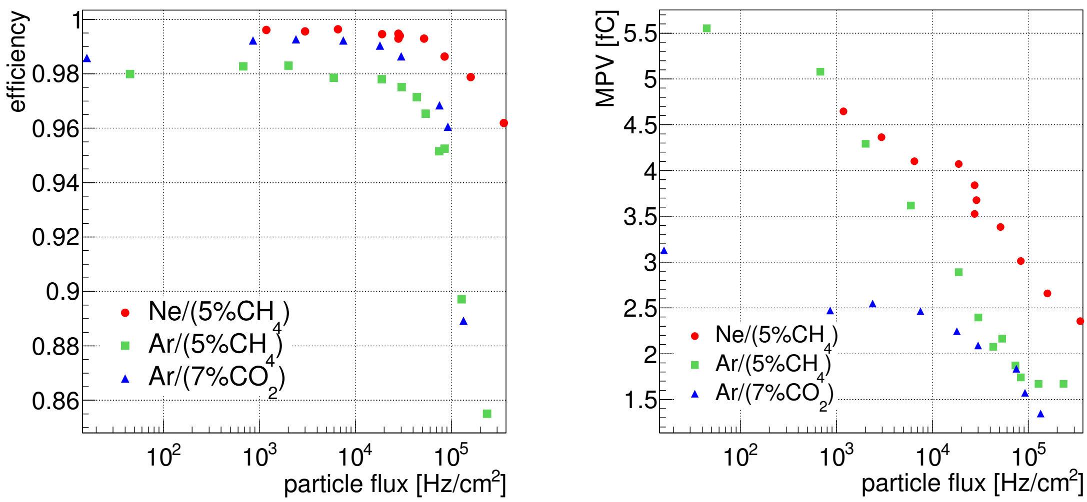


Figure 12: For the same data set; the global detection efficiency (a) and the charge MPV (b) as a function of the particle flux. Measurement performed by the $300 \times 300$ mm$^2$ RPWELL detector operated at a potential $\Delta V_{\rm RPWELL}$= 880 V, 1700 V, 1770 V in Ne/(5%)$CH_4$, Ar/(5%)$CH_4$, and Ar/(7%)$CO_2$ gas mixtures respectively. Data recorded by APV25/SRS readout electronics.

pion fluxes, as shown in figure 14 and 15 for the $100 \times 100$ mm$^2$ and for the $300 \times 300$ mm$^2$ RPWELL detectors respectively. The applied voltages were the same as those of the measurements presented in figure 11 and 12. No significant gain variations were observed along $\sim$1 hour of operation in all three gas mixtures for both detectors. The values of global detection efficiency and average pad multiplicity during these measurements also remained unaffected.

The discharge probability was measured during the high-rate pion runs presented in figure 14 and 15. No discharges were observed in the $100 \times 100$ mm$^2$ detector in any of the gas mixtures while irradiating the detector with over $10^8$ pions; therefore the resulting value of $10^{-8}$ is a lower limit for the discharge probability in the present

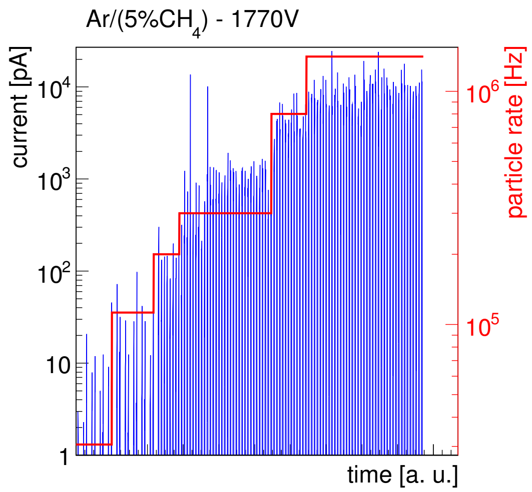


Figure 13: Current flowing through the $300 \times 300$ mm$^2$ RPWELL detector detector anode during pion runs at different rates in Ar/(5%)$CH_4$ gas mixture. The beam spill structure is clearly visible.

RPWELL configuration. Since pions are prone to induce highly-ionizing secondary events, this is an additional indication on the broad dynamic range of this detector. The $300 \times 300$ mm$^2$ RPWELL showed some sporadic discharges when operated in argon mixtures, as shown for example in figure 15-b, during the measurement in Ar/(5%)$CH_4$. Since discharges were recorded also in the electrode segments located outside the beam area, they are most likely related to "weak points" in the modular detector prototype design: an open path along the support pins, leading to discharges propagating between the THGEM segment edge and the anode (see appendix A.3). This conclusion is supported by the suppression of those discharge events when rubber o-rings were inserted around each pin in between the THGEM and the spacers. Such open paths were avoided in the next iteration of the detector design (used for the assembly of the $500 \times 500$ mm$^2$ detector).

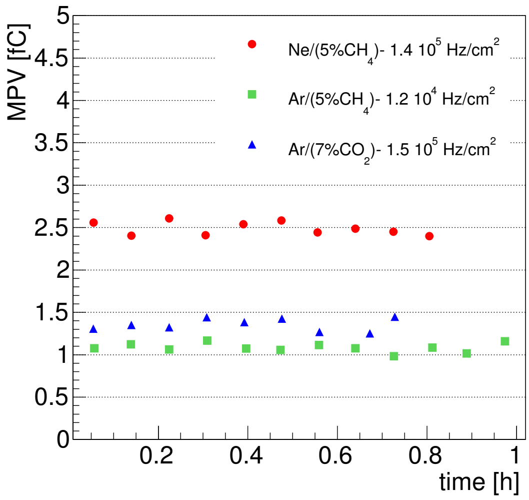


Figure 14: Gain stability of the $100 \times 100$ mm$^2$ RPWELL detector over time under a high-rate ($10^4$-$10^5$ Hz/cm$^2$) pion flux in Ne/(5%)$CH_4$, Ar/(5%)$CH_4$ and Ar/(7%)$CO_2$ gas mixtures. The operation voltage $\Delta V_{RPWELL}$ values were 880 V, 1700 V and 1770 V respectively. Data recorded by APV25/SRS readout electronics.

(a)

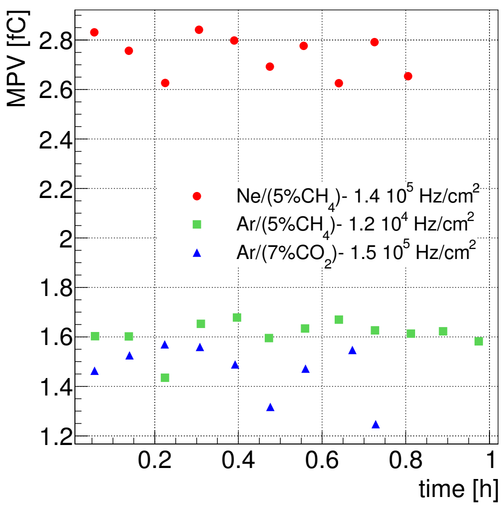


(b)

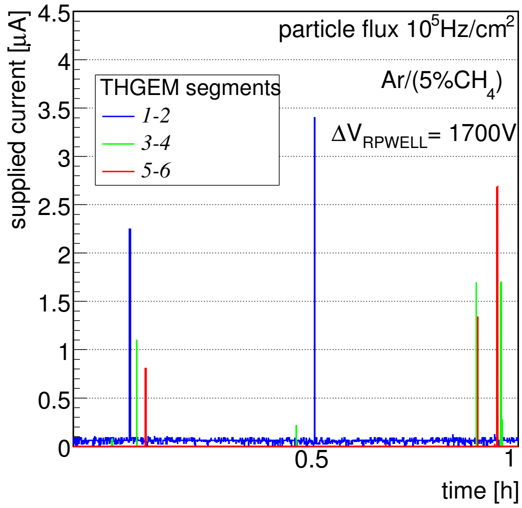


Figure 15: For the same data set; (a) Gain stability (charge MPV) as a function of time at moderate pion fluxes. Measurement performed by the $300 \times 300$ mm$^2$ RP-WELL detector operated at a potential $\Delta V_{RPWELL}$= 880 V, 1700 V, 1770 V in Ne/(5%)$CH_4$, Ar/(5%)$CH_4$, and Ar/(7%)$CO_2$ gas mixtures respectively. (b) Current supplied to the three couples of THGEM segments 1-2, 3-4, 5-6 (shown in figure35-a), during 1 hour operation at $\sim 10^5$ Hz/cm$^2$ particle flux in Ar/(5%)$CH_4$. The beam was focused on the center of segment 3.

### 3.1.2 Epoxy/graphite based coupling

As described in section 2.1.1, coupling the anode to the RP through an epoxy/graphite layer has potentially several advantages. The $100 \times 100$ mm$^2$ tiled Semitron-RPWELL prototype with pads readout (section A.4.2) was built to study the effect of the epoxy/graphite layer on the detector performance, especially on the pad multiplicity.

#### Efficiency, pad multiplicity and rate dependence

The $100 \times 100$ mm$^2$ tiled Semitron-RPWELL (section A.4.2) performance in terms of efficiency and pad multiplicity is shown in figure 16. This performance is compared to that of the prototypes assembled using the channel-by-channel technique (figure 9). The detectors were operated in the same Ar/(7%)$CO_2$ gas mixture. As can be seen, using epoxy/graphite coupling similar performance was recorded. In particular, no significant increase in the average pad multiplicity was observed; it remained at $\sim$1.2 at 98% efficiency.

Based on these results, it can be concluded that the presence of a resistive epoxy/graphite layer between the anode and the RP does not increase significantly the lateral spread of the avalanche electrons. Further studies (see appendix B) have shown that, despite the fact that the epoxy is a good insulator, there is a finite resistivity between the RP and the anode through the epoxy. Thus, the least resistance path to ground for the avalanche electrons is through the RP, and the charges do not spread sideways.

The response of the detector to increasing pion fluxes is shown in figure 17; the performance is very similar to the one observed with the prototype assembled with a channel-by-channel coupling technique (figure 11). This indicates no degradation due to the different anode-RP coupling methods.

Based on these results, this simple RP coupling technique through a graphite/epoxy layer was adopted for the assembly of the $500 \times 500$ mm$^2$ RPWELL prototype.

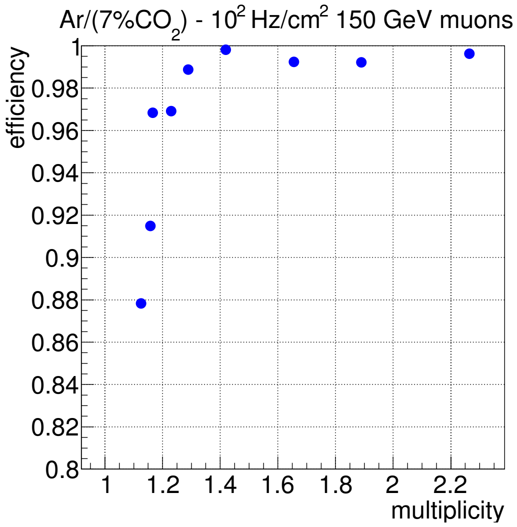


Figure 16: The measured efficiency as a function of the multiplicity in the tiled Semitron-RPWELL detector, in Ar/(7%)$CO_2$ gas mixture. The RP-anode coupling through a graphite/epoxy layer does not affect the pad multiplicity. Data recorded by APV25/SRS readout electronics.

(a)

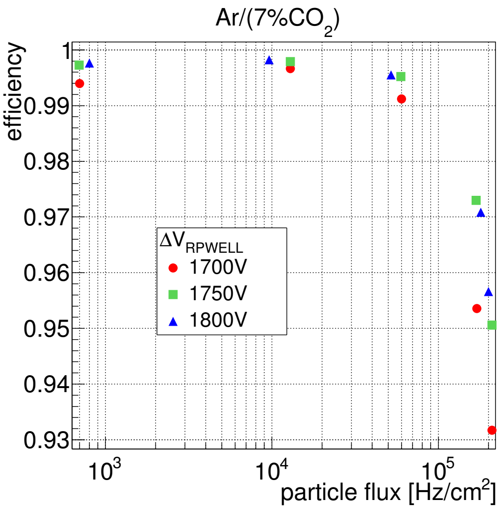


(b)

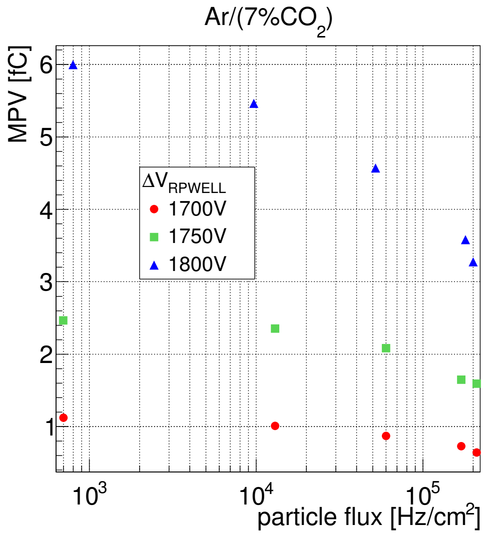


Figure 17: The measured global detection efficiency (a) and the charge distribution MPV (b) as a function of the particle flux in the tiled Semitron-RPWELL detector, in Ar/(7%)$CO_2$ gas mixture. Data recorded by APV25/SRS readout electronics.

## 3.2 Position resolution of RPWELL detectors

### 3.2.1 Position resolution: measured data

The $100 \times 100$ mm$^2$ tiled silicate-glass-RPWELL detector (section A.4.1) with strips readout was operated in Ne/(5%)$CH_4$ gas mixture and characterized in the test-beam. It was exposed to a flux of 150 GeV muons at $\sim 10^2$ Hz/cm$^2$, and its localization properties were studied taking advantage of the tracking system (setup and methods are described in section 2.3) [4]. A typical cluster charge spectrum is showed in figure 18. The fit to a Landau distribution show a good separation from the noise.

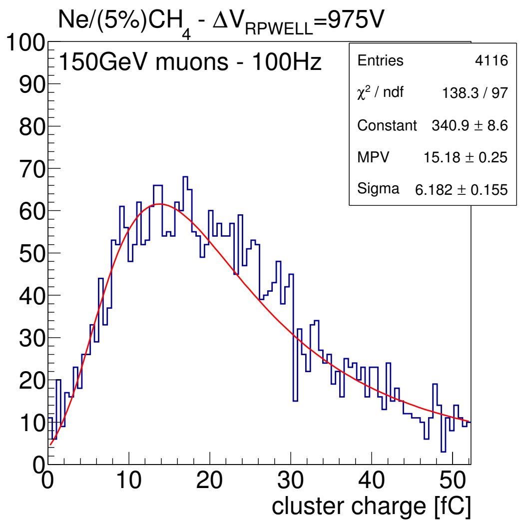


Figure 18: Cluster charge spectrum from muon beam, recorded with the $100 \times 100$ mm$^2$ glass-RPWELL. The fit is to a Landau distribution. Detector operated Ne/(5%)$CH_4$ gas mixture at $\Delta V_{\mathrm{RPWELL}} = 975$ V. Data recorded by APV25/SRS readout electronics.

The main conclusion from this study is that the holes pattern and pitch are the leading factors limiting the position resolution. In figure 19, an example of the residuals histogram with its Gaussian fit (residuals are defined in section 2.3 as the distance between the particle track and the charge centroid reconstructed by from the detector) is shown. The corresponding position resolution (RMS-value of the distribution) is 0.28 mm. This result was obtained at the highest achievable operation voltage of $\Delta V_{RPWELL}$= 975 V.

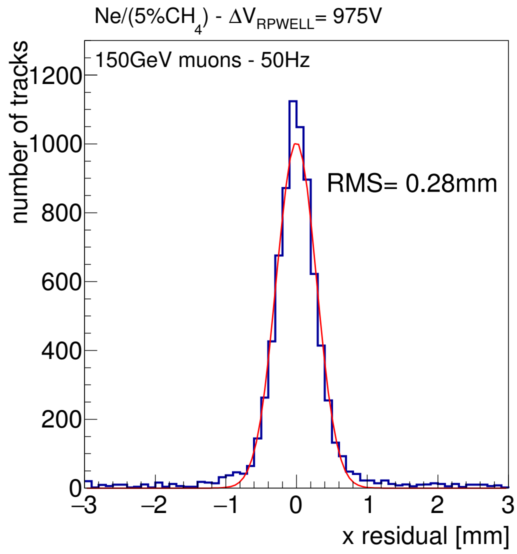


Figure 19: The residuals histogram recorded with the $100 \times 100$ mm$^2$ glass-RPWELL operated in Ne/(5%)$CH_4$ gas mixture, fitted to a Gaussian, of which the RMS defines the detector position resolution (here 0.28 mm RMS). The operation voltage was $\Delta V_{RPWELL}$= 975 V. The anode-strips pitch was 1 mm. The particle beam was 50 Hz 150 GeV/c muons at normal incidence. Data recorded by APV25/SRS readout electronics.

Figure 20-a depicts the measured position resolution as a function of $\Delta V_{RPWELL}$. As can be seen, the position resolution improves when increasing the operation voltage. Because of the low density of multiplier holes (here the hole pitch is 0.96 mm, and the hole diameter is 0.5 mm), most of the PEs ionized by muons traversing the detector orthogonally is focused in a single hole. Only a small number of PEs, if any,

reaches the neighboring holes. Every PE originates an avalanche. On average, the avalanche that develops in a neighboring hole starts from small number of PEs and thus has little charge. At higher gains (voltages), the signal-to-noise ratio improves also for avalanches starting from smaller number of PEs. This results in a better sensitivity also to avalanches developing in the neighboring holes, and an improved position resolution.

The relationship between the position resolution and the hole multiplicity is explained in more detail in section 3.2.2, when discussing the Monte Carlo simulation results.

The effect of the drift field on the position resolution was found to be negligible, as shown in figure 20-b; this suggests that the transverse electron diffusion in the 5 mm drift gap in Ne/(5%)$CH_4$ does not contribute significantly to the detector performance.

Figure 21-top shows the reconstructed beam particles position along the x-axis as measured by the tracker for the same data set as in figure 19. The equivalent measurement by the RPWELL detector is depicted in figure 21-middle. The measured RPWELL detector distribution clearly reproduces the THGEM-holes pattern shown in figure 36. This effect results from the primary charges focusing mostly into individual THGEM holes, suggesting that the THGEM-electrode geometry plays a significant role in determining the detector's position resolution. For the same measurement, figure 21-bottom shows a 2-D representation of the measured residuals as a function of the track position.

A measurement of the position resolution at different particle-incidence angles is shown in figure 22. The typical local residuals pattern shown in figure 21-c vanishes at large angles (figure 22-a), since the fraction of primary charges reaching each hole is no longer correlated uniquely with the muon trajectory. This effect results also in a degradation of the position resolution, as reflected in the residuals histograms

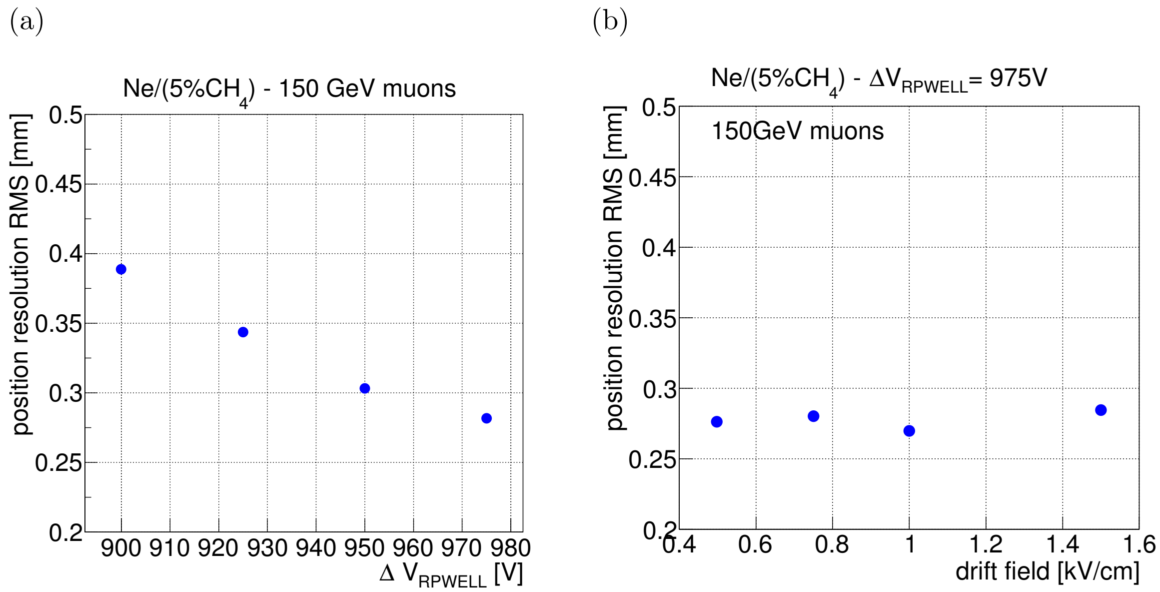


Figure 20: Data recorded by the $100 \times 100$ mm$^2$ glass-RPWELL detector operated in Ne/(5%)$CH_4$ gas mixture. a) The measured RMS position resolution as a function of $\Delta V_{RPWELL}$. b) The position resolution at the maximum achievable voltage ($\Delta V_{RPWELL}$= 975 V) for different values of the drift field. The readout anode-strips pitch was 1 mm. The beam was 50 Hz 150 GeV/c muons at normal incidence. Data recorded by APV25/SRS readout electronics.

plotted in figure 22-b. In figure 22-c we show the position resolution as a function of the incidence angle. At 40° the position resolution is 0.82 mm RMS about a 3-fold degradation compared to the perpendicular incidence case.

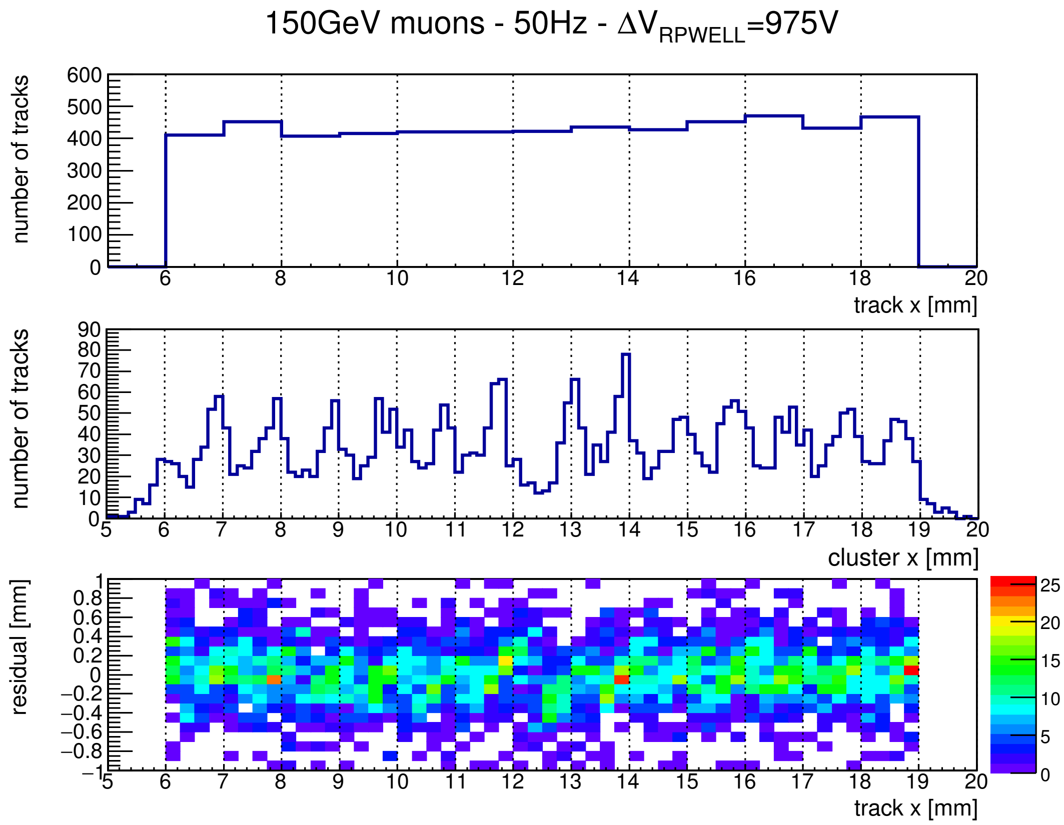


Figure 21: Data recorded by the $100 \times 100$ mm$^2$ glass-RPWELL detector in Ne/(5%)$CH_4$ gas mixture, operated at $\Delta V_{RPWELL}$= 975 V. The particle beam was 50 Hz 150 GeV/c muons at normal incidence. For the same run; (Top) The reconstructed muon-beam distribution along the x-axis measured by the tracker. (Middle) The reconstructed beam distribution recorded by the $100 \times 100$ mm$^2$ glass-RPWELL detector. (Bottom) Local residuals pattern. The peaks in RPWELL detector distribution correspond to the holes locations. The strips pitch was 1 mm. Data recorded by APV25/SRS readout electronics.

(a) (b) (c)

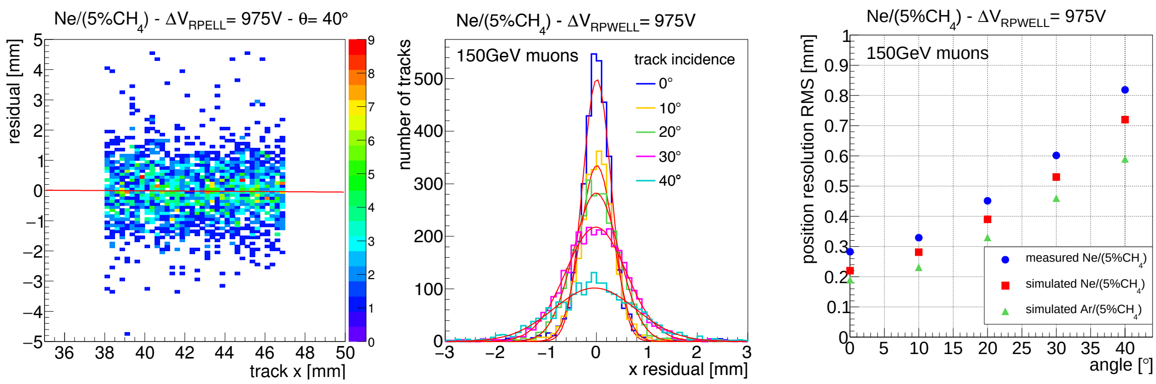


Figure 22: Data recorded by the $100 \times 100$ mm$^2$ glass-RPWELL detector in Ne/(5%)$CH_4$ gas mixture, operated at $\Delta V_{RPWELL}$= 975 V: a) The measured local residual value vs particle location at a muons incidence angle of $\theta$= 40°, after linear correction. Distributions of the residuals (b) and RMS position resolution (c) for different particle-incidence angles. The strips pitch was 1 mm. Data recorded by APV25/SRS readout electronics.

### 3.2.2 Position resolution: Monte Carlo simulations

To study the physics processes governing the RPWELL position resolution measured in the test-beam, detailed Monte Carlo simulations were performed. The simulation is described in section 2.4. More details can be found in [4]. Figure 23-a shows the simulated residuals histogram for the $100 \times 100$ mm$^2$ glass-RPWELL detector's operation in Ne/(5%)$CH_4$ gas mixture, yielding the best experimental position resolution, with $\Delta V_{\mathrm{RPWELL}}$= 975 V.

The simulated RMS value of 0.22 mm is slightly better than the experimental one (0.28 mm) shown in figure 19. This discrepancy is partly due to the measured electronic noise of 10 ADC counts RMS (average on all the channels). Once the noise is included on the simulation as a "white" Gaussian fluctuation of the strips baseline, a value of 0.24 mm RMS is obtained, closer to the measured one.

Figure 23-b (top) shows the simulated cluster position along the x-axis. The profile is in good agreement with the experimental distribution shown in figure 21-b (top), with peaks corresponding to the THGEM holes. This structure is attributed to the combined effect of charge focusing into the holes and charge sharing between holes being very close to one. In figure 23-b (bottom), a 2-D representation of the simulated residuals as a function of the event position is shown. Also here, the characteristic pattern due to primary-charge focusing into the holes is clearly visible.

Comparing the simulated local residuals in figure 23-b (bottom) with the measured ones in figure 21-b (bottom), the patterns are very similar, with the residuals reaching zero values in correspondence to THGEM holes and the central region between holes; the latter being due to charge sharing. The simulation confirms the measured degradation of the position resolution at increasing angles (figure 22-c).

In addition to the simulation of the RPWELL detector with Ne/(5%)$CH_4$ gas mixture, the properties of RPWELL operated with argon mixtures were studied. .

(a)

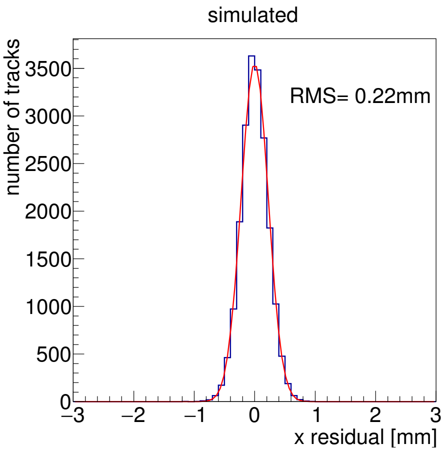


(b)

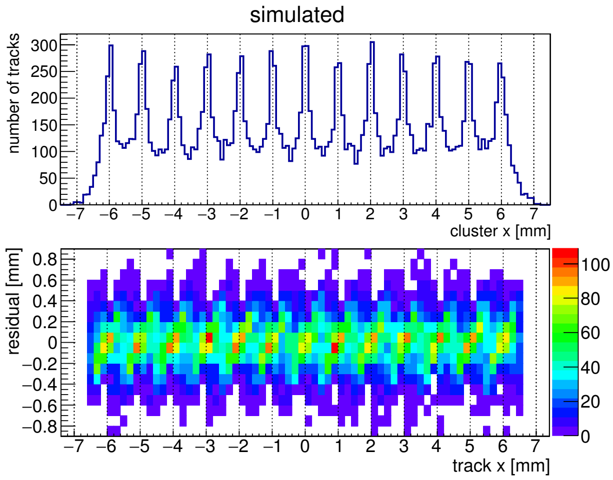


Figure 23: Simulated RPWELL performance in Ne/(5%)$CH_4$ gas, operated at $\Delta V_{\mathrm{RPWELL}}$= 975 V. a) Residuals histogram, with the resulting 0.22 mm RMS position resolution value. b) Simulated detector response, along the x-axis, to a broad beam (top), and local residuals pattern (bottom).

The simulated position resolution of an of RPWELL operated with Ar/(5%)$CH_4$ as a function of incidence particle angle is shown in figure 22-c. It is compared to the measured and simulated position resolution of RPWELL operated with Ne/(5%)$CH_4$, for the same 5 mm drift gap. The noticeable improvement (10% and 22% for incidence angles of 0° and 40° respectively) is due to the larger number of PEs extracted by a MIP in argon compared to neon, as shown in the simulated distributions in figure 24-a; the larger density of PEs clusters along the muon trajectory, improves the correlation between the track trajectory and the holes participating in the charge multiplication.

The electron transport properties (diffusion) in the different gas mixtures affect the detector response. This could have different implications depending on the target application. In particular, a detector optimized for position resolution could benefit from larger diffusion while smaller diffusion is needed to minimize the average pad multiplicity.

**Implications for a (s)DHCAL**

It was shown (section 3.2.1) that the main factor limiting the position resolution in the RPWELL detector is the THGEM holes pattern. In particular, the worst performance is obtained when the holes multiplicity is exactly 1 (no primary charge sharing among neighboring holes). Comparing the Ar/(7%)$CO_2$ and Ar/(5%)$CH_4$ gas mixtures, while the number of extracted PEs in both gas mixtures is similar (figure 24-b), the transverse electron diffusion coefficients are different: 100 µm/cm for Ar/(7%)$CO_2$ and 620 µm/cm for Ar/(5%)$CH_4$ at 0.5 kV/cm drift field [167]). Moreover, compared to neon-based gas mixtures, in argon mixtures the operation voltage is relatively high, resulting in an enhanced focusing of the electrons into the THGEM holes. These two effects combined together result in a lower PEs charge sharing between neighboring holes for Ar/(7%)$CO_2$.

As an example, the resulting average holes multiplicity in a 1 mm holes pitch RPWELL with 3 mm drift gap, operated at $\Delta V_{RPWELL}$= 1900 V, for a 150 GeV muon traversing the detector in the middle of a THGEM hole is 1.01 and 1.55 for Ar/(7%)$CO_2$ and Ar/(5%)$CH_4$ respectively. Monte Carlo simulations shows that the fact that in Ar/(7%)$CO_2$ the average hole multiplicity is very close to 1, results in a slightly worse position resolution of 0.24 mm, compared to 0.22 mm in Ar/(5%)$CH_4$. From these considerations, the Ar/(7%)$CO_2$ mixture would be optimal for an application like (s)DHCAL: in case that the THGEM holes pattern would match the segmentation of the readout (e.g. pads), a hole multiplicity close to 1 would give a minimal pad multiplicity, which is the important feature for that application.

(a) (b)

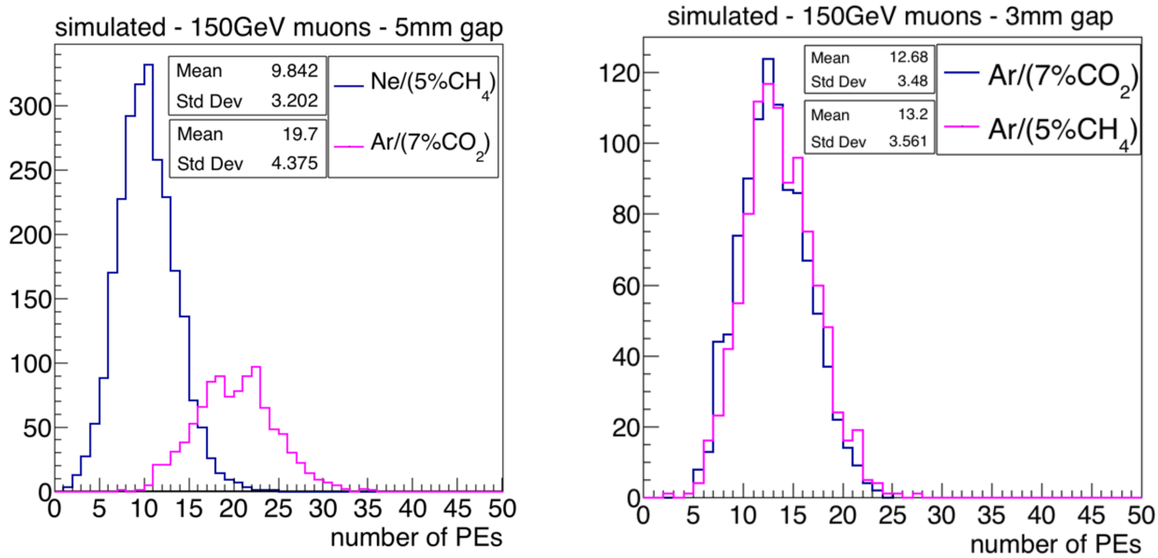


Figure 24: Simulated primary electrons distributions extracted by 150 GeV muons in 5 mm Ne/(5%)$CH_4$ or Ar/(5%)$CH_4$ (a) and in 3 mm Ar/(5%)$CH_4$ or Ar/(7%)$CO_2$ gas mixtures (b).

## 3.3 Large-area RPWELL prototype

The target detector area is $500 \times 500$ mm$^2$. The design and assembly of such prototype presents many technological challenges. Among others:

- Building a detector with uniform response over the whole detection area.
- Maintain discharge-free operation. In particular, ensuring the protection of the anode at the interfaces between two RP tiles.
- Minimizing the dead area and the effect of the edges.

Focusing on overcoming these technological challenges, the large $500 \times 500$ mm$^2$ prototype was assembled with a strips readout anode (significantly cheaper than a padded one).

In this section, we present the main results obtained with this prototype: response uniformity in normal operation conditions, stability under harsh irradiation conditions, detection efficiency in Ar/(7%)$CO_2$ gas mixture. These positive results were obtained with a thin RPWELL configuration with 3 mm drift gap. It is considered an important achievement, given the demanding thickness requirements for DHCAL or sDHCAL sampling elements.

### 3.3.1 Laboratory studies

As a first step, preliminary to a test-beam campaign (section 3.3.2), the $500 \times 500$ mm$^2$ detector prototype described in section A.5 was tested in the laboratory to ensure efficient detecion of MIPs, and stable operation under harsh radiation environment.

#### Cosmic-rays measurements

Cosmic rays spectra were recorded with the $500 \times 500$ mm$^2$ RPWELL detector. The setup described in section2.2.2, based on the APV25/SRS electronics system was used. The operation voltage was set to $\Delta V_{RPWELL}$= 1900 V. This value is higher than the one typically needed to achieve maximum efficiency with RPWELL detectors of similar geometry with the same readout electronics. It was dictated by the fact that the induced signal did spread over several strips, and thus the charge per strip was relatively low (good signal-to-noise separation over several strips is needed for precise measurement of the cluster centroid position).

The spectrum from a $100 \times 100$ mm$^2$ detector region (selected by scintillators position) is shown in figure 25. Similar spectra were recorded from all the 4 irradiated glass-tiles regions (see the detector geometry in appendix A.5). To avoid noise events, we considered only clusters with strip multiplicity >5. Considering that on average 13 electron-ion pairs are produced by a MIP in the 3 mm drift gap in Ar/(7%)$CO_2$ (see figure 24), and that all of them are collected within ~100 ns, we estimate from the MPV of the Landau spectrum an effective gain of 12 fC/13e = $1.5{\cdot}10^3$ with the present ~75 ns shaping time of the readout electronics. The total gas gain is significantly higher, due to the 2 μs long signal rise time [17] that the fast readout electronics cannot fully integrate. The effective gain was indeed similar to the one reached in the test-beam (figure 29), and it is compatible with the gain curve trend shown in with a 100 × 100 $mm^2$ detector in Ar/(7%)$CO_2$ with pad readout [2] (figures 7 and 8).

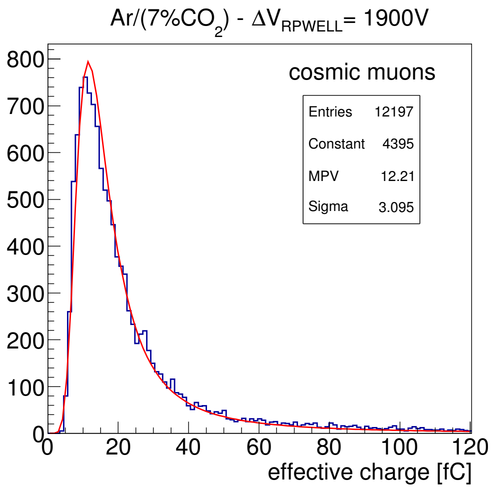


Figure 25: Cosmic rays spectrum measured from a 100 × 100 $mm^2$ region of the 500 × 500 $mm^2$ detector operated in Ar/(7%)$CO_2$ gas mixture at a voltage of $\Delta V_{\mathrm{RPWELL}}$= 1900 V. The fit to a Landau distribution shows a MPV of 12 fC. Data recorded by APV25/SRS readout electronics.

**X-ray stress-test and preliminary uniformity scan**

The 500 × 500 $mm^2$ RPWELL prototype was tested with the x-ray scanning system described in section 2.2.1. The detector was operated in Ar/(7%)$CO_2$ under a flow of 10 ccm/min. The operation voltage was $\Delta V_{\mathrm{RPWELL}}$= 1800 V, and the voltage across the 3 mm drift gap was kept at 150 V. The effective gain under irradiation could not be measured directly (as explained in section 2.2.1), but in a similar configuration, in normal operation (under low rate MIPs) it is $\sim 0.8 \cdot 10^3$ (figure 7). Although this gain is low, due to the large number of PEs, a lot of charge was occupying the holes.

Complementary and prior to the normal operation in test-beam, this measurement served as a stress-test of the detector. The operation under high intensity of high-energy photon flux demonstrated that it can operate safely under harsh irradiation condition, high rate and high charge, without suffering persistent or permanent currents after the source is turned off. Moreover, no "hot-spots", i.e. local sources of electrical instabilities were found, even close to sensitive regions like the interface in between glass RP tiles (see figure 39-a).

**Stability** No significant current increase was observed during 9 hours of constant irradiation over a $30 \times 30$ mm$^2$ area at maximum intensity in the same detector position, neither near an electrode spacer (see figure 39-b) nor far away from it. This indicates that the spacers and the epoxy that glues them to the electrodes are not a source of electrical instability. An initial current increase from $\sim 700$ nA to $\sim 980$ nA was observed in the first hour of operation; then it remained stable or slightly decreased to $\sim 940$ nA. This could be an indication to some charging up effect, probably influencing the gain response of the detector [165]. When the x-ray beam was turned off, the current immediately went back to the baseline value of $\sim 5$ nA, indicating upon the absence of permanent effects.

**Response uniformity** A scan of the full $500 \times 500$ mm$^2$ RPWELL detector area was performed using a 30 mm collimator, to estimate its response uniformity and to find out the presence of eventual hot-spots or defects. The maximum x-ray flux was used. The operation voltage was $\Delta V_{\mathrm{RPWELL}} = 1800$ V (with 150 V across the drift gap), and each position was irradiated for a period of 120 s.

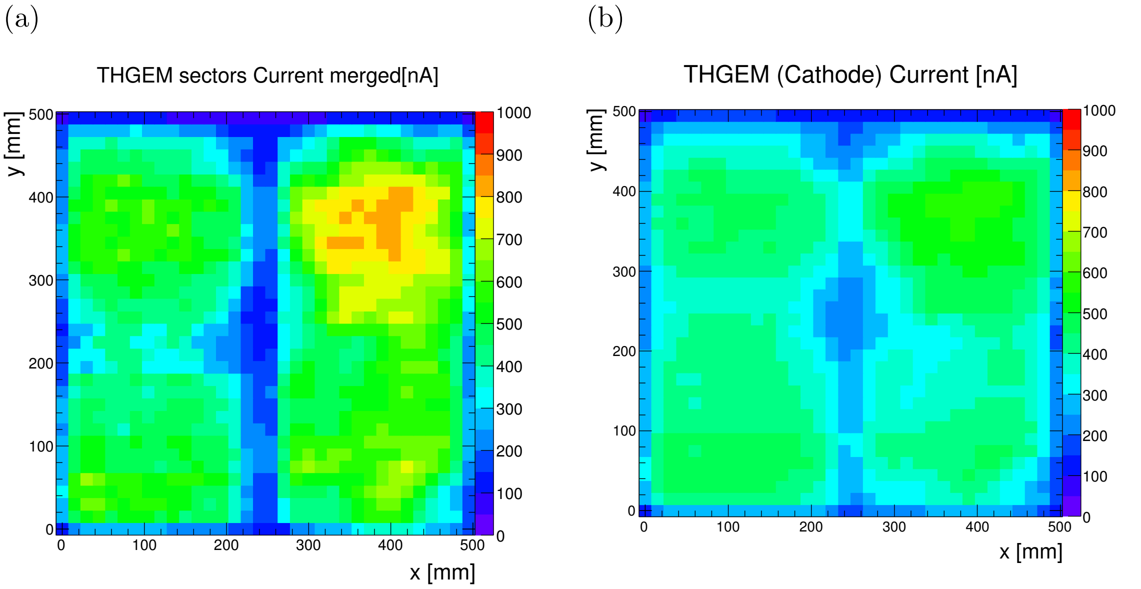


Figure 26: Average current measured when scanning the $500 \times 500$ mm$^2$ RPWELL detector with 22 keV x-rays. Detector operated in Ar/(7%)$CO_2$ gas mixture at $\Delta V_{\mathrm{RPWELL}}$= 1800 V. The scan step was 120 seconds per point, at maximum x-ray flux. Current recorded from the THGEM (a) and cathode (b) electrodes.

For each beam position, the average current measured on the two THGEM electrodes and on the cathode (the latter due to a fraction of the avalanche ions leaving the THGEM holes and drifting back to the cathode) is plotted (figure 26).

Under this harsh conditions, it can be seen that the current measured at the center of each of the 4 glass-RP tiles (figure 40-a) is higher compared to the borders. This effect could be attributed to a non-uniform pressing of the THGEM during the gluing process. The latter may result in a thicker layer of graphite/epoxy, and hence higher resistance, at the borders of each tile. The current flowing to ground through higher resistance would cause a larger voltage drop, resulting in a lower gain. This effect seems to be more severe for the right-up tile. The variance in the thickness of different glass-tiles might also affect the uniformity.

Figure 27 presents the results of a scan of the right-up glass-tile region, operated with a finer collimation of 5 mm diameter, at $\Delta V_{\mathrm{RPWELL}}$= 1800 V, for 5 seconds per point. Mechanical features, like the position of 6 machined wells in the cathode and dead areas corresponding to the 6 mm diameter spacers between the THGEM and the cathode, are nicely imaged. The local gain non-uniformities, especially the low gain in the sides, hint to the above mentioned non-uniformity of the RP gluing to the anode. This non-uniformity did not show up during regular detector operation under low-rate MIP-like radiation (see figure 29). Nevertheless, the next prototypes will be assembled paying careful attention to the selection of the glass tiles and to the pressing during gluing.

(a) (b)

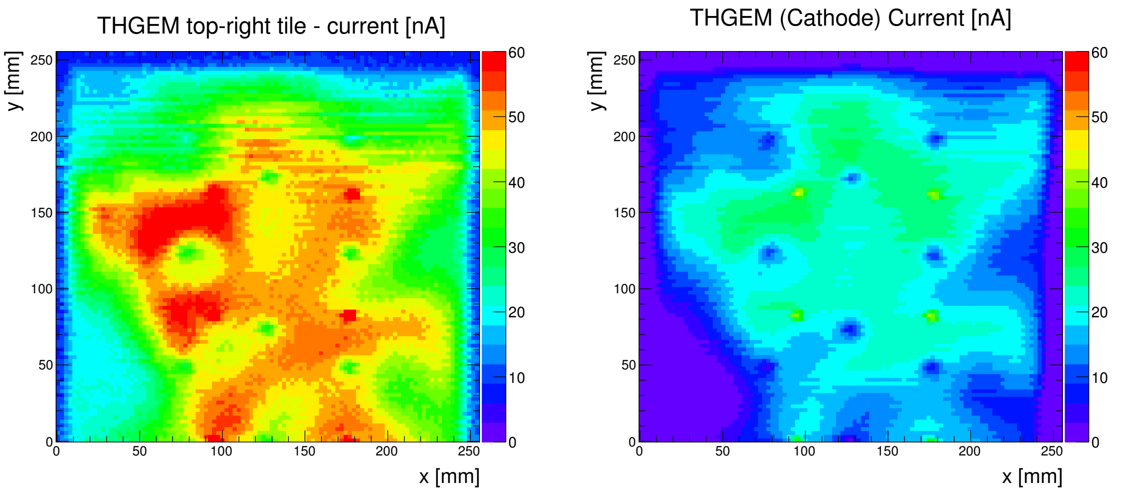


Figure 27: Average current scan of a 250× 250 mm$^2$ region (top-right quarter) of the 500 × 500 mm$^2$ RPWELL with 22 keV x-rays. Detector operated Ar/(7%)$CO_2$ gas mixture at $\Delta V_{\mathrm{RPWELL}}$= 1800 V. The scan step was 5 seconds per point, at maximum x-ray flux. Current recorded from the right (a) THGEM sector and from the cathode (b).

### 3.3.2 Test-beam studies

#### Efficiency and gain uniformity

The $500 \times 500$ mm$^2$ RPWELL detector described in section A.5 was built as a step to demonstrate the scalability of the RPWELL concept to large areas. One of the most important features of a large tracking detector is a uniform response.

Figure 28 shows the cluster spectrum recorded by the $500 \times 500$ mm$^2$ RPWELL under $10^{\,2}$ Hz muon beam. The spectrum, fitted to a Landau distribution, shows a good separation from the noise.

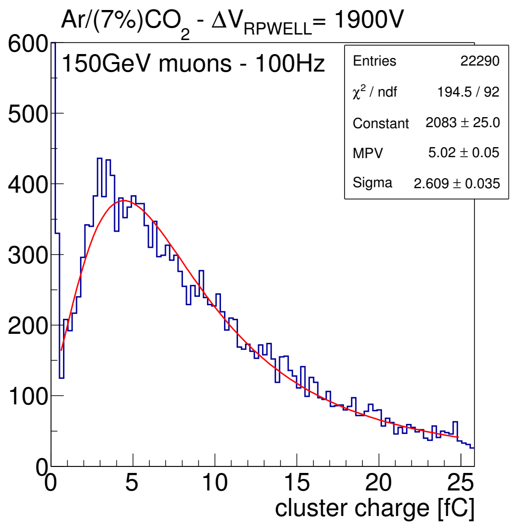


Figure 28: Cluster charge spectrum from muon beam, recorded with the $500 \times 500$ mm$^2$ RPWELL. The fit is to a Landau distribution. Detector operated Ar/(7%)$CO_2$ gas mixture at $\Delta V_{\mathrm{RPWELL}}$= 1900 V. Data recorded by APV25/SRS readout electronics.

Figure 29 depicts the local efficiency and the charge spectrum average in a wide central region of a THGEM sector, measured in low rate muon beam. It can be seen that efficiency close to 1 is uniformly obtained over the whole detector area, and that the gain non-uniformity is much milder than the one appearing in the preliminary measurements with high-intensity energetic x-rays presented in figure 26. As explained earlier, this behavior indicates upon non-uniform voltage drops observed only once the detector is exposed to intense irradiation, such that significant current is flowing through the RP which could result in a voltage drop.

(a) (b)

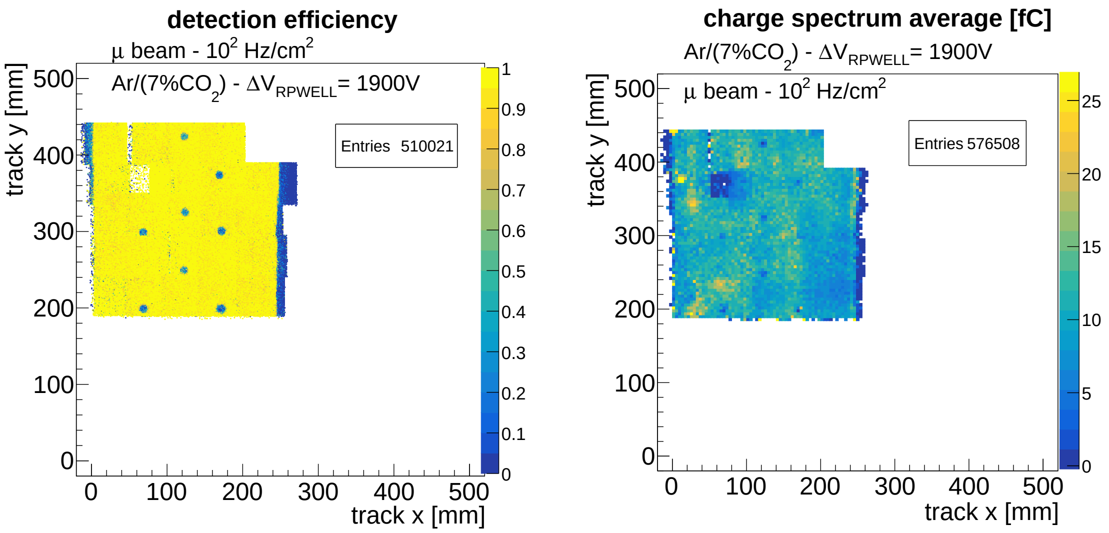


Figure 29: $500 \times 500$ mm$^2$ RPWELL local efficiency (a) and charge spectrum average (b). Detector operated Ar/(7%)$CO_2$ gas mixture at $\Delta V_{\mathrm{RPWELL}}$= 1900 V. Data recorded by APV25/SRS readout electronics.

In figure 30, it is also possible to see that the effect of a spacer (dead area) is confined to a region of typically ∼10 mm diameter around it. Considering that the diameter of the spacer itself is 6 mm, with a THGEM region around it without holes in a circle of 7.5 mm diameter, the presence of the frame is affecting the detection efficiency up to ∼2 mm distance. This result is supported by the dedicated laboratory study presented in appendix C: despite the different drift gap and radiation source, the presence of a frame (edge) inside the gas volume affected a region spanning ∼2 mm around the frame.

(a)

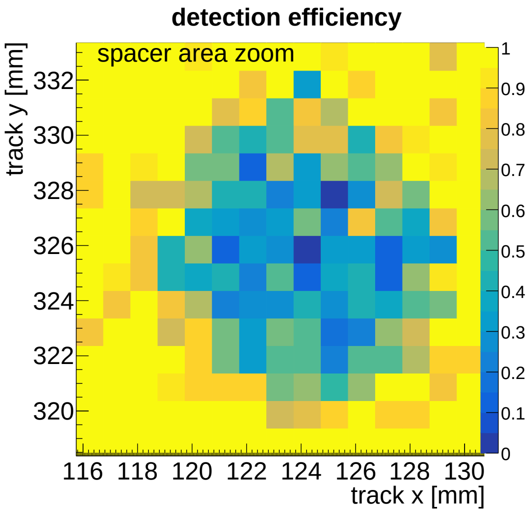


(b)

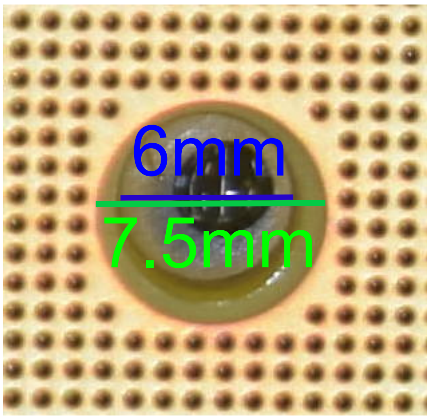


Figure 30: $500 \times 500$ mm$^2$ RPWELL local efficiency (a) around a spacer (b). Detector operated Ar/(7%)$CO_2$ gas mixture at $\Delta V_{\mathrm{RPWELL}} = 1900$ V. Data recorded by APV25/SRS readout electronics.

Based on these results, the design of the future $500 \times 500$ mm$^2$ detector prototypes is being modified; the THGEM electrode segmentation and mechanical supports structure are being optimized to minimize the dead areas and the areas affected by the presence of insulating edges in the gas volume, in particular, the central spoke (figure39-c) needs to be avoided.

**Position resolution**

A position resolution analysis (similar to the one applied to the $100 \times 100$ mm$^2$ detector described in section 3.2) was performed for the $500 \times 500$ mm$^2$ prototype. Although this prototype was not optimized for this study, it was possible to measure the position resolution taking advantage of the 1 mm pitch strips. The detector was operated in Ar/(7%)$CO_2$ gas mixture at $\Delta V_{\mathrm{RPWELL}}$= 1900 V.

In figure 31, the residuals histogram is shown, yielding a position resolution of ∼0.4 mm RMS, together with the local residuals structure resulting from the THGEM holes pattern. The resulting average strip multiplicity was ∼5.5.

Compared to the results presented in section 3.2, where the measured position resolution was 0.28 mm RMS, the worse performance is not due to some misalignment between the large THGEM electrode and the strips plane; in fact the result does not improve when considering smaller regions in the y direction.

(a) (b)

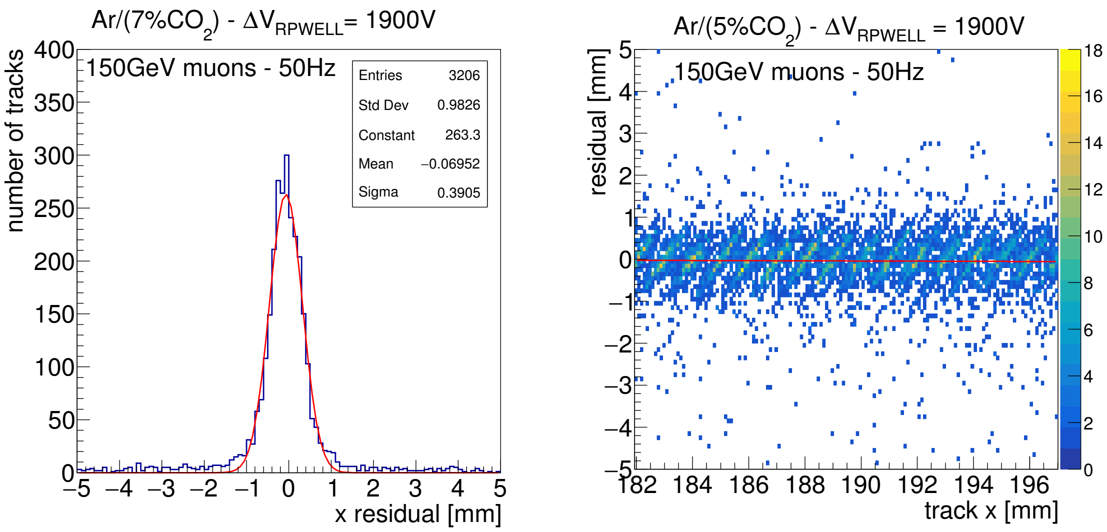


Figure 31: a) The residuals histogram recorded with the 500 × 500 mm$^2$ RPWELL prototype with strips readout, fitted to a Gaussian, of which the RMS defines the detector position resolution (here 0.4 mm RMS). b) Local residuals for the same data-set. The detector was operated in Ar/(7%)$CO_2$ gas mixture at $\Delta V_{\mathrm{RPWELL}}$= 1900 V. The anode-strips pitch was 1 mm. Data recorded by APV25/SRS readout electronics.

As shown in section 3.3 the different gas mixture and different diffusion coefficients can not explain the worse resolution obtained with the $500 \times 500$ mm$^2$ chamber. The worst position resolution value obtained by simulation for hole multiplicity 1, is $\sim$0.24 mm, to be compared with the 0.4 mm measured in the test-beam. This discrepancy is explained, instead, by the a measured electronic noise of 16 ADC counts RMS (which translates to $\sim$0.3 fC). These effects were studied with Monte Carlo simulations. For each strip, the noise was added to the signal as a random value drown from a Gaussian distribution centered at 0 width 16 ADC RMS. As can be seen in figure 32, the simulation reproduces very well the experimental residuals distribution with 0.4 mm RMS.

This result suggests that, unlike the case of the $100 \times 100$ mm$^2$ detector (section 3.2), the noise level is in this case the limiting factor determining the position resolution in the large RPWELL detector.

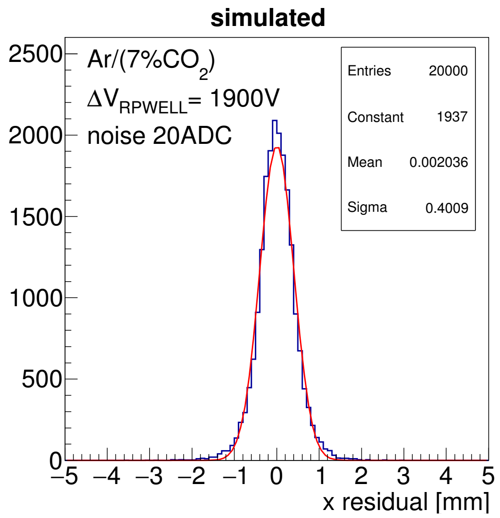


Figure 32: The simulated residuals histogram for the $500 \times 500$ mm$^2$RPWELL detector geometry, fitted to a Gaussian, of which the RMS defines the detector position resolution (here 0.4 mm RMS). The operation gas is Ar/(7%)$CO_2$, and the voltage $\Delta V_{RPWELL}$= 1900 V. The anode-strips pitch is 1 mm. The particles simulated are 150 GeV/c muons at normal incidence. Noise with 20 ADC RMS was added to reach the measured performance.

# Chapter 4

# Discussion

The present work targeted the development of an RPWELL-based detector as sampling element in a sDHCAL. The basic requirements are large area coverage, thickness less than 6 mm (excluding readout electronics), high detection efficiency at low average pad multiplicity, wide dynamic range and moderate rate capabilities. Such detector is suitable also for other applications requiring particle detection at moderate, sub-mm, spatial resolution over a large area.

All experiments designed for future linear colliders foresee the implementation of a PF calorimeter as a key-element for their expected performance. Many consider DHCAL or sDHCAL as a readout option. As an example, the baseline design of the hadronic calorimeter of the SiD experiment comprises 40 layers of stainless steel absorber plates separated by 8 mm gaps, incorporating about 4000 $m^2$ of active detection elements with $10 \times 10$ $mm^2$ pixels and highly-integrated readout electronics. The sampling elements must sustain stable operation in hadronic environment, with high detection efficiency at moderate particle fluxes (1 kHz/$cm^2$), and with minimal pad multiplicity - ideally 1 readout channel firing per particle.

As a solution, the few-mm thick RPWELL sampling element concept, developed at WIS, was suggested. The RPWELL is a single-sided THGEM electrode coupled to the readout anode through a highly Resistive Plate (RP).

Within the context of the sDHCAL, the main challenges addressed in this work were:

1. Proof of principle: demonstrating efficient and stable RPWELL operation over a broad range of primary ionization, required for the detection of minimum ionizing particles in presence of highly-ionizing background.

2. Construction and characterization of large-area detector prototypes.

3. Improving the configuration for an RPWELL sDHCAL sampling element.

When relevant and possible, studies to assess the physics processes governing the RPWELL detector performance were carried out. The achieved knowledge helps in optimizing the detector performance.

Based on previous experience [17], two materials with bulk resistivity in the range of $10^9$-$10^{10}$ $\Omega$cm were used as resistive plates: Semitron ESD225 acetal and silicate doped-glass. They presented different mechanical difficulties. For its availability in sub-mm thicknesses, the doped glass is currently the best available material. It is likely that the conception of large-area RPWELL detectors will require the development of industrially made application-tailored resistive-plate materials.

Several prototypes were built for different studies (appendix A), and systematic investigations were carried out both in the laboratory, and with muon and high-rate pion beams at the CERN-SPS beam line. Special attention has been paid to demonstrate the capability of these prototypes to fulfill the sDHCAL requirements. As mentioned earlier, the developed detectors are suitable for any application requiring sub-mm position resolution. The size of the largest prototype was $500 \times 500$ mm$^2$, demonstrating the scalability of the RPWELL concept to large areas.

The main achievements of this work are summarized below.

**RPWELL as sampling element for sDHCAL:** the present research demonstrates that the RPWELL detector, could be a suitable concept for a sDHCAL sampling element, being a single-stage, thin (less than 7 mm) detector, capable of operating reliably and stably in a discharge-free mode, also under moderate pion fluxes. In particular, Semitron ESD225 based prototypes of $100 \times 100$ mm$^2$ and $300 \times 300$ mm$^2$, with $10 \times 10$ mm$^2$ segmented anode, read out by the APV25/SRS readout electronics, showed stable operation at a gas gain of a few times $10^4$, resulting in >98% detection efficiency. Operation at particle fluxes up to $\sim 10^4$ Hz/cm$^2$ resulted in $\sim$20% gain drop leading to $\sim$5% efficiency loss. Under these conditions the recorded average pad multiplicity was $\sim$1.2 (section 3.1.1).

This performance is superior to that of the glass-RPC - the current baseline technology considered for future DHCAL applications (average multiplicity of 1.5-2 at 90-95% efficiency [149]), with the additional advantage for the RPWELL of being a fully proportional detector, suitable for a sDHCAL. The RPWELL performance is also comparable to that of other candidate technologies, like MICROMEGAS (98% efficiency at 1.1 average multiplicity [150]) and GEM ( 95% efficiency at an average multiplicity of 1.3 [151]).

Discharge-free operation of the RPWELL was demonstrated for the first time, with a single-element THGEM-based detector - also under pion flux as high as $\sim$15 kHz/cm$^2$. It is important to note that the detector response was equally good both in neon- and argon-based gas mixtures; the latter, apart from being significantly cheaper, yields a larger number of primary electrons, therefore allowing for a smaller drift gap maintaining the same detection efficiency (section 3.1.1).

**Robustness, scalability and suitability for mass production:** transition from an R&D-oriented design to an experiment-targeted prototyping approach was demonstrated. It included an assembly method by gluing under vacuum, which was tested first with the $100 \times 100$ mm$^2$ self-supported prototypes and later with the $500 \times 500$ mm$^2$ prototype.

Two different methods for coupling the RP to the readout anode were developed and investigated (section 2.1.1). A direct coupling providing a channel-by-channel conductive path gave satisfactory results, but it is complicated to implement and it cannot be applied easily to finely-segmented anodes. RP coupling through a uniform graphite/epoxy layer gave comparable performance in terms of average pad multiplicity, with the advantage of being simple to apply over large areas to any readout anode geometry (section 3.1.2).

A large-area, self-supported $500 \times 500$ mm$^2$ RPWELL detector prototype with doped silicate-glass RP coupled to readout strips through a graphite/epoxy resistive film was designed, assembled and tested at the CERN-SPS test-beam. This prototype operated stably also when scanned by an intense flux of energetic x-rays, showing no sign of local sources of electrical instabilities (section 3.3.1). When tested in muon beam, the detector demonstrated good performance in terms of efficiency and gain uniformity (section 3.3.2). This characterization constitutes an important step towards future "mass production" of large-area detectors. The present design can be further optimized according to the specific targeted application. In future prototypes, the design should be improved, so that the dead areas due to mechanical supports are minimized.

**Position resolution properties of RPWELL detectors:** the position resolution of the RPWELL detector was found to be 0.28 mm RMS, based on a dedicated study conducted with the $100 \times 100$ mm$^2$ prototype (section 3.2). This result was supported by Monte Carlo simulations which showed that the main factor limiting the resolution was the primary charge focusing into the THGEM holes (section 3.2.2)[1].

[1]In a similar study conducted with the large $500 \times 500$ mm$^2$ detector a degraded resolution of

**Edge effects:** the effect of edges and frames on the detector performance was studied in the laboratory (appendix C) and compared to the results obtained with the $500 \times 500$ mm$^2$ detector in test-beam (section 3.3.2). It was shown that the detector gain, efficiency and energy resolution, are affected by the presence of an insulating material (frame edge, supporting spoke, etc) up to 2 mm away from it.

The work presented provides new insights into some of the RPWELL operation principles and allows for optimizing the detector design and performance targeting specific applications. Based on the presented results, for the (s)DHCAL application, we propose the following sampling element configuration:

- **Mechanical design:** thin 3 mm drift gap. Number of support buttons as small as possible and no spokes, to minimize the dead area and the regions affected by the presence of edges inside the gas volume.
- **RP choice and method of coupling to the readout anode:** the RP should be Semitron ESD225 or doped silicate-glass, coupled to the anode through a graphite/epoxy layer. It is likely that the conception of large-area RPWELL detectors will require the development of industrially-made application-tailored RP materials.
- **Electrode geometry:** in order to minimize the pad multiplicity, the primary charge focusing into the THGEM holes can be optimized. If the multiplication avalanche involves only one multiplier hole, the induced signal is located exactly at its center. The single-sided THGEM electrode should therefore have a square pattern of holes, segmented into square regions aligned with

0.4 mm RMS was measured. The main limiting factor was found to be an additional electronic noise, which was at the level of ~10% of the charge (section 3.3.2). This detector was not optimized for position resolution.

the $10 \times 10$ mm$^2$ readout pads. At the border between two readout pads, the THGEM holes should be distanced by a larger pitch. The current investigated pitch was 0.96 mm within each square region, and 1.3 mm at the interface, but this value could be further optimized to get the lowest possible pad multiplicity without losing detection efficiency.

- **Operation gas:** the gas mixture should be the cost-effective Ar/(7%)$CO_2$for two main reasons: a) Due to the large number of primary electrons extracted by MIPs, full detection efficiency can be obtained with thin (3 mm) drift gap. b) It is characterized by low electron transverse diffusion, which yields small charge sharing between neighboring THGEM holes and thus small average pad multiplicity.

Future studies should focus on the role that the detector parameters (THGEM thickness, RP thickness and resistivity, etc) play in the signal formation and in the pad multiplicity. The detector operation stability over long time periods and transient behaviors due to charging up effects also deserve attention. These properties have been recently investigated by other members of our group [166, 156].

The future RPWELL-based sDHCAL prototypes will be read out by the dedicated MICROROC readout electronics [5] developed for sDHCALs applications. This is the next step towards the integration of RPWELL sampling elements into a full sDHCAL prototype.

# Bibliography


[1] S. Bressler, L. Moleri, M. Pitt, S. Kudella, C. Azevedo, F. Amaro, M. Jorge, J. dos Santos, J. Veloso, H. N. da Luz, *et al.*, "First in-beam studies of a Resistive-Plate WELL gaseous multiplier," *Journal of Instrumentation*, vol. 11, no. 01, p. P01005, 2016.

[2] L. Moleri, F. Amaro, L. Arazi, C. Azevedo, A. Breskin, A. Coimbra, E. Oliveri, F. Pereira, D. S. Renous, J. Schaarschmidt, , J. M. F. dos Santos, J. F. C. de Albuquerque Veloso, and S. Bressler, "In-beam evaluation of a medium-size Resistive-Plate WELL gaseous particle detector," *Journal of Instrumentation*, vol. 11, no. 09, p. P09013, 2016.

[3] L. Moleri, F. D. Amaro, L. Arazi, C. D. R. Azevedo, E. Oliveri, M. Pitt, J. Schaarschmidt, D. Shaked-Renous, J. M. F. dos Santos, J. F. C. de Albuquerque Veloso, A. Breskin, and S. Bressler, "The Resistive-Plate WELL with Argon mixtures-a robust gaseous radiation detector," *Nuclear Instruments and Methods in Physics Research Section A: Accelerators, Spectrometers, Detectors and Associated Equipment*, 2016.

[4] L. Moleri, P. Bhattacharya, A. E. Coimbra, A. Breskin, and S. Bressler, "On the localization properties of an RPWELL gas-avalanche detector," *Journal of Instrumentation*, vol. 12, no. 10, p. P10017, 2017.

[5] C. Adloff, J. Blaha, M. Chefdeville, A. Dalmaz, C. Drancourt, F. Dulucq, A. Espargiliere, R. Gaglione, N. Geffroy, J. Jacquemier, Y. Karyotakis, G. Martin-Chassard, J. Prast, N. Seguin-Moreau, C. de La Taille, and A. Vouters, "MICROROC: MICRO-mesh gaseous structure Read-Out Chip," *Journal of Instrumentation*, vol. 7, no. 01, p. C01029, 2012.

[6] D. Curtin, R. Essig, S. Gori, P. Jaiswal, A. Katz, T. Liu, Z. Liu, D. McKeen, J. Shelton, M. Strassler, *et al.*, "Exotic decays of the 125 GeV Higgs boson," *Physical Review D*, vol. 90, no. 7, p. 075004, 2014.

[7] G. Apollinari, O. Brüning, T. Nakamoto, and L. Rossi, "High Luminosity Large Hadron Collider HL-LHC," *arXiv preprint arXiv:1705.08830*, 2017.

[8] M. E. Peskin, "Comparison of LHC and ILC capabilities for Higgs boson coupling measurements," *arXiv preprint arXiv:1207.2516*, 2012.

[9] H. Baer, T. Barklow, K. Fujii, Y. Gao, A. Hoang, S. Kanemura, J. List, H. E. Logan, A. Nomerotski, M. Perelstein, *et al.*, "The International linear collider technical design report-volume 2: physics," *arXiv preprint arXiv:1306.6352*, 2013.

[10] T. Behnke, J. E. Brau, P. N. Burrows, J. Fuster, M. Peskin, M. Stanitzki, Y. Sugimoto, S. Yamada, and H. Yamamoto, "The International Linear Collider Technical Design Report-Volume 4: Detectors ," *arXiv preprint arXiv:1306.6329*, 2013.

[11] L. Linssen, A. Miyamoto, M. Stanitzki, and H. Weerts, "Physics and detectors at CLIC: CLIC conceptual design report ," *arXiv preprint arXiv:1202.5940*, 2012.

[12] Q. Qin *et al.*, “Overview of the CEPC Accelerator ,” in *55th ICFA Advanced Beam Dynamics Workshop on High Luminosity Circular e+ e-Colliders–Higgs Factory (HF2014)*, 2014.

[13] W. Dou, G. Jie, X. Ming, G. Hui-Ping, G. Yuan-Yuan, X. Shou-Yan, W. Na, A. Yu-Wen, Q. Qing, X. Gang, *et al.*, “Optimization parameter design of a circular e+ e- Higgs factory ,” *Chinese physics C*, vol. 37, no. 9, p. 097003, 2013.

[14] A. Bernstein, T. Bienz, A. Caldwell, L. Chen, M. Derrick, I. Gialas, A. Hamri, R. Imlay, S. Kartik, H. Kim, *et al.*, “Beam tests of the ZEUS barrel calorimeter,” *Nuclear Instruments and Methods in Physics Research Section A: Accelerators, Spectrometers, Detectors and Associated Equipment*, vol. 336, no. 1-2, pp. 23–52, 1993.

[15] The ATLAS collaboration, “Jet reconstruction and performance using particle flow with the ATLAS Detector ,” Tech. Rep. 7, Jul 2017.

[16] The CMS collaboration, “Jet energy scale and resolution in the CMS experiment in pp collisions at 8 TeV ,” *The European Physical Journal C*, vol. 77, no. 11, 2017.

[17] A. Rubin, L. Arazi, S. Bressler, L. Moleri, M. Pitt, and A. Breskin, “First studies with the Resistive-Plate WELL gaseous multiplier,” *Journal of Instrumentation*, vol. 8, no. 11, p. P11004, 2013.

[18] H. Yang, “Preliminary conceptual design about the CEPC calorimeters,” *International Journal of Modern Physics A*, vol. 31, no. 33, p. 1644026, 2016.

[19] H. Aihara, P. Burrows, and M. Oreglia, “Silicon Detector Letter of Intent,” tech. rep., SLAC National Accelerator Laboratory (SLAC), 2010.

[20] The ILD concept group, "The international large detector: Letter of intent," tech. rep., 2010.

[21] V. L. Fitch, *Elementary Particle Physics: The Origins* , pp. 43–55. New York, NY: Springer New York, 1999.

[22] C. T. Wilson, "On the cloud method of making visible ions and the tracks of ionizing particles," *Nobel lectures in physics*, 1927.

[23] C. Anderson, "Nobel Lecture: The production and properties of positrons," 1965.

[24] P. Blackett, *Cloud Chamber Researches in Nuclear Physics and Cosmic Radiation.* Norstedt, 1949.

[25] E. Rutherford, "An electrical method of counting the number of $\alpha$-particles from radio-active substances," *Proceedings of the Royal Society of London. Series A, Containing Papers of a Mathematical and Physical Character*, vol. 81, no. 546, pp. 141–161, 1908.

[26] S. C. Curran, "The New Counters," *Science Progress (1933-)*, vol. 42, no. 165, pp. 32–45, 1954.

[27] H. Yukawa, "Meson theory in its developments," *Nobel lectures in physics*, 1949.

[28] C. F. Powell, "The cosmic radiation," *Nobel Lecture, December*, vol. 11, 1950.

[29] A. Langsdorf Jr, "A continuously sensitive diffusion cloud chamber," *Review of Scientific Instruments*, vol. 10, no. 3, pp. 91–103, 1939.

[30] D. A. Glaser, "Elementary particles and bubble chambers," *Noble Lecture, December*, vol. 12, 1960.

[31] I. Falomkin, M. Kulyukin, G. Pontecorvo, and Y. A. Sherbakov, "Highly localized bright tracks in helium-filled streamer chamber ," *Nuclear Instruments and Methods*, vol. 53, pp. 266–272, 1967.

[32] J. Bienlein, A. Böhm, G. von Dardel, H. Faissner, F. Ferrero, J.-M. Gaillard, H. Gerber, B. Hahn, V. Kaftanov, F. Krienen, *et al.*, "Spark chamber study of high-energy neutrino interactions ," *Physics Letters*, vol. 13, no. 1, pp. 80–86, 1964.

[33] R. Cobb, J. Duthie, and J. Stewart, "Spark-Chamber Experiment on Cosmic Gamma Rays ," *Physical Review Letters*, vol. 15, no. 12, p. 507, 1965.

[34] G. Charpak, "Electronic imaging of ionizing radiation with limited avalanches in gases," *Reviews of modern physics*, vol. 65, no. 3, p. 591, 1993.

[35] M. Schwartz, "The first high-energy neutrino experiment," *Reviews of Modern Physics*, vol. 61, no. 3, p. 527, 1989.

[36] G. Charpak, R. Bouclier, T. Bressani, J. Favier, and Č. Zupančič, "The use of multiwire proportional counters to select and localize charged particles," *Nuclear Instruments and Methods*, vol. 62, no. 3, pp. 262–268, 1968.

[37] C. Rubbia, "Experimental observation of the intermediate vector bosons $W^+$, $W^-$, and $Z^0$," *Reviews of Modern Physics*, vol. 57, no. 3, p. 699, 1985.

[38] T. Bressani, D. Rahm, G. Charpak, and C. Zupancic, "Track localization by means of a drift chamber ," 1969.

[39] D. R. Nygren, "The time projection chamber: A new 4 pi detector for charged particles ," *eConf*, vol. 740805, no. PEP-0144, p. 58, 1976.

[40] J. Alme, Y. Andres, H. Appelshäuser, S. Bablok, N. Bialas, R. Bolgen, U. Bonnes, R. Bramm, P. Braun-Munzinger, R. Campagnolo, *et al.*, "The ALICE TPC, a large 3-dimensional tracking device with fast readout for ultra-high multiplicity events ," *Nuclear Instruments and Methods in Physics Research Section A: Accelerators, Spectrometers, Detectors and Associated Equipment*, vol. 622, no. 1, pp. 316–367, 2010.

[41] J. Thomas, "A TPC for measuring high multiplicity events at RHIC ," *Nuclear Instruments and Methods in Physics Research Section A: Accelerators, Spectrometers, Detectors and Associated Equipment*, vol. 478, no. 1, pp. 166–169, 2002.

[42] S. Majewski, G. Charpak, A. Breskin, and G. Mikenberg, "A thin multiwire chamber operating in the high multiplication mode ," *Nuclear Instruments and Methods in Physics Research*, vol. 217, no. 1, pp. 265–271, 1983.

[43] A. Abusleme, C. Bélanger-Champagne, A. Bellerive, Y. Benhammou, J. Botte, H. Cohen, M. Davies, Y. Du, L. Gauthier, T. Koffas, *et al.*, "Performance of a full-size small-strip thin gap chamber prototype for the ATLAS new small wheel muon upgrade ," *Nuclear Instruments and Methods in Physics Research Section A: Accelerators, Spectrometers, Detectors and Associated Equipment*, vol. 817, pp. 85–92, 2016.

[44] V. Sola, R. Arcidiacono, A. Bellora, N. Cartiglia, F. Cenna, R. Cirio, S. Durando, M. Ferrero, Z. Galloway, B. Gruey, *et al.*, "Ultra-Fast Silicon Detectors for 4D tracking," *Journal of Instrumentation*, vol. 12, no. 02, p. C02072, 2017.

[45] A. N. Otte and D. Garcia, "A very brief review of recent SiPM developments," in *International Conference on New Photo-detectors*, vol. 6, p. 9, 2015.

[46] S. Dalla Torre, "The Brilliant Present and the Promising Perspectives of the Micropattern Gaseous Detectors," *Nuclear Physics News*, vol. 26, no. 3, pp. 9–13, 2016.

[47] F. Sauli, "Radiation imaging with gaseous detectors," *Nuclear Instruments and Methods in Physics Research Section A: Accelerators, Spectrometers, Detectors and Associated Equipment*, 2017.

[48] F. Sauli, *Gaseous radiation detectors: fundamentals and applications.* No. 36, Cambridge University Press, 2014.

[49] R. Chechik, A. Breskin, C. Shalem, and D. Mörmann, "Thick GEM-like hole multipliers: properties and possible applications," *Nuclear Instruments and Methods in Physics Research Section A: Accelerators, Spectrometers, Detectors and Associated Equipment*, vol. 535, no. 1, pp. 303–308, 2004.

[50] A. Lyashenko, A. Breskin, R. Chechik, J. Veloso, J. Dos Santos, and F. Amaro, "Development of high-gain gaseous photomultipliers for the visible spectral range," *Journal of Instrumentation*, vol. 4, no. 07, p. P07005, 2009.

[51] M. Cortesi, R. Zboray, R. Adams, V. Dangendorf, and H.-M. Prasser, "Concept of a novel fast neutron imaging detector based on THGEM for fan-beam tomography applications," *Journal of Instrumentation*, vol. 7, no. 02, p. C02056, 2012.

[52] T. Francke, *Innovative applications and developments of micro-pattern gaseous detectors.* IGI Global, 2014.

[53] R. Veenhof, "Garfield - simulation of gaseous detectors," tech. rep., CERN.

[54] S. Biagi, "Magboltz - transport of electrons in gas mixtures," tech. rep., CERN.

[55] A. Oed, "Position-sensitive detector with microstrip anode for electron multiplication with gases," *Nuclear Instruments and Methods in Physics Research Section A: Accelerators, Spectrometers, Detectors and Associated Equipment*, vol. 263, no. 2-3, pp. 351–359, 1988.

[56] F. Sauli, "GEM: A new concept for electron amplification in gas detectors," *Nuclear Instruments and Methods in Physics Research Section A: Accelerators, Spectrometers, Detectors and Associated Equipment*, vol. 386, no. 2-3, pp. 531–534, 1997.

[57] Y. Giomataris, P. Rebourgeard, J. P. Robert, and G. Charpak, "MICROMEGAS: a high-granularity position-sensitive gaseous detector for high particle-flux environments," *Nuclear Instruments and Methods in Physics Research Section A: Accelerators, Spectrometers, Detectors and Associated Equipment*, vol. 376, no. 1, pp. 29–35, 1996.

[58] F. Amaro, C. Santos, J. Veloso, A. Breskin, R. Chechik, and J. Dos Santos, "The Thick-COBRA: a new gaseous electron multiplier for radiation detectors," *Journal of Instrumentation*, vol. 5, no. 10, p. P10002, 2010.

[59] S. Bressler, L. Arazi, L. Moleri, M. Pitt, A. Rubin, and A. Breskin, "Recent advances with THGEM detectors," *Journal of Instrumentation*, vol. 8, no. 12, p. C12012, 2013.

[60] J. Veloso, J. Dos Santos, and C. Conde, "A proposed new microstructure for gas radiation detectors: The microhole and strip plate ," *Review of Scientific Instruments*, vol. 71, no. 6, pp. 2371–2376, 2000.

[61] M. Cortesi, S. Rost, W. Mittig, Y. Ayyad-Limonge, D. Bazin, J. Yurkon, and A. Stolz, "Multi-layer thick gas electron multiplier (M-THGEM): A new MPGD

structure for high-gain operation at low-pressure ," *Review of Scientific Instruments*, vol. 88, no. 1, p. 013303, 2017.

[62] A. Ochi, T. Nagayoshi, S. Koishi, T. Tanimori, T. Nagae, and M. Nakamura, "Development of micro pixel chamber ," *Nuclear Instruments and Methods in Physics Research Section A: Accelerators, Spectrometers, Detectors and Associated Equipment*, vol. 478, no. 1, pp. 196–199, 2002.

[63] V. Peskov, E. Silin, T. Sokolova, and I. Radionov, "First attempts to combine capillary tubes with photocathodes ," *Nuclear Instruments and Methods in Physics Research Section A: Accelerators, Spectrometers, Detectors and Associated Equipment*, vol. 433, no. 1, pp. 492–501, 1999.

[64] M. Chefdeville, P. Colas, Y. Giomataris, H. van der Graaf, E. H. Heijne, S. van der Putten, C. Salm, J. Schmitz, S. Smits, J. Timmermans, *et al.*, "An electron-multiplying Micromegas grid made in silicon wafer post-processing technology ," *Nuclear Instruments and Methods in Physics Research Section A: Accelerators, Spectrometers, Detectors and Associated Equipment*, vol. 556, no. 2, pp. 490–494, 2006.

[65] F. Tessarotto *et al.*, "THGEM-based photon detectors for the upgrade of COMPASS RICH-1," *Nuclear Instruments and Methods in Physics Research Section A: Accelerators, Spectrometers, Detectors and Associated Equipment*, vol. 732, pp. 264–268, 2013.

[66] S. Murphy *et al.*, "The WA105-3x1x1 $m^3$ dual phase LAr-TPC demonstrator," *arXiv preprint arXiv:1611.05846*, 2016.

[67]

[68] F. Kuger, A. Collaboration, *et al.*, “Performance studies of resistive Micromegas detectors for the upgrade of the ATLAS Muon spectrometer ,” *Nuclear Instruments and Methods in Physics Research Section A: Accelerators, Spectrometers, Detectors and Associated Equipment*, vol. 845, pp. 248–252, 2017.

[69] M. Bagliesi, M. Berretti, E. Brucken, R. Cecchi, E. David, F. Garcia, V. Greco, J. Heino, T. Hilden, K. Kurvinen, *et al.*, “The TOTEM T2 telescope based on triple-GEM chambers ,” *Nuclear Instruments and Methods in Physics Research Section A: Accelerators, Spectrometers, Detectors and Associated Equipment*, vol. 617, no. 1, pp. 134–137, 2010.

[70] Z. Fraenkel, A. Kozlov, M. Naglis, I. Ravinovich, L. Shekhtman, I. Tserruya, B. Azmoun, C. Woody, S. Sawada, S. Yokkaichi, *et al.*, “A hadron blind detector for the PHENIX experiment at RHIC ,” *Nuclear Instruments and Methods in Physics Research Section A: Accelerators, Spectrometers, Detectors and Associated Equipment*, vol. 546, no. 3, pp. 466–480, 2005.

[71] S. White, “PICOSEC: Charged particle timing to 24 picosecond precision with MicroPattern gas detectors ,” *Nuclear Instruments and Methods in Physics Research Section A: Accelerators, Spectrometers, Detectors and Associated Equipment*, 2017.

[72] F. Resnati, A. Badertscher, A. Curioni, S. Horikawa, L. Knecht, D. Lussi, A. Marchionni, G. Natterer, A. Rubbia, and T. Viant, “Stable operation with gain of a double phase Liquid Argon LEM-TPC with a 1 mm thick segmented LEM ,” in *Journal of Physics: Conference Series*, vol. 308, p. 012016, IOP Publishing, 2011.

[73] A. Buzulutskov, “Advances in cryogenic avalanche detectors ,” *Journal of Instrumentation*, vol. 7, no. 02, p. C02025, 2012.

[74] S. Duval, A. Breskin, R. Budnik, W. Chen, H. Carduner, M. Cortesi, J. Cussonneau, J. Donnard, J. Lamblin, P. Le Ray, *et al.*, "On the operation of a micropattern gaseous UV-photomultiplier in liquid-Xenon ," *Journal of Instrumentation*, vol. 6, no. 04, p. P04007, 2011.

[75] L. Arazi, E. Erdal, A. Coimbra, M. Rappaport, D. Vartsky, V. Chepel, and A. Breskin, "Liquid Hole Multipliers: bubble-assisted electroluminescence in liquid xenon," *Journal of Instrumentation*, vol. 10, no. 08, p. P08015, 2015.

[76] D. Vartsky, I. Israelashvili, M. Cortesi, L. Arazi, A. Coimbra, L. Moleri, E. Erdal, D. Bar, M. Rappaport, S. Shchemelinin, *et al.*, "Liquid-Xe detector for contraband detection ," *Nuclear Instruments and Methods in Physics Research Section A: Accelerators, Spectrometers, Detectors and Associated Equipment*, vol. 824, pp. 240–242, 2016.

[77] I. Israelashvili, A. Coimbra, D. Vartsky, L. Arazi, S. Shchemelinin, E. Caspi, and A. Breskin, "Fast-neutron and gamma-ray imaging with a capillary liquid xenon converter coupled to a gaseous photomultiplier ," *Journal of Instrumentation*, vol. 12, no. 09, p. P09029, 2017.

[78] L. De Nardo and M. Farahmand, "Operation of gas electron multiplier (GEM) with propane gas at low pressure and comparison with tissue-equivalent gas mixtures," *Nuclear Instruments and Methods in Physics Research Section A: Accelerators, Spectrometers, Detectors and Associated Equipment*, vol. 819, pp. 154–162, 2016.

[79] C. Shalem, R. Chechik, A. Breskin, K. Michaeli, and N. Ben-Haim, "Advances in thick GEM-like gaseous electron multipliers Part II: Low-pressure operation ," *Nuclear Instruments and Methods in Physics Research Section A: Ac-*

*celerators, Spectrometers, Detectors and Associated Equipment*, vol. 558, no. 2, pp. 468–474, 2006.

[80] K. Gnanvo, "New Trends in Micro Pattern Gaseous Detectors (MPGDs)," *Bulletin of the American Physical Society*, vol. 61, 2016.

[81] Y. Jia-Qing, X. Yu-Guang, H. Tao, L. Jun-Guang, Z. Li, Q. Guo-Pu, C. Xiao, N. Shun-Li, and C. Hai-Tao, "Simulation and performance study of ceramic THGEM," *Chinese physics C*, vol. 39, no. 6, p. 066001, 2015.

[82] M. Morales, C. Pecharroman, G. Mata-Osoro, L. Diaz, and J. Garzon, "Conductivity and charge depletion aging of resistive electrodes for high rate RPCs," *Journal of Instrumentation*, vol. 8, no. 01, p. P01022, 2013.

[83] G. Alekseev, N. Kalinina, V. Karpukhin, D. Khazins, and V. Kruglov, "Investigation of self-quenching streamer discharge in a wire chamber ," *Nuclear Instruments and Methods*, vol. 177, no. 2-3, pp. 385–397, 1980.

[84] H. Raether, *Electron avalanches and breakdown in gases.* Butterworths, 1964.

[85] V. Peskov, B. Ramsey, and P. Fonte, "Breakdown features of various microstrip-type gas counter designs and their improvements," *IEEE Transactions on nuclear science*, vol. 45, no. 3, pp. 244–248, 1998.

[86] R. Waters, J. Meek, and J. Craggs, "Spark breakdown in non-uniform fields," *Electrical breakdown of gases*, p. 385, 1978.

[87] J. Y. Won and P. Williams, "Experimental study of streamers in pure N2 and $N_2/O_2$ mixtures and a$\sim$ 13 cm gap," *Journal of Physics D: Applied Physics*, vol. 35, no. 3, p. 205, 2002.

[88] U. Ebert, W. van Saarloos, and C. Caroli, "Propagation and structure of planar streamer fronts ," *Physical Review E*, vol. 55, no. 2, p. 1530, 1997.

[89] S. Franchino, D. G. Diaz, R. Hall-Wilton, H. Müller, E. Oliveri, D. Pfeiffer, F. Resnati, L. Ropelewski, M. Van Stenis, C. Streli, *et al.*, "Effects of high charge densities in multi-GEM detectors," in *Nuclear Science Symposium and Medical Imaging Conference (NSS/MIC), 2015 IEEE*, pp. 1–5, IEEE, 2015.

[90] P. Gasik, A. Mathis, L. Fabbietti, and J. Margutti, "Charge density as a driving factor of discharge formation in GEM-based detectors," *Nuclear Instruments and Methods in Physics Research Section A: Accelerators, Spectrometers, Detectors and Associated Equipment*, vol. 870, pp. 116–122, 2017.

[91] J. Allison *et al.*, "GEANT4a simulation toolkit," *Nuclear instruments and methods in physics research section A: Accelerators, Spectrometers, Detectors and Associated Equipment*, vol. 506, no. 3, pp. 250–303, 2003.

[92] S. Bressler, L. Moleri, L. Arazi, E. Erdal, A. Rubin, M. Pitt, and A. Breskin, "A concept for laboratory studies of radiation detectors over a broad dynamic-range: instabilities evaluation in THGEM-structures," *Journal of Instrumentation*, vol. 9, no. 03, p. P03005, 2014.

[93] R. Santonico and R. Cardarelli, "Development of resistive plate counters ," *Nuclear Instruments and Methods in physics research*, vol. 187, no. 2-3, pp. 377–380, 1981.

[94] V. Parkhomchuck, Y. N. Pestov, and N. Petrovykh, "A spark counter with large area," *Nuclear Instruments and Methods*, vol. 93, no. 2, pp. 269–270, 1971.

[95] H. Schmidt, "Pestov spark counters: work principle and applications," *Nuclear Physics B-Proceedings Supplements*, vol. 78, no. 1-3, pp. 372–380, 1999.

[96] Y. N. Pestov, "Review on counters with localized discharge," *Nuclear Instruments and Methods in Physics Research Section A: Accelerators, Spectrometers, Detectors and Associated Equipment*, vol. 494, no. 1, pp. 447–454, 2002.

[97] D. Gonzalez-Diaz, P. Fonte, J. Garzón, and A. Mangiarotti, "An analytical description of rate effects in timing RPCs," *Nuclear Physics B-Proceedings Supplements*, vol. 158, pp. 111–117, 2006.

[98] P. Fonte, "Review of RPC simulation and modelling ," *PoS*, p. 033, 2012.

[99] G. Bencivenni, R. De Oliveira, G. Morello, and M. P. Lener, "The micro-Resistive WELL detector: a compact spark-protected single amplification-stage MPGD ," *Journal of Instrumentation*, vol. 10, no. 02, p. P02008, 2015.

[100] Y. Bilevych, V. B. Carballo, M. Chefdeville, P. Colas, E. Delagnes, M. Fransen, H. Van Der Graaf, W. Koppert, J. Melai, C. Salm, B. Schmitz, J. Timmermans, and N. Wyrsch, "Spark protection layers for CMOS pixel anode chips in MPGDs," *Nuclear Instruments and Methods in Physics Research Section A: Accelerators, Spectrometers, Detectors and Associated Equipment*, vol. 629, no. 1, pp. 66–73, 2011.

[101] I. Crotty, J. L. Valverde, G. Laurenti, M. Williams, and A. Zichichi, "The non-spark mode and high rate operation of resistive parallel plate chambers ," *Nuclear Instruments and Methods in Physics Research Section A: Accelerators, Spectrometers, Detectors and Associated Equipment*, vol. 337, no. 2-3, pp. 370–381, 1994.

[102] M. Chefdeville, "Charge-up effects in resistive Micromegas Their impact on sparking & detector performance." Presented at RD51 mini-week, December 2015.

[103] T.-H. Lin, A. Düdder, M. Schott, C. Valderanis, L. Wehner, and R. Westenberger, "Signal characteristics of a resistive-strip micromegas detector with an integrated two-dimensional readout ," *Nuclear Instruments and Methods in Physics Research Section A: Accelerators, Spectrometers, Detectors and Associated Equipment*, vol. 767, pp. 281–288, 2014.

[104] W. Riegler, "Electric fields, weighting fields, signals and charge diffusion in detectors including resistive materials ," *Journal of Instrumentation*, vol. 11, no. 11, p. P11002, 2016.

[105] M. S. Dixit, J. Dubeau, J.-P. Martin, and K. Sachs, "Position sensing from charge dispersion in micro-pattern gas detectors with a resistive anode ," *Nuclear Instruments and Methods in Physics Research Section A: Accelerators, Spectrometers, Detectors and Associated Equipment*, vol. 518, no. 3, pp. 721–727, 2004.

[106] M. Cortesi, R. Alon, R. Chechik, A. Breskin, D. Vartsky, and V. Dangendorf, "Investigations of a THGEM-based imaging detector ," *Journal of Instrumentation*, vol. 2, no. 09, p. P09002, 2007.

[107] T. Alexopoulos, J. Burnens, R. De Oliveira, G. Glonti, O. Pizzirusso, V. Polychronakos, G. Sekhniaidze, G. Tsipolitis, and J. Wotschack, "A spark-resistant bulk-micromegas chamber for high-rate applications," *Nuclear Instruments and Methods in Physics Research Section A: Accelerators, Spectrometers, Detectors and Associated Equipment*, vol. 640, no. 1, pp. 110–118, 2011.

[108] M. Chefdeville, Y. Karyotakis, T. Geralis, and M. Titov, "Resistive Micromegas for sampling calorimetry, a study of charge-up effects ," *Nuclear Instruments and Methods in Physics Research Section A: Accelerators, Spectrometers, Detectors and Associated Equipment*, vol. 824, pp. 510–511, 2016.

[109] R. Oliveira, V. Peskov, F. Pietropaolo, and P. Picchi, "First tests of thick GEMs with electrodes made of a resistive kapton ," *Nuclear Instruments and Methods in Physics Research Section A: Accelerators, Spectrometers, Detectors and Associated Equipment*, vol. 576, no. 2, pp. 362–366, 2007.

[110] P. Fonte, N. Carolino, L. Costa, R. Ferreira-Marques, S. Mendiratta, V. Peskov, and A. Policarpo, "A spark-protected high-rate detector ," *Nuclear Instruments and Methods in Physics Research Section A: Accelerators, Spectrometers, Detectors and Associated Equipment*, vol. 431, no. 1, pp. 154–159, 1999.

[111] A. Breskin, R. Alon, M. Cortesi, R. Chechik, J. Miyamoto, V. Dangendorf, J. Maia, and J. Dos Santos, "A concise review on THGEM detectors," *Nuclear Instruments and Methods in Physics Research Section A: Accelerators, Spectrometers, Detectors and Associated Equipment*, vol. 598, no. 1, pp. 107–111, 2009.

[112] C. Shalem, R. Chechik, A. Breskin, and K. Michaeli, "Advances in Thick GEM-like gaseous electron multipliers-Part I: atmospheric pressure operation," *Nuclear Instruments and Methods in Physics Research Section A: Accelerators, Spectrometers, Detectors and Associated Equipment*, vol. 558, no. 2, pp. 475–489, 2006.

[113] M. Cortesi, R. Chechik, A. Breskin, G. Guedes, V. Dangendorf, D. Vartzky, and D. Bar, "Advances in imaging THGEM-based detectors ," *Nuclear Instruments and Methods in Physics Research Section A: Accelerators, Spectrometers, Detectors and Associated Equipment*, vol. 572, no. 1, pp. 175–176, 2007.

[114] R. Alon, J. Miyamoto, M. Cortesi, A. Breskin, R. Chechik, I. Carne, J. Maia, J. dos Santos, M. Gai, D. McKinsey, *et al.*, "Operation of a thick gas electron

multiplier (THGEM) in Ar, Xe and Ar-Xe ," *Journal of Instrumentation*, vol. 3, no. 01, p. P01005, 2008.

[115] R. Alon, M. Cortesi, A. Breskin, and R. Chechik, "Time resolution of a Thick Gas Electron Multiplier (THGEM)-based detector ," *Journal of Instrumentation*, vol. 3, no. 11, p. P11001, 2008.

[116] J. Maia, J. dos Santos, A. Breskin, and R. Chechik, "THGEM electron multiplier in high pressure Kr ," *Journal of Instrumentation*, vol. 4, no. 10, p. P10006, 2009.

[117] M. Cortesi, V. Peskov, G. Bartesaghi, J. Miyamoto, S. Cohen, R. Chechik, J. Maia, J. dos Santos, G. Gambarini, V. Dangendorf, *et al.*, "THGEM operation in Ne and Ne/$CH_4$," *Journal of Instrumentation*, vol. 4, no. 08, p. P08001, 2009.

[118] V. Peskov, M. Cortesi, R. Chechik, and A. Breskin, "Further evaluation of a THGEM UV-photon detector for RICH–comparison with MWPC ," *Journal of Instrumentation*, vol. 5, no. 11, p. P11004, 2010.

[119] J. Miyamoto, A. Breskin, and V. Peskov, "Gain limits of a Thick GEM in high-purity Ne, Ar and Xe ," *Journal of Instrumentation*, vol. 5, no. 05, p. P05008, 2010.

[120] C. Azevedo, M. Cortesi, A. Lyashenko, A. Breskin, R. Chechik, J. Miyamoto, V. Peskov, J. Escada, J. Veloso, and J. dos Santos, "Towards THGEM UV-photon detectors for RICH: on single-photon detection efficiency in Ne/$CH_4$ and Ne/$CF_4$ ," *Journal of Instrumentation*, vol. 5, no. 01, p. P01002, 2010.

[121] A. Breskin, M. Cortesi, R. Alon, J. Miyamoto, V. Peskov, G. Bartesaghi, R. Chechik, V. Dangendorf, J. Maia, and J. dos Santos, "The THGEM: A thick

robust gaseous electron multiplier for radiation detectors ," *Nuclear Instruments and Methods in Physics Research Section A: Accelerators, Spectrometers, Detectors and Associated Equipment*, vol. 623, no. 1, pp. 132–134, 2010.

[122] A. Breskin, V. Peskov, M. Cortesi, R. Budnik, R. Chechik, S. Duval, D. Thers, A. Coimbra, J. Dos Santos, J. Lopes, *et al.*, "CsI-THGEM gaseous photomultipliers for RICH and noble-liquid detectors ," *Nuclear Instruments and Methods in Physics Research Section A: Accelerators, Spectrometers, Detectors and Associated Equipment*, vol. 639, no. 1, pp. 117–120, 2011.

[123] J. Veloso, C. Santos, F. Pereira, C. Azevedo, F. Amaro, J. Dos Santos, A. Breskin, and R. Chechik, "THCOBRA: Ion back flow reduction in patterned THGEM cascades ," *Nuclear Instruments and Methods in Physics Research Section A: Accelerators, Spectrometers, Detectors and Associated Equipment*, vol. 639, no. 1, pp. 134–136, 2011.

[124] A. Coimbra, A. Breskin, and J. dos Santos, "THGEM operation in high pressure Ne/$CF_4$ ," *Journal of Instrumentation*, vol. 7, no. 02, p. C02062, 2012.

[125] L. Arazi, H. N. da Luz, D. Freytag, M. Pitt, C. Azevedo, A. Rubin, M. Cortesi, D. Covita, C. Oliveira, E. Oliveri, *et al.*, "THGEM-based detectors for sampling elements in DHCAL: laboratory and beam evaluation," *Journal of Instrumentation*, vol. 7, no. 05, p. C05011, 2012.

[126] A. Coimbra, A. Conceição, J. Mir, A. Rubin, M. Pitt, A. Breskin, C. Henriques, and J. dos Santos, "First results with THGEM followed by submillimetric multiplying gap," *Journal of Instrumentation*, vol. 8, no. 06, p. P06004, 2013.

[127] L. Arazi, C. D. R. Azevedo, A. Breskin, S. Bressler, L. Moleri, H. N. da Luz, E. Oliveri, M. Pitt, A. Rubin, J. M. F. dos Santos, J. F. C. d. A. Veloso, and

A. P. White, “Beam studies of the segmented resistive WELL: a potential thin sampling element for digital hadron calorimetry ,” *Nuclear Instruments and Methods in Physics Research Section A: Accelerators, Spectrometers, Detectors and Associated Equipment*, vol. 732, pp. 199–202, 2013.

[128] S. Bressler, L. Arazi, H. N. da Luz, C. Azevedo, L. Moleri, E. Oliveri, M. Pitt, A. Rubin, J. dos Santos, J. Veloso, and A. Breskin, “Beam studies of novel THGEM-based potential sampling elements for Digital Hadron Calorimetry,” *Journal of Instrumentation*, vol. 8, no. 07, p. P07017, 2013.

[129] L. Arazi, M. Pitt, S. Bressler, L. Moleri, A. Rubin, and A. Breskin, “Laboratory studies of THGEM-based WELL structures with resistive anode,” *Journal of Instrumentation*, vol. 9, no. 04, p. P04011, 2014.

[130] I. Israelashvili, M. Cortesi, D. Vartsky, L. Arazi, D. Bar, E. Caspi, and A. Breskin, “A comprehensive simulation study of a Liquid-Xe detector for contraband detection,” *Journal of Instrumentation*, vol. 10, no. 03, p. P03030, 2015.

[131] A. Bondar, A. Buzulutskov, A. Grebenuk, D. Pavlyuchenko, Y. Tikhonov, and A. Breskin, “Thick GEM versus thin GEM in two-phase argon avalanche detectors ,” *Journal of Instrumentation*, vol. 3, no. 07, p. P07001, 2008.

[132] A. Bondar, A. Buzulutskov, A. Dolgov, A. Grebenuk, E. Shemyakina, A. Sokolov, D. Akimov, A. Breskin, and D. Thers, “Two-phase Cryogenic Avalanche Detectors with THGEM and hybrid THGEM/GEM multipliers operated in Ar and Ar+ $N_2$ ,” *Journal of Instrumentation*, vol. 8, no. 02, p. P02008, 2013.

[133] L. Arazi, A. Coimbra, E. Erdal, I. Israelashvili, M. Rappaport, S. Shchemelinin, D. Vartsky, J. dos Santos, and A. Breskin, “First results of a large-area cryogenic

gaseous photomultiplier coupled to a dual-phase liquid xenon TPC ," *Journal of Instrumentation*, vol. 10, no. 10, p. P10020, 2015.

[134] E. Erdal, L. Arazi, M. Rappaport, S. Shchemelinin, D. Vartsky, and A. Breskin, "First demonstration of VUV-photon detection in liquid xenon with THGEM and GEM-based liquid hole multipliers ," *Nuclear Instruments and Methods in Physics Research Section A: Accelerators, Spectrometers, Detectors and Associated Equipment*, vol. 845, pp. 218–221, 2017.

[135] Alexeev *et al.*, "Progresses in the production of large-size THGEM boards ," *Journal of Instrumentation*, vol. 9, no. 03, p. C03046, 2014.

[136] S. Levorato *et al.*, "The MPGD-based photon detectors for the upgrade of COMPASS RICH-1 ," *Nuclear Instruments and Methods in Physics Research Section A: Accelerators, Spectrometers, Detectors and Associated Equipment*, 2017.

[137] M. Cortesi, R. Zboray, R. Adams, V. Dangendorf, M. Meshkian, and H.-M. Prasser, "Development of large-area THGEM detectors for investigation of thermal-hydraulic phenomena using neutron imaging ," *Journal of Instrumentation*, vol. 8, no. 10, p. C10009, 2013.

[138] Y.-N. Zhang, Q. Liu, H.-B. Liu, Y.-G. Xie, X.-R. Lyu, S. Chen, W.-Q. Huang, D.-J. Hong, and Y.-H. Zheng, "Study of a sealed high gas pressure THGEM detector and response of alpha particle spectra ," *Chinese Physics C*, vol. 41, no. 4, p. 046001, 2017.

[139] K. Li, J.-R. Zhou, X.-D. Wang, T. Xiong, Y. Zhang, Y.-G. Xie, L. Zhou, H. Xu, G.-A. Yang, Y.-F. Wang, Y. Wang, J.-J. Wu, Z.-J. Sun, and B.-T. Hu, "Study

of a nTHGEM-based thermal neutron detector ," *Chinese physics C*, vol. 40, no. 7, p. 076002, 2016.

[140] Y. Ayyad, M. Cortesi, W. Mittig, and D. Bazin, "$CO_2$ operation of an active target detector readout based on THGEM. ," *Journal of Instrumentation*, vol. 12, no. 06, p. P06003, 2017.

[141] R. Chechik, A. Breskin, and C. Shalem, "Thick GEM-like multipliers-a simple solution for large area UV-RICH detectors," *Nuclear Instruments and Methods in Physics Research Section A: Accelerators, Spectrometers, Detectors and Associated Equipment*, vol. 553, no. 1, pp. 35–40, 2005.

[142] V. Peskov, G. Bencze, A. Di Mauro, P. Martinengo, D. Mayani, L. Molnar, E. Nappi, G. Paic, N. Smirnov, H. Anand, *et al.*, "First observation of Cherenkov rings with a large area CsI-TGEM-based RICH prototype ," *Nuclear Instruments and Methods in Physics Research Section A: Accelerators, Spectrometers, Detectors and Associated Equipment*, vol. 695, pp. 154–158, 2012.

[143] L. Naumann, R. Kotte, D. Stach, and J. Wüstenfeld, "Ceramics high rate timing RPC," *Nuclear Instruments and Methods in Physics Research Section A: Accelerators, Spectrometers, Detectors and Associated Equipment*, vol. 628, no. 1, pp. 138–141, 2011.

[144] M. Thomson, "Particle flow calorimetry and the PandoraPFA algorithm," *Nuclear Instruments and Methods in Physics Research Section A: Accelerators, Spectrometers, Detectors and Associated Equipment*, vol. 611, no. 1, pp. 25–40, 2009.

[145] F. Sefkow, A. White, K. Kawagoe, R. Pöschl, and J. Repond, "Experimental tests of particle flow calorimetry," *Reviews of Modern Physics*, vol. 88, no. 1, p. 015003, 2016.

[146] C. Adams, A. Bambaugh, B. Bilki, J. Butler, F. Corriveau, T. Cundiff, G. Drake, K. Francis, B. Furst, V. Guarino, *et al.*, "Design, construction and commissioning of the Digital Hadron Calorimeter-DHCAL," *Journal of Instrumentation*, vol. 11, no. 07, p. P07007, 2016.

[147] B. Bilki, "The CALICE digital hadron calorimeter: calibration and response to pions and positrons," in *Journal of Physics: Conference Series*, vol. 587, p. 012038, IOP Publishing, 2015.

[148] Z. Deng *et al.*, "Resistive Plate Chamber digitization in a hadronic shower environment ," *Journal of Instrumentation*, vol. 11, no. 06, p. P06014, 2016.

[149] J. Repond, "Analysis of Muon Events in the DHCAL," *Physics Procedia*, vol. 37, pp. 347–355, 2012.

[150] M. Chefdeville, Y. Karyotakis, N. Geffroy, R. Gaglione, C. Adloff, G. Vouters, J. Jacquemier, F. Peltier, A. Dalmaz, J. Samarati, and G. Vouters, "Resistive Micromegas for sampling calorimetry," *PoS*, p. 054, 2014.

[151] A. White, J. Yu, and S. Park, "Development of a gas electron multiplier-based digital hadron calorimeter," in *Journal of Physics: Conference Series*, vol. 404, p. 012031, IOP Publishing, 2012.

[152] The CALICE collaboration, "First results of the CALICE SDHCAL technological prototype ," *Journal of Instrumentation*, vol. 11, no. 04, p. P04001, 2016.

[153] J. Wang, Y. Wang, X. Zhu, W. Ding, Y. Li, J. Cheng, N. Herrmann, I. Deppner, Y. Zhang, P. Loizeau, P. Senger, and D. Gonzalez-Diaz, "Development of

multi-gap resistive plate chambers with low-resistive silicate glass electrodes for operation at high particle fluxes and large transported charges," *Nuclear Instruments and Methods in Physics Research Section A: Accelerators, Spectrometers, Detectors and Associated Equipment*, vol. 621, no. 1, pp. 151–156, 2010.

[154] A. Rubin, *Thesis for the degree.* PhD thesis, Weizmann Institute of Science, 2013.

[155] P. Correia, M. Pitt, C. Azevedo, A. Breskin, S. Bressler, C. Oliveira, A. Silva, R. Veenhof, and J. Veloso, "Simulation of gain stability of thgem gas-avalanche particle detectors," *arXiv preprint arXiv:1711.02073*, 2017.

[156] M. Pitt, P. Correia, S. Bressler, A. Coimbra, D. S. Renous, C. Azevedo, J. Veloso, and A. Breskin, "Measurements of charging-up processes in thgem-based particle detectors," *arXiv preprint arXiv:1801.00533*, 2018.

[157] S. Martoiu, H. Müller, A. Tarazona, and J. Toledo, "Development of the scalable readout system for micro-pattern gas detectors and other applications," *Journal of Instrumentation*, vol. 8, no. 03, p. C03015, 2013.

[158] M. French, L. Jones, Q. Morrissey, A. Neviani, R. Turchetta, J. Fulcher, G. Hall, E. Noah, M. Raymond, G. Cervelli, P. Moreira, and G. Marseguerra, "Design and results from the APV25, a deep sub-micron CMOS front-end chip for the CMS tracker," *Nuclear Instruments and Methods in Physics Research Section A: Accelerators, Spectrometers, Detectors and Associated Equipment*, vol. 466, no. 2, pp. 359–365, 2001.

[159] K. Karakostas *et al.*, "Micromegas telescope for the RD51 Test Beams," in *XXVIII Workshop on Recent Advances in Particles Physics and Cosmology*, vol. 26, 2010.

[160] K. Karakostas, "A Tracking Program for RD51 Telescope." work developed for the RD51 collaboration, 2012.

[161] H. Müller, "Femtobox." presented in RD51 miniweek, 2015.

[162] M. Bianco, O. Sidiropoulou, P. Loesel, S. Martoiu, and A. Zibell, "Development and test of a versatile DAQ system based on the ATCA standard," *PoS*, p. 202, 2014.

[163] S. Muhkopadhyay and N. Majumdar, "Computation of 3D MEMS electrostatics using a nearly exact BEM solver ," *Engineering Analysis with Boundary Elements*, vol. 30, no. 8, pp. 687–696, 2006.

[164] I. B. Smirnov, "Modeling of ionization produced by fast charged particles in gases," *Nuclear Instruments and Methods in Physics Research Section A: Accelerators, Spectrometers, Detectors and Associated Equipment*, vol. 554, no. 1, pp. 474–493, 2005.

[165] D. Shaked-Renous, "Resistive-Plate WELL (RPWELL) gas-avalanche radiation detectors: Methods, characterization & properties ," M.Sc. thesis, Weizmann Institute of Science, 2017.

[166] D. S. Renous, A. Roy, A. Breskin, and S. Bressler, "Gain stabilization in micro pattern gaseous detectors: methodology and results," *Journal of Instrumentation*, vol. 12, no. 09, p. P09036, 2017.

[167] Y. Assran and A. Sharma, "Transport properties of operational gas mixtures used at lhc," *arXiv preprint arXiv:1110.6761*, 2011.

[168] C. Adloff, J. Blaha, M. Chefdeville, A. Dalmaz, C. Drancourt, A. Espargilière, R. Gaglione, N. Geffroy, D. Girard, J. Jacquemier, Y. Karyotakis, I. Koletsou,

F. Peltier, J. Samarati, S. Tsigaridas, G. Tsipolitis, and G. Vouters, "Construction and test of a 1×1m$^2$ Micromegas chamber for sampling hadron calorimetry at future lepton colliders," *Nuclear Instruments and Methods in Physics Research Section A: Accelerators, Spectrometers, Detectors and Associated Equipment*, vol. 729, pp. 90–101, 2013.

## List of publications directly related to the present PhD thesis

- Luca Moleri, Fernando Domingues Amaro, Lior Arazi, Carlos Davide Rocha Azevedo, Eraldo Oliveri, Michael Pitt, Jana Schaarschmidt, Dan Shaked-Renous. *"The Resistive-Plate WELL with Argon mixtures A robust gaseous radiation detector."* Nuclear Instruments and Methods in Physics Research Section A: Accelerators, Spectrometers, Detectors and Associated Equipment 845 (2017): 262-265.

- Luca Moleri, Fernando Domingues Amaro, Lior Arazi, Carlos Davide Rocha Azevedo, Amos Breskin, Artur Emanuel Cardoso Coimbra, Eraldo Oliveri, Fabio A. Pereira, Jana Schaarschmidt, Dan Shaked-Renous, Joaquim Marques Ferreira dos Santos, João Filipe Calapez de Albuquerque Veloso, and Shikma Bressler. *"In-beam evaluation of a medium-size Resistive-Plate WELL gaseous particle detector."* Journal of Instrumentation 11, no. 09 (2016): P09013.

- Luca Moleri, Purba Bhattacharya, Artur Emanuel Cardoso Coimbra, Amos Breskin and Shikma Bressler*On the localization properties of a RPWELL gas-avalanche detector.* Journal of Instrumentation 12, no. 10 (2017): P10017.

# Appendix A

# RPWELL prototypes

## A.1 30×30mm$^2$ RPWELL detector for edge-effect studies

A small $30 \times 30$ mm$^2$ RPWELL prototype was assembled in an aluminum chamber (figure 33-a) to study the edge effects, in particular the gain and energy resolution variations in proximity of frames.

A 0.6 mm thick Semitron ESD225 RP was coupled to the anode with double sided conductive tape, as in [1]. The chamber was installed on a moving jig providing X-Y translation in front of an X-ray tube as described in section ??.

The THGEM was 0.4 mm thick, with 0.5 mm diameter holes (and 100 μm rim around them) arranged in a square pattern of 0.96 mm pitch, except a central cross where the pitch was 1.3 mm. In order to study how the signal is affected by the proximity of a frame (edge effect), a 5 mm thick FR4 bar was placed on one side of the THGEM at different distances from the center of the last raw of holes: 0.7 mm and 2.7 mm (figure 33-b and 33-c respectively). The drift gap was 7 mm, and the cathode was the chamber window itself (an aluminized mylar foil glued with epoxy).

(a) (b) (c)

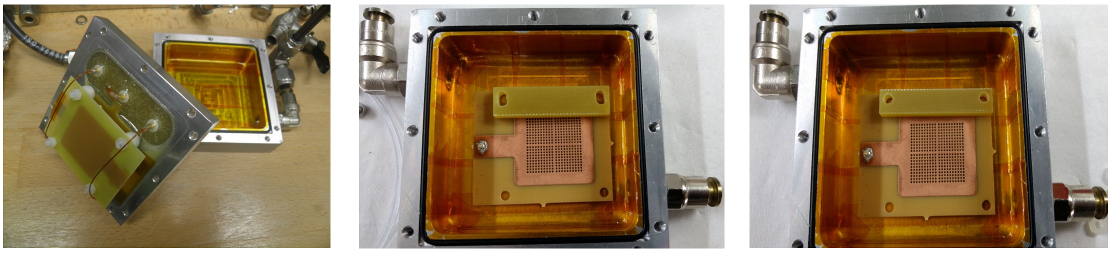

Figure 33: a) The aluminum chamber containing the $30 \times 30$ mm$^2$ RPWELL detector for edge effect studies. b)-c) the frame on top of the THGEM electrode at different distances from the holes line: 0.7 mm and 2.7 mm respectively.

## A.2 100×100mm$^2$ RPWELL detector with RP directly coupled to pads readout

A $100 \times 100$ mm$^2$RPWELL detector was assembled in an aluminum chamber; the latter had a mylar window for x-ray measurements. The detector scheme is sketched in figure 34-a. The single-sided THGEM electrode, 0.86 mm thick, had 0.5 mm diameter holes mechanically drilled in an FR4 plate, copper-clad on one side. 100 µm rims were etched around each hole to remove sharp metal edges, improving the electrical stability at high voltage. The holes were arranged in a square lattice (figure 34-b), with 0.96 mm pitch, so that they cover the underlying $10 \times 10$ mm$^2$ anode pads, but not their borders, where 0.86 mm wide metal bands are left, as described in [125]. The THGEM electrode was coupled to the anode pads (figure 34-d) through a 0.4 mm thick Semitron ESD225 static dissipative acetal plate ($2{\cdot}10^9$ Ωcm bulk resistivity). Efficient clearance of the avalanche electrons was granted by the electrical contact between the resistive plate and the readout pads: the bottom of the resistive material was patterned with conductive pads (figure 34-c), (by 1 mm wide, 50 µm deep machined grooves) into $10 \times 10$ mm$^2$ regions (corresponding to the metal pads of the readout electrode); each of them was coated with silver paint[1] and individually connected to the anode pads using conductive epoxy[2] or conductive tape[3]. The latter is preferable, since it gives a soft bond that doesn't break under mechanical stress (due for example to the acetal expansion when exposed to humidity). The 5 mm drift gap was fixed by delrin spacers. The THGEM electrode, spacers and cathode were assembled on the anode using nylon rods and nuts. More details on the detector assembly are given in [1, 3].

[1] Demetron Leit Silber 200

[2] Circuit Works

[3] 3M Electrically Conductive Adhesive Transfer Tape 9707

(a)

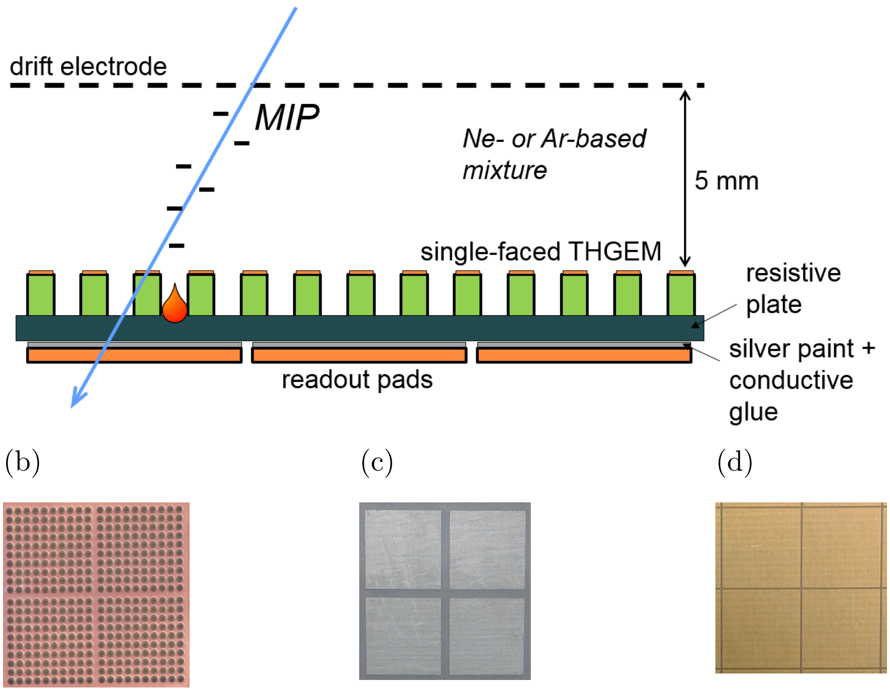


Figure 34: The $100 \times 100$ mm$^2$ RPWELL detector scheme. A single sided THGEM (b) is coupled to the readout anode through a resistive plate. The anode readout pads (d) are coupled to conductive pads patterned on the resistive plate (c). The metal bands in (b) are located above the underlying pad borders (c,d).

## A.3 300×300mm$^2$ RPWELL detector with RP directly coupled to pads readout

A $300 \times 300$ mm$^2$ RPWELL detector was assembled in an aluminum chamber with mylar window similarly to the one introduced in the design of the $100 \times 100$ mm$^2$ detector (section A.2). It comprised a single-sided copper-clad FR4 THGEM electrode with a nominal thickness of 0.8 mm; its measured thickness (including both Copper and FR4) was 0.96 mm, with variations smaller than 40 µm across the surface.

The electrode had 0.5 mm diameter holes, drilled on a 1 mm pitch hexagonal pattern; chemically etched 0.1 mm rims around the holes prevented sharp edges and other eventual defects. The $300 \times 300$ mm$^2$ THGEM electrode comprised six electrically decoupled $50 \times 300$ mm$^2$ segments (figure 35-a); 3 mm gaps were left between neighboring segments, to avoid inter-segment discharges in case of significant potential drop on one of them. The readout anode was composed of a $30 \times 30$ matrix of $10 \times 10$ mm$^2$ readout pads (figure 35-b); the individual pads were electrically connected to a 0.4 mm thick Semitron ESD225 plate (figure 35-c), in the same way as for the smaller detector described in section A.2. Figure 35-d shows the positioning of the resistive plate on top of the readout anode. The 5 mm drift gap was fixed by delrin spacers (50 mm spaced). The THGEM electrode, spacers and cathode were assembled on the anode using nylon rods and nuts (figure 35-e). More details on the detector assembly are given in [2].

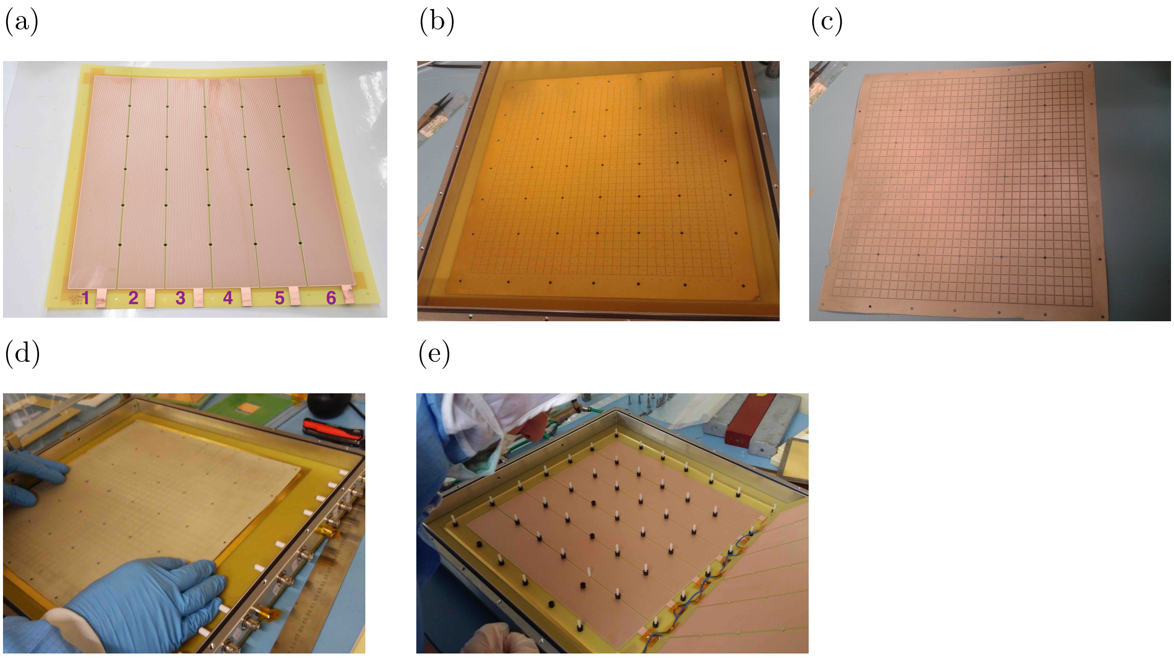


Figure 35: 300 × 300 mm$^2$ RPWELL detector prototype parts: (a)(c). (d) Assembling the resistive plate (c) on top of the readout anode (b), using conductive tape. (e) The open detector with all its elements (except the vessel cover): the anode and resistive plate (not visible); the THGEM electrode, with the support nylon pins (white) and spacers (black); the cathode (lifted on the right side); the aluminum vessel.

## A.4 100×100mm$^2$ tiled RPWELL detectors

Two RPWELL detectors with an area of 90×90 mm$^2$ were designed and assembled. This was the first attempt to build a prototype where the gas volume is defined by FR4 lateral frames glued together with the anode and the cathode (a full FR4 piece copper clad). The THGEM-electrodes plane was composed of nine 30 × 30 mm$^2$ tiles as shown in figure 36-a (gas nozzles and HV connections are visible). Each 0.8 mm thick THGEM tile had a 20×20 mm$^2$ squared hole pattern: 0.5 mm hole-diameter (100 µm rim) and a pitch of 0.96 mm, except for a central cross with a 1.3 mm pitch (the same as in the detector described in section A.2). Two different techniques were used to couple a doped silicate-glass [153] and a Semitron ESD225 RP to a strips (figure 36-b) and a pads anode (figure 36-c) respectively.

(a)

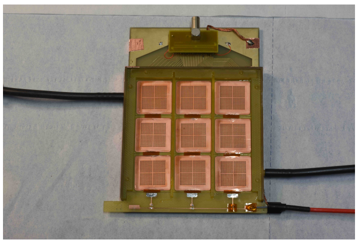

(b)

(c)

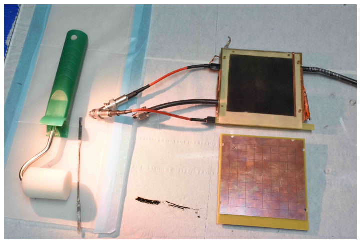

Figure 36: (a) Detector's THGEM-electrodes plane (cathode removed), made of 9 tiles with a 0.96 mm pitch square holes-pattern. Note the larger 1.3 mm pitch between the central holes rows. (b) The doped silicate-glass RP on top of the strips anode. (c) The Semitron ESD225 RP coated with graphite just before gluing to the pads anode.

### A.4.1 Doped silicate-glass resistive plate indirect coupling to anode

A 0.6 mm thick doped silicate-glass piece was glued to a hollow FR4 frame, its bottom side was sprayed with a graphite layer of ∼3 MΩ/□ and then covered with a 1 mm thick insulating polymer[4] to give support and protection to it. A lateral copper strip attached to the graphite layer and connected to ground granted charge evacuation through the surface. The RP was attached to an anode divided in three regions segmented into 1 mm, 1.5 mm and 2 mm pitch copper strips respectively. In this configuration, there was no electrical contact between the RP and the an-

[4]Polymer-G

ode which is placed at 1.6 mm from the THGEM bottom, 1 mm from the resistive film; as described in section 2.1.1 the signal is induced on the anode, without any charge actually reaching it. The RP mounted on top of the anode together with FR4 frames is shown in figure 36-b (also the input and output gas nozzles are visible). The $100 \times 100$ mm$^2$ tiled glass-RPWELL detector scheme and operation principle are shown in figure 37. Because of the large induced-signal spread onto the readout strips, due to the lateral charge evacuation across the RP bottom surface and the large distance between the electron avalanche and the anode, this detector was used for position resolution studies.

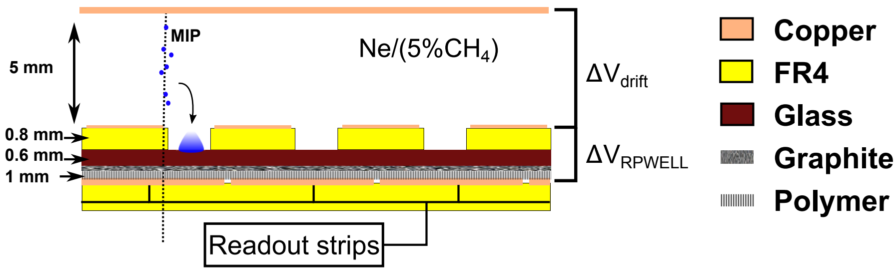


Figure 37: A schematic view of the $100 \times 100$ mm$^2$ tiled glass-RPWELL detector assembly, with anode readout strips, and operation principle.

### A.4.2 Semitron ESD225 coupling to anode through epoxy/graphite layer

The main purpose of this prototype was studying the effect of the RP coupling to the anode through a graphite/epoxy layer on the average pad multiplicity.

A 0.4 mm thick Semitron ESD225 static dissipative acetal plate was coated with a thin resistive layer of graphite of $\sim$3 M$\Omega/\square$ surface resistivity and then glued to a readout anode with a very thin layer of epoxy[5]. The readout anode was divided

[5]Araldite 2011

into $10 \times 10$ mm$^2$ pads. Under the assumption that the epoxy layer would isolate the resistive layer from the anode, we attached to the sides of the graphite layer copper strips connected to ground for charge evacuation; a subsequent experiment (see appendix B) showed that this is not the case: the contact of fluid epoxy with graphite during gluing results in a finite resistivity between the RP and the anode; the charge is therefore evacuated through the readout pads and it doesn't travel across the resistive layer to the side copper strip. This is important because lateral charge propagation in the resistive layer would cause an increase in pad multiplicity, as shown in [129]. The main advantage of this assembly method over the one presented in section A.2 is the fact that it does not require any patterning of the RP surface; the coupling to the anode is uniformly applied (instead of channel-by-channel), so it can be used indifferently with any readout anode segmentation and size. The Semitron ESD225 RP coated with graphite, together with the anode spread with epoxy just before gluing is shown in figure 36-b. The $100 \times 100$ mm$^2$ tiled Semitron-RPWELL detector scheme and operation principle are shown in figure 38.

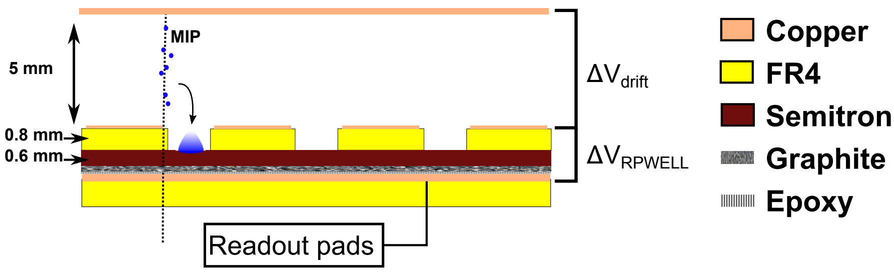


Figure 38: A schematic view of the $100 \times 100$ mm$^2$ tiled Semitron-RPWELL detector assembly, with anode pads, and operation principle.

## A.5 500×500mm$^2$ RPWELL prototype with RP coupling to strips readout through an epoxy/graphite layer

For the first time a $500 \times 500$ mm$^2$ RPWELL chamber was designed and produced. The resistive plate was made of 4 doped silicate-glass [153] tiles, $250{\times}250$ mm$^2$ in size. The anode was segmented into 1 mm pitch readout strips, and the RP tiles were coupled to it through a graphite and epoxy layer, using the method described in section A.4 for the $100 \times 100$ mm$^2$ tiled Semitron-RPWELL. As described in appendix B, there is a finite conductivity between the RP and the anode strips, therefore the avalanche charge is collected and neutralized at the anode, minimizing its lateral spread. An insulating paint[6] was used to fill all the glass interfaces and to cover all the regions around the tiles, where the anode is directly exposed to the gas and therefore it is not protected against discharges (figure 39-a). The effectiveness of this method was proved by the detector electrical stability in normal operation and under very high intensity x-rays irradiation (section 3.3.1). The electron multiplier was composed by two $500{\times}250$ mm$^2$ THGEM segments with a nominal thickness of 0.8 mm; holes of 0.5 mm diameter, with 0.1 mm etched rims, arranged in a uniform square pattern of 1 mm pitch. The two THGEMs were connected to a high voltage ruler, so that they can be biased separately from a connection outside the chamber. The 3 mm gas gap between the THGEM and a cathode plane was defined by 4 lateral frames, that together with 34 round spacers positioned over the THGEM area (figure 39-b) and a central spoke (figure 39-c), serve to press the THGEM electrodes in contact with the RP. All the parts were machined from polycarbonate. Four gas inputs at the chamber corners allow for arranging the gas circulation according to the specific

[6] vonRoll Damicoat 2405-02

gas composition and chamber orientation. The central spoke has a hole to let the gas circulate in between the two sectors of the chamber. All the detector parts were glued together with epoxy[7], using a vacuum bag to apply a uniform controlled pressure of about 0.02 atm$^2$ (0.02 kg/cm$^2$ corresponding to 10 kg/(glass tile)). This limit is the minimum pressure that was possible to control. All the parts were glued in different stages, interleaved by visual inspection and electrical tests both in air and in different gas mixtures. Here a summary of the assembly protocol:

- All the parts were inspected and their actual dimensions were measured. A dummy-assembly was performed to ensure that all the parts could fit together.
- The silicate doped-glass tiles were sprayed with graphite and glued to the anode (figure 40-a).
- After epoxy curing, all tiles interfaces and borders were protected with insulating paint[8]. After curing the excesses were removed and the the surface cleaned.
- The THGEM electrodes were placed on top of the RP (figure 40-b). An electrical test in air was performed to ensure the electrodes quality and the anode protection. The resistance between strips and from strips to ground were also checked. Tests in operating gas mixtures (using a plastic bag similar to the one in figure 40-c) were done to reach operation conditions. At this stage it was possible to operate the detector and measure signal from a source.
- The lateral frames, central spoke, HV ruler, spacers and gas connectors were positioned using internal and side jigs and glued under vacuum (figure 40-c).
- The THGEM sectors were connected to the HV ruler and the electrical tests were repeated.

[7] Araldite 2011

[8] vonRoll Damicoat 2405-02

- After removing the internal jigs, the cathode was glued and the chamber was sealed by filling all the possible gaps with epoxy.
- HV cables were connected to each electrode.

In next prototypes, this same assembly method will be used to couple a $500 \times 500$ mm$^2$ RP-WELL to $10 \times 10$ mm$^2$ pads readout boards with integrated MICROROC chips [5], like the ones described in [168].

(a) (b) (c)

Figure 39: a) The glass tiles interface and borders covered with insulating paint. b) A lateral frame, a support spacer and the HV ruler. c) The central spoke.

(a) (b) (c)

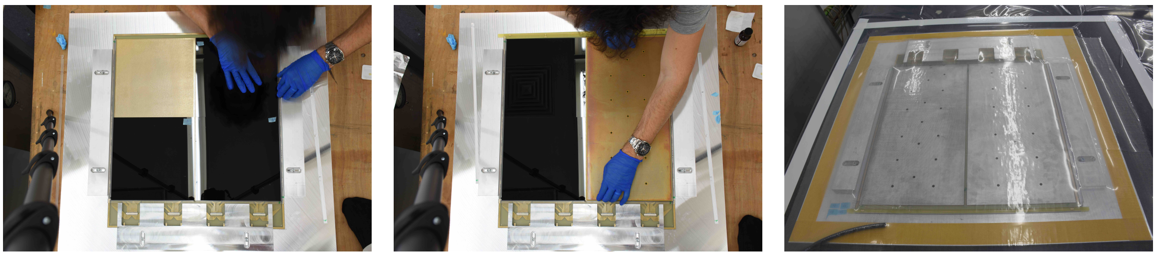

Figure 40: $500 \times 500$ mm$^2$ RPWELL assembly. a) 4 glass tiles are coupled to the anode through a graphite and epoxy layer. b) Two THGEM tiles are placed on top of the RP. c) Gluing of frames and spacers pressed by vacuum bag.

# Appendix B

# Resistive plate coupling through epoxy/graphite layer

The resistivity between the RP and the anode in case that they are coupled through an epoxy and graphite layer, as described in section 2.1.1 was investigated. Dedicated anodes that allowed for measuring both surface resistivity and bulk resistivity were prepared. Figure 41-a shows the experimental setup and the assembly steps. From top to bottom: the first electrode is the equivalent of the resistive plate in the RPWELL detector, it has a central FR4 region in between two copper lines for both bulk and surface resistivity measurements; the second electrode (anode) has a full copper region that is the equivalent of the detector anode. Following the same procedure used for the detectors described in sections A.4 and A.5, a graphite layer was spray-painted on the first electrode, covering also the copper strips. Then a thin epoxy film was applied with a roller and the two electrodes were glued together under vacuum. As a comparison, a second assembly was produced without graphite deposition on the resistive plate. For both setups, two resistance measurements were performed using an insulation tester[1]: surface resistivity (figure 41-b (top)) between the two sides of the first electrode and bulk resistivity (figure 41-b (bottom)) between the anode and the two sides of the first electrode. Concerning the possibility that chemical changes of the epoxy might occur in time, affecting significantly its electrical properties, the setups were placed in a nitrogen desiccator (20°C, $< 5\%$ humidity) for 12 hours and then measured again. The setups were also warmed in an oven at a temperature between 40°C and 50°C for about 12 hours, and then measured again after cooling down to room temperature for one hour. All the results are shown in table B.1, together with further measurements several hours after the treatment. The tests on the sample assembled with graphite and epoxy show that there is a finite bulk and surface resistivity, stable for relatively long time and after curing with temperature and dry environment. In the sample without graphite, on the contrary, the resistivity between the electrodes was very high, more than 22 GΩ, which was the measuring instrument limit when operated at maximum voltage of 1000 V. The surface and bulk resistivity values should be optimized for specific application, by tuning the amount of graphite sprayed on the RP, to reach the desired conductivity between readout channels (affecting lateral charge spread and crosstalk) and between RP and anode (important for efficient charge evacuation).

[1]Megger MIT400

(a) (b)

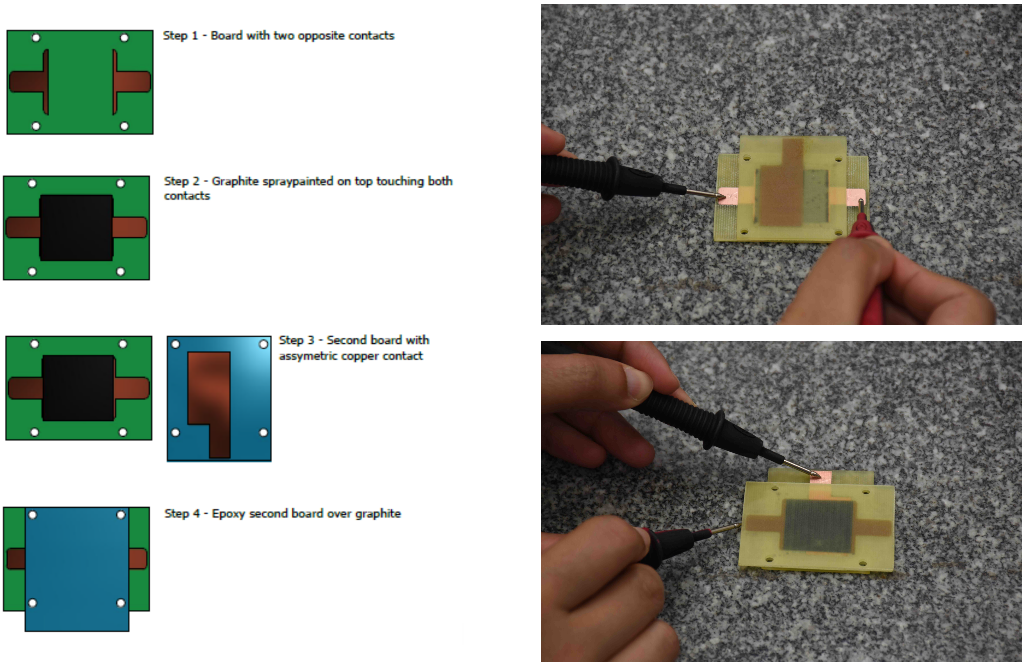


Figure 41: a) Schematic of the electrodes assembly devised for epoxy conductivity tests with assembly steps. b) Surface (top) and bulk (bottom) resistivity measurements.

| | **surface resistivity [MΩ/□]** | **Bulk resistance 9.5 mm distance [MΩ]** | **Bulk resistance 1.5 mm distance [MΩ]** |
|---|---|---|---|
| **before gluing** | 2.7 | - | - |
| **after gluing** | 10.6 | 8.4 | 8.9 |
| **after 12 h in desiccator** | 9.8 | 8 | 8.3 |
| **after 12 h baking 60°** | 15 | 11 | 11 |
| **after 12 h** | 14 | 11 | 8.7 |

Table B.1: Results from the resistivity tests.

# Appendix C

# Edge effects study

The presence of spacers and support structures in gaseous detectors can cause distortions of the electric field and dead areas, affecting their performance, namely detection efficiency, energy resolution, etc. In order to address this issue systematically, a set of measurements was conducted with the $30 \times 30$ mm$^2$ chamber described in appendix A.1, operated in Ar/(5%)$CH_4$ in atmospheric conditions, and irradiated with a x-ray scanner (figure 42). As detailed in appendix A.1, to emulate the presence of a frame in the detector, an FR4 frame was positioned on top of the THGEM electrode, so that its inner edge distance to the center of the last raw of holes was fixed at 0.7 mm or 2.7 mm (see figure 33). The setup comprised an x-ray tube[1] with copper target, providing a collimated beam (1 mm diameter) of photons peaked at 8 keV. The tested chamber was assembled on a high precision x-y stepper-motor driven holder, and it was scanned with a typical step size of 1 mm. In each point a charge spectrum was measured using a standard preamplifier/linear amplifier/MCA calibrated chain, and stored for analysis. The main peak in each spectrum was fitted to a Gaussian and the mean value and the energy resolution - defined as the Gaussian FWHM/mean -

[1] Oxford Jupiter 5000

were obtained.

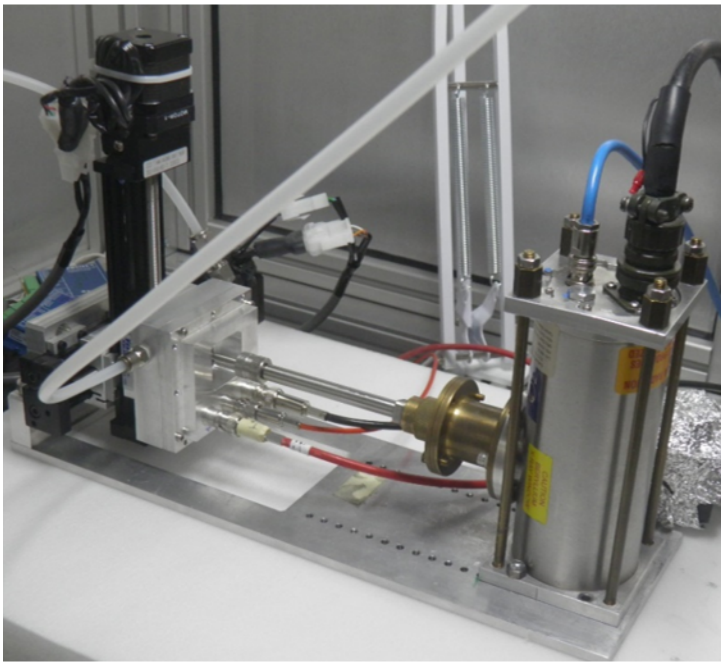

Figure 42: The $30 \times 30$ mm$^2$ RPWELL prototype mounted in the small x-y scan system with the copper x-ray gun.

The detector was scanned along one axis; a spectrum was acquired in each position for a fixed amount of time. To reduce the systematic uncertainties due to non-uniformities arising from the electrode thickness and the detector assembly, all the measured quantities were normalized with respect to a reference measurement in which the FR4 frame was removed from the detector.

Examples of spectra recorded at different beam positions with the FR4 frame at 0.7 mm from the THGEM holes are shown in figure 43; the x-axis is calibrated to the total number of electrons in an avalanche. The low charge shoulder appearing when the beam is at 2 mm from the last hole indicates upon PEs loss on the frame (i.e. a collection efficiency $< 1$).

In order to quantify this effect, average quantities were plotted, for both frame distances from the THGEM holes (0.7 mm and 2.7 mm). In figure 44-a, the spectrum integral, normalized to measurement obtained without frame, is plotted as a function of the x-ray beam position. The spectrum integral can be expressed as I = $n_{PE} \cdot a_{collection} \cdot G \cdot n_{events}$, where $n_{PE}$ is the average number of PEs extracted by a x-ray photon, $a_{collection}$ is the PEs collection efficiency, G is the detector gas gain, and $n_{events}$ is the number of photon events recorded. Considering a measurement with the FR4 frame in place, giving $I_{frame}$, and a measurement without frame, giving $I_0$, the plotted ratio $I_{frame}/I_0$ gives the ratio of $a_{collection} \cdot n_{events}$ in the two cases. It is possible to appreciate a loss starting from 1.5 mm from the last hole, more pronounced when the frame is closer to the holes. Even though it is not possible to directly relate this measurement to the PEs collection efficiency, it is an indication of the typical distance at which a frame induces an efficiency loss. Despite the different geometry and radiation source, this result is similar to what found in test-beam measurement for the 500 × 500 mm$^2$ detector (figure 30). Figure 44-a shows that the normalized peak position - representing the gain at full collection efficiency - is not affected by the frame, when it is mounted at 2.7 mm from the holes, but it increases starting from 1.5 mm away from the last hole center, when the frame is placed 0.7 mm away. It is known from previous works [136] that the detector gain increases in the holes at the edge; this effect is enhanced by the presence of the frame. The energy resolution when approaching the edge (figure 44-c) gets worse ∼1.5 or ∼3 times when the frame is at 0.7 mm or at 2.7 mm from the last hole respectively.

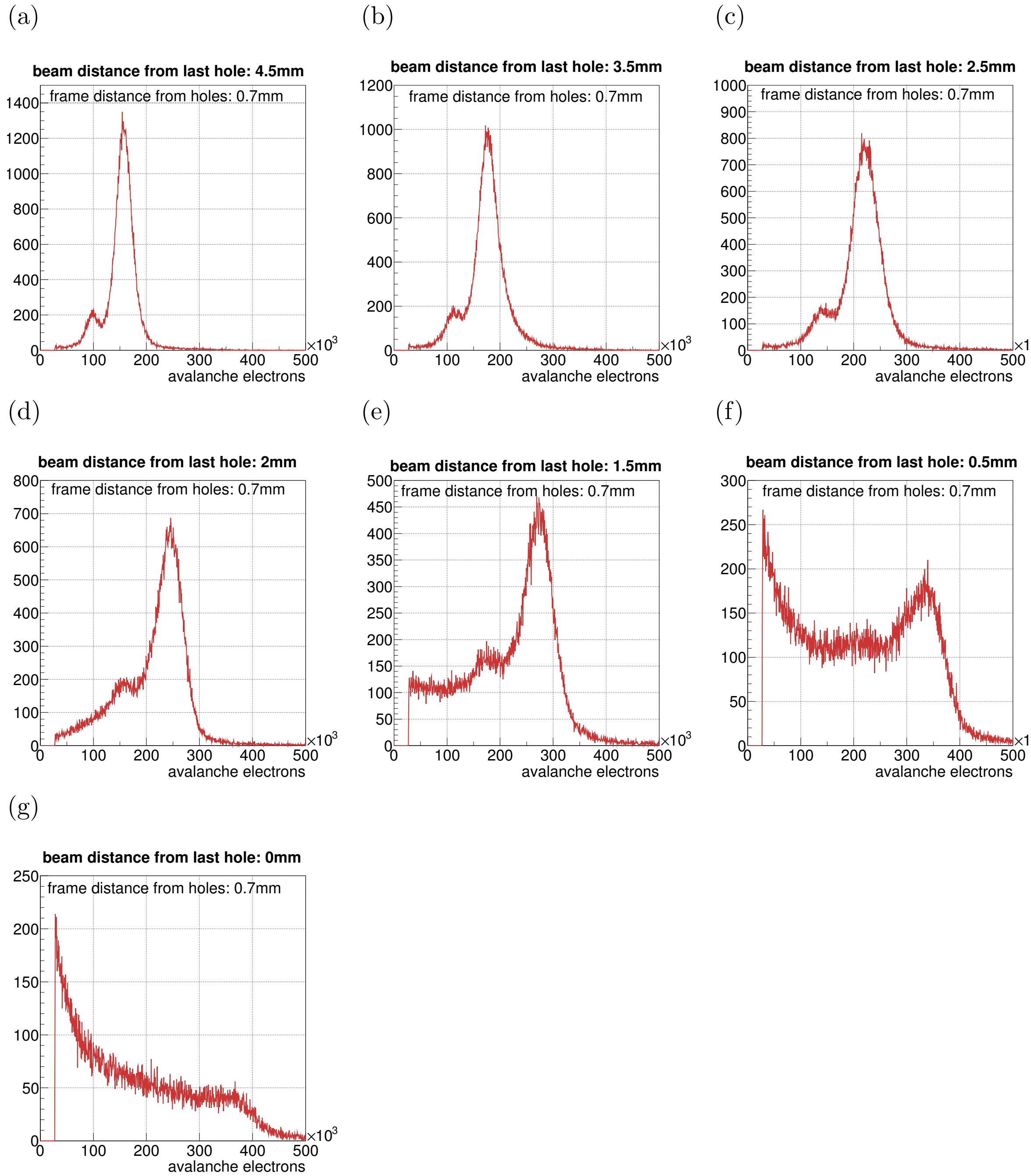


Figure 43: x-ray spectra recorded at different x-ray distance from the last hole. The FR4 frame is placed 0.7 mm far from the last hole center.

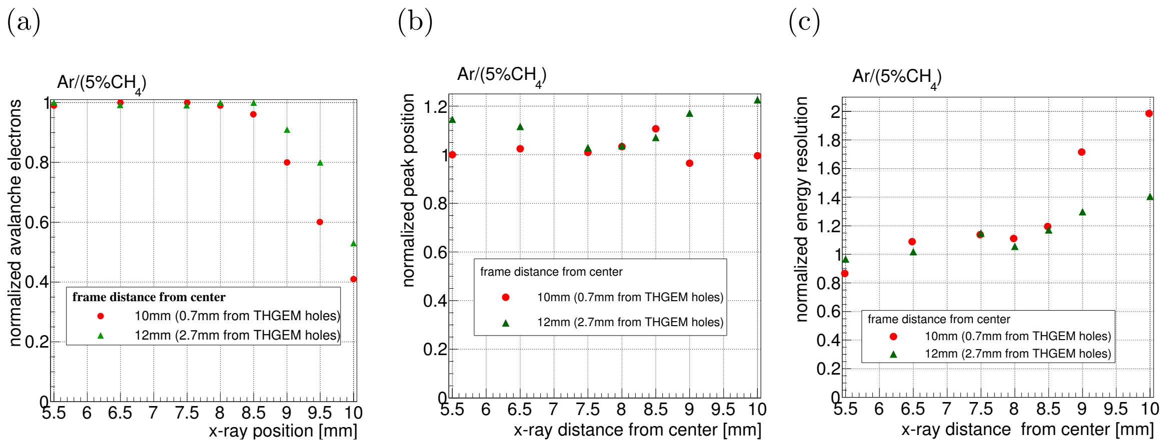


Figure 44: For FR4 frame distances of 0.7 mm and 2.7 mm from the THGEM holes: (a) Spectrum integral; (b) full-collection peak position; (c) energy resolution. All the results are normalized to a measurement without frame.